



UNIVERSIDAD DE CHILE
FACULTAD DE CIENCIAS FÍSICAS Y MATEMÁTICAS
DEPARTAMENTO DE FÍSICA

Dissipative Localized Structures

Marcel G. Clerc

SANTIAGO DE CHILE
September 2020

Contents

Contents	3
1 Particles in Physics	7
2 Conservative Solitary Waves: Solitons	11
2.1 Nonlinear wave paradigm: <i>Solitary waves or Soliton</i>	12
2.1.1 Solitary waves at shallow limits	14
2.1.2 Localized linear waves	14
2.2 Fermi-Pasta-Ulam-Tsingou problem	16
2.2.1 Fermi-Pasta-Ulam-Tsingou problem and Kdv equation	18
2.2.2 Dynamics of counterpropagating solitons: Boussinesq equation .	22
2.2.3 Solitary waves in fluidized granular matter	25
2.3 Chain of coupled pendulums	28
2.3.1 sine-Gordon Equation	32
2.3.2 Breather solitons and weak nonlinear analysis	35
2.3.3 Nonlinear Schrödinger equation	37
2.3.4 Nonlinear enveloped equation in kerr media	40
3 Dissipative solitons in parametric systems	45
3.1 Experimental observations of dissipative solitons in parametric systems	46
3.2 Parametrically forced pendulum chain	48

3.2.1	Quasi-reversible limit: parametrically forced nonlinear Schrodinger equation	50
3.3	Effective parametric resonance	59
3.3.1	Dissipative solitons in two dimensions	72
3.4	Interaction of parametric solitons	74
3.4.1	Interaction of a pair of solitons	74
3.5	Interaction pair law of localized states in two-dimensions	80
3.5.1	Interaction far from the appearance of localized structures.	83
3.5.2	Self-similar dynamics of a soliton gas	84
3.6	Solitons in an inhomogeneous medium	87
3.7	Phase Shielding Dissipative solitons	91
3.7.1	Analytical description	93
3.7.2	Phase dynamics	98
3.7.3	Soliton stability with homogeneous phase	100
3.7.4	Phase shielding solitons in two-dimensions	104
4	Dissipative solitons in forcing systems	107
4.0.1	Josephson junctions an exceptional oscillator	109
4.0.2	From driven damped sine-Gordon model to driven damped non-linear Schrödinger equation (Lugiato-Lefever equation)	111
4.1	Localized structures	115
4.1.1	System without dissipation	118
4.1.2	Quasi-reversal limit	120
5	Structures located between homogeneous states	123
5.1	Bistable model	123
5.1.1	Population dynamics	124
5.1.2	Nematic-isotropic transition	125
5.1.3	Ferromagnetic transition	127
5.2	Particle-type solutions between two-uniform states: wave called Front	130

5.3	Front propagation at the Freedericksz transition	134
5.4	Kink interaction	136
5.4.1	Kinematic law of a pair kinks	136
5.4.2	Interaction of a gas of kinks: coarsegraning	142
5.4.3	Effect of discretization kink interaction	145
5.5	Localized states as result of kink interaction	147
5.5.1	Simple model: Turing-Swift-Hohenberg equation	149
5.5.2	Localized structures as result front interaction	153
5.5.3	Amplitiude approach to localized patterns and hole state	154
5.5.4	Snaking bifurcation diagrams	159
5.6	Liftshitz normal form: non variational generalization of Turing-Swift-Hohenberg Equation	159
5.7	Alee effect in population dynamics: Nagumo Model	162

Bibliography**165**

Chapter 1

Particles in Physics

Particles have been a fundamental concept of physics [183], which has accompanied it since the dawn of modern physics. Intuitively, a particle or corpuscle is a tiny proportion of matter, that is, a localized object, which is ascribed various physical properties such as volume and mass. The main characteristic of a particle is to be a localized object; that is, this corpuscle is described by a position. According to their size, the particles are described as being sub-atomic particles (electrons, neutrinos, and quarks), or microscopic like atoms or molecules, or macroscopic like dust in the air (see Fig. 1.1). Classically, particularly in mechanics and statistical mechanics, particles are described as material points that exchange energy and momentum through their interaction.

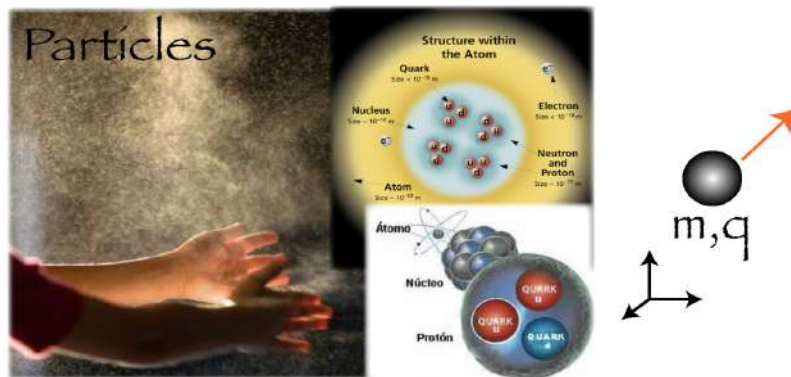


Figure 1.1: Miscellaneous standard particles.

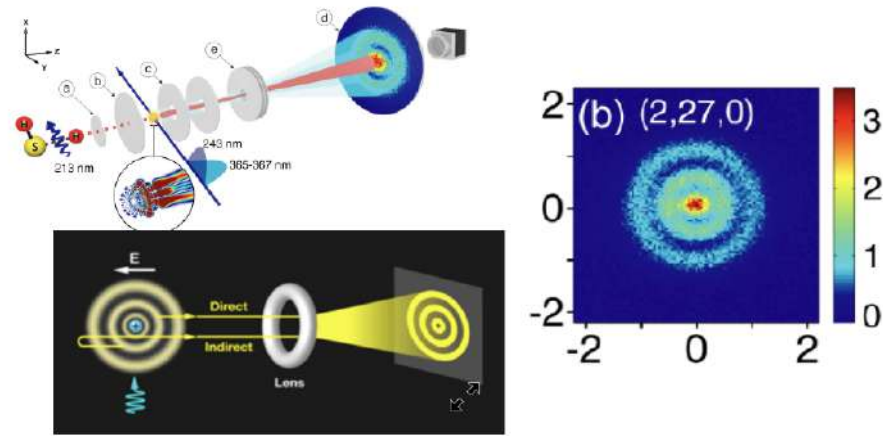


Figure 1.2: Observation of the electron orbitals of an excited hydrogen atom [193].

Contrary to the microscopic level in the world governed by quantum mechanics, the particles are described by the wave function. That is, they are described by a complex field whose modulus accounts for the probability density. Then at a fundamental level, the particles are described by fields that ascribe or occupy all space. These fields are concentrated in a region that is interpreted where the particle is. Recently, thanks to quantum microscopy (photoionization microscopy), the structure of a wave function have been observed [193]. Figure 1.2 shows the wave function of a hydrogen atom.

In simple terms, the particles correspond to localized solutions of the wave function. Macroscopic systems, that is, those systems made up of a large number of constituents,

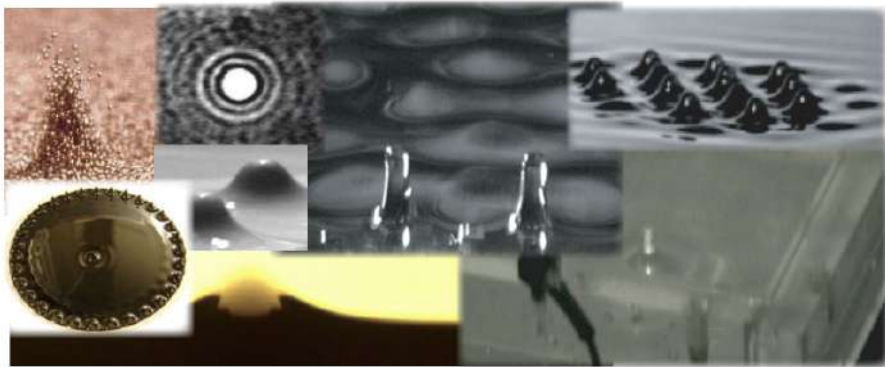


Figure 1.3: Collage of the localized structures in nature.

are described by fields. These fields also exhibit localized solutions, which are called particle-type solutions or dissipative structures. Figure 1.3 illustrates a collage of examples of particle type solutions. The main objective of this monograph is to study the mechanisms, existence, stability properties, dynamical evolution, and bifurcation diagrams of localized solutions.

Chapter 2

Conservative Solitary Waves: Solitons

Macroscopic systems in equilibrium, that is, systems composed of many fundamental constituents isolated or in contact with a thermostat that can exchange energy, particles, momentum, or some other physical quantity, are characterized by exhibiting temporally homogeneous and spatially uniform equilibria. This type of equilibrium is known as *the thermodynamic equilibrium* [134]. Local disturbances of these equilibrium states are characterized by exhibiting linear waves that dampen their amplitude as a function of time. Figure 2.1 illustrates this type of disturbance. This type of behavior is described by means of the equation of waves or dispersive medium with dissipation

Therefore, macroscopic media in equilibrium are dispersive wave media with dissipation. However, this type of behavior changes dramatically when localized disturbances of finite large amplitude occur. This type of localized disturbance can give rise to one



Figure 2.1: Damped waves observed in the ocean (snapshots obtained from the internet).

of the paradigmatic phenomena of Nonlinear Physics, the emergence, and evolution of solitary waves or solitons [88, 150, 177].

2.1 Nonlinear wave paradigm: *Solitary waves or Soliton*

In 1834 physics will have a celebrated year thanks to the observations of the Scottish engineer John Scott Russell, while conducting experiments to determine the most efficient design for ships in a canal, he discovered a phenomenon that he described as the translation wave. In fluid dynamics, this wave or non-linear wave is now called a solitary wave or soliton. The discovery is described below, in his own original words. "He was observing the movement of a ship that was being moved rapidly along a narrow channel by a pair of horses, when the ship suddenly stopped, causing a The mass of water in the canal had set in motion, which was accumulated around the bow of the ship, and suddenly left behind, rolling forward with great speed, assuming the form of a large solitary rise, a round mound, smooth and well-defined water, which continued its course along the channel apparently without a change in shape or decrease in velocity. I followed it on horseback, and it still outpaced at a rate of about eight to nine miles per hour [14 km / h], retaining its original shape at about thirty feet [9 m] long and one foot and a half. [300-450 mm] high. Its height gradually decreased, and after a one or two-mile [2.3 km] chase, I lost it at the ends of the channel. Such is, in the month of August 1834, it was my first opportunity to see this singular and beautiful phenomenon that I have called the translation wave "(John Scott Russel) [187]. A recreation of the solitary wave observed by John Scott Russell is illustrated in Figure 2.2. The use of the soliton expression was proposed in the telecommunications context by Akira Hasegawa [110].

Scott Russell subsequently carried out systematic experimental and theoretical investigations of solitary waves and concluded: i) solitons are stable and can travel very long distances, ii) The speed depends on the size of the wave, and its width in the depth of the water. iii) Unlike normal waves, they will never merge, so a small wave is hit by a



Figure 2.2: El ingeniero escocés John Scott Russell y una recreación de una onda solitaria similar aquella observada por Scott Russell.

large one, rather than combining the two. If a wave is too large for the depth of the water, it splits into two, one large and one small.

Observations:

- The first characterization can simply be understood as the result that this solution is a localized form of energy transport. In the ideal case of modeling this phenomenon by means of Hamiltonian equations [132], these solutions propagate without deformation forever. It is important to note that Scott Russell notes that these solutions are out of balance in his terms "His height (soliton) was gradually decreasing and after a chase of one or two miles"
- From his second observation, we can conclude that the shape is modified as a function of the amount of transported water, which is in turn a manifestation of the conservation of energy and mass. It is also the first manifestation of the

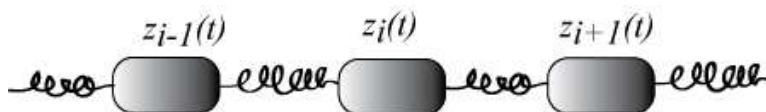


Figure 2.3: Discrete model of a wave medium.

underlying non-linear phenomenon in solitons since its speed is not the same for solitons of different heights. Which contradicts the typical behavior of a linear wave medium.

- The third observation is a manifestation of the underlying nonlinear phenomenon in solitons. Linear waves are characterized by being proportional to their cause, that is, a double-amplitude disturbance generates double-amplitude waves. Therefore, the collision of two waves is not the sum of their respective amplitudes, there are phenomena of phase shift from their positions to their maximums, as we will see later.
- The deformable solitary waves described by Scott Russell are of a one-dimensional nature from a point of view of their characterization and dynamics, that is, the transverse direction does not play any relevant role. However, if one performs a localized disturbance on a lake, that is to say, no longer a restricted one-dimensional system as is the case of the channel, solitary waves are not observed.

It is important to note the spirit of an integral physicist of Scott Russell who, unlike many of his contemporaries and predecessors, carried out a complementary activity both experimental and theoretical.

2.1.1 Solitary waves at shallow limits

2.1.2 Localized linear waves

An extended oscillatory medium is characterized by being microscopically constituted by elements around its equilibrium position, which can be modeled to a first approxi-

mation by coupled oscillators (see figure 2.3). For example, this is the usual description of a bungee cord which is modeled by

$$\ddot{z}_i(t) = k(z_{i+1} - 2z_{i+1} + z_{i-1}), \quad (2.1)$$

where $z_i(t)$ it accounts for the displacement with respect to its equilibrium position of the i -th element. The separation between these elements is characterized by distance dx . In the continuous limit, one can consider that $dx \rightarrow 0$ and $k \rightarrow \infty$ so that $c^2 \equiv k/dx^2$ is finite and the variable $z_i(t)$ becomes a field $z(x, t)$, where x accounts for the spatial parameterization. The parameter c accounts for the speed of propagation of the disturbances around the equilibrium position. Then the coupled oscillator equation (2.1) takes the form (linear wave equation)

$$\partial_{tt}z = c^2 \partial_{xx}z, \quad (2.2)$$

The most intriguing solution to this equation is the solution proposed by D'Alembert [77]

$$z(x, t) = f(x \pm ct), \quad (2.3)$$

where f is an arbitrary function that must be differentiable at least twice. If the sign \pm is $-$ ($+$) the previous solution gives a solution with profile f that propagates to the right (left) without deforming. Therefore, this system exhibits waves that propagate in both directions at the same speed. Figure 2.4a shows the evolution of the D'Alembert

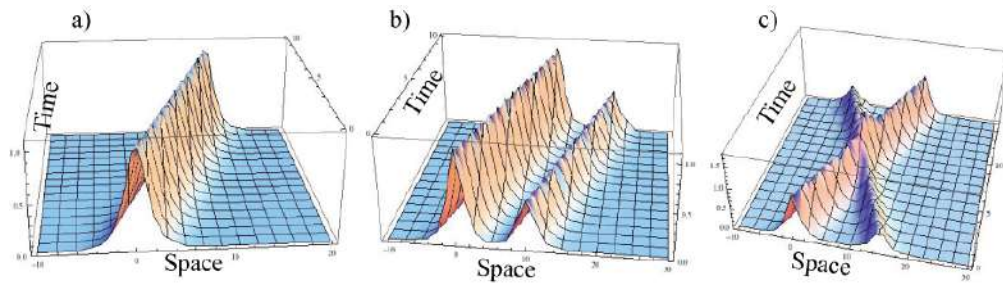


Figure 2.4: Soluciones localizadas de la ecuación de ondas (2.2).

solution in a space-time diagram for the case of a localized profile. It is important to note that regardless of the shape of the profile, it propagates with the same speed, as illustrated in figure 2.4b. Therefore one disturbance can never reach another. Note that these solutions do not transport matter but energy and momentum. Since the profile is localized, one can naturally associate a position to this solution, for example, the one that corresponds to its maximum. Then one can consider this solution as a particle-like solution, which represents an isolated wave. A question of interest is what happens if one collides two counter-propagative waves. That is, one considers a more general D'Alembert solution

$$z(x, t) = f(x - ct) + h(x + ct), \quad (2.4)$$

As a consequence of the superposition principle, these two waves simply overlap when they collide and continue without deformation and information that there was a collision. This process is illustrated in Figure 2.4c.

Observations:

- In these linear media, it is not possible to speak of solitary waves since the solution acquires the form that one imposes in the initial conditions.
- As a consequence of the superposition principle, each localized solution is entirely independent of the others, and therefore it makes no sense to speak of interaction; that is, this system accounts for gas of independent particles, gas ideas without any type of exchange.

2.2 Fermi-Pasta-Ulam-Tsingou problem

Naturally, one hopes that the image of the previous linear system should be slightly modified with the inclusion of the first non-linearities, however, since the previous behavior is not structurally stable, we will see how new dynamical behaviors emerge. In the summer of 1953 nonlinear science entered a paradox: Fermi, Pasta, Ulam, and

Mary Tsingou (cf. figure 2.5) carried out numerical simulations of a vibrating string in a nonlinear regimen, that is, they are considered not so small deformations. It is important to mention that this is the first performance of numerical experiments to achieve a better understanding of physical systems. The behavior of the system was found to be quite different from what intuition would have led to expect. Fermi thought that after many iterations, the system could present thermalization, that is, a distribution of equipartition of energy (ergodic behavior) between the modes and thus forget its initial condition. This is based on the fact of believing that the systems with few degrees of freedom exhibited chaotic behavior which does not equalize the energy, but as one increases the degrees of freedom, the systems tend to equalize the energy as observed in the thermodynamic limit. However, the system exhibits a very complicated quasi-periodic dynamics, that is, certain privileged recurring behaviors emerged. They

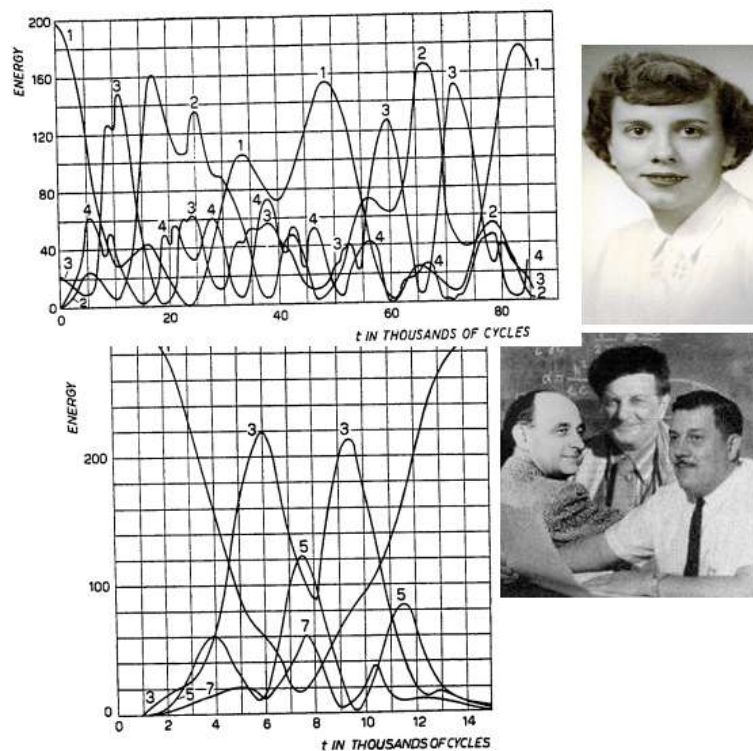


Figure 2.5: Numerical evolution of energy for different modes.

published their results in a technical report from Los Alamos in 1955 ¹ [92].

The behavior exhibited by this system is due to the fact that it does not tend to thermodynamic equilibrium due to the reason that this system is integrable [14, 213], that is, if the degree of freedom is increased, quantities are also added in the same proportion conserved, so the dynamics are not simply to conserve energy but a series of other quantities, which restrict the dynamics. As we will see, it is this in the context that one expects for conservative systems to find localized solitary wave solutions. That is, solitons are the consequence of integrable Hamiltonian systems [90].

2.2.1 Fermi-Pasta-Ulam-Tsingou problem and Kdv equation

To have a better understanding of the problem, we will take the continuous limit of the chain of nonlinear oscillators following the line of thought of Kruskal and Zabusky [210]. The equation that describes the chain of oscillators (2.1) can be generalized considering that the coupling constant between the oscillators k is nonlinear, then the equation that describes the chain of oscillators takes the form

$$\ddot{z}_i(t) = (z_{i+1} - 2z_{i+1} + z_{i-1}) (k_o + \alpha(z_{i+1} - z_{i-1})), \quad (2.5)$$

where k_o and α account for the linear coupling and nonlinearity between the oscillators, to consider the continuous limit, we will consider the following strategy $z_{i+1} = z(x+h)$ and we will expand this expression to the derivatives of order four in order to generalize the wave equation, that is, $z(x+h) \approx z(x) + h\partial_x z + h^2\partial_{xx}z/2 + h^3\partial_{xxx}z/3! + h^4\partial_{xxxx}z/4!$. Introducing this approximation in the previous equation

$$\partial_{tt}z \approx \left(h^2\partial_{xx}z + \frac{h^4}{12}\partial_{xxxx}z \right) \left(k_o + \alpha 2 \left(h\partial_x z + \frac{h^3}{6}\partial_{xxx}z \right) \right). \quad (2.6)$$

¹Enrico Fermi died in 1954 and so this whitepaper was published after Fermi's death. In this report, despite the fact that Tsingou wrote the codes, which today would be simple but in the programming dawn were complex, she was not consolidated as a co-author because perhaps "she fulfilled a technical role" and not a scientific development, her contribution was recognized starting in 2008, where this problem changed from being called Fermi-Pasta-Ulam to Fermi-Pasta-Ulam-Tsingou [87].

considering the dominant terms, we obtain

$$\partial_{tt}z = h^2 k_o \partial_{xx}z + \frac{h^4 k_o}{12} \partial_{xxxx}z + \alpha 2h^3 \partial_{xx}z \partial_x z. \quad (2.7)$$

In the limit $h \rightarrow 0$ and $k_o \rightarrow \infty$ with $hk_o = c^2$, one obtains the linear wave equation, however if we consider the previous corrections and normalize the units of z so that the non-linear coefficient is one, we obtain that the above equation takes the form

$$\partial_{tt}z = c^2 \partial_{xx}z + \gamma \partial_{xxxx}z + \partial_{xx}z \partial_x z. \quad (2.8)$$

where $\gamma \equiv h^4 k_o / 12$, which is a small number. This is a nonlinear wave equation. Introducing the following variable $u = \partial_x z$ and taking the partial derivative with respect to space, the previous equation takes the form (Boussinesq equation [33])

$$\partial_{tt}u = \partial_{xx} \left(c^2 u + \frac{u^2}{2} + \gamma \partial_{xx}u \right). \quad (2.9)$$

This equation was derived by Boussinesq to account for the surface waves observed by John Scott Russell [33].

To find the solution and describe the dynamics exhibited by equation (2.8) we will consider the following ansatz $z(x, t) = f(x - ct, \tau = t) + w(x - ct, \tau)$, where $f(\zeta \equiv x - ct, \tau)$ is a small function ($f \ll 1$) and slowly variable in ζ and τ , that is, the successive derivatives of f each time are smaller ($\partial_{\zeta\zeta}f \ll \partial_{\zeta}f \ll 1$ and $\partial_{\tau\tau}f \ll \partial_{\tau}f \ll 1$), ζ is the coordinate in the co-mobile system, τ accounts for the slow dynamics and W is a corrective function that will account for the nonlinear corrections for f . Introducing the previous ansatz in equation (2.8) to the lowest order we have

$$\partial_{tt}f(x - ct) = c^2 \partial_{xx}f.$$

Which satisfies any sufficiently smooth function. In the following order, one get

$$\partial_{tt}W - c^2 \partial_{xx}W = c \partial_{\zeta\tau}f + \gamma \partial_{\zeta\zeta\zeta\zeta}f + \partial_{\zeta\zeta}f \partial_{\zeta}f. \quad (2.10)$$

To solve the equation for W we must invert this linear equation. Then we impose the solubility condition, which means that there cannot be terms that explicitly depend on ζ . Then f must satisfy

$$c \partial_{\zeta\tau}f = -\gamma \partial_{\zeta\zeta\zeta\zeta}f - \partial_{\zeta\zeta}f \partial_{\zeta}f. \quad (2.11)$$

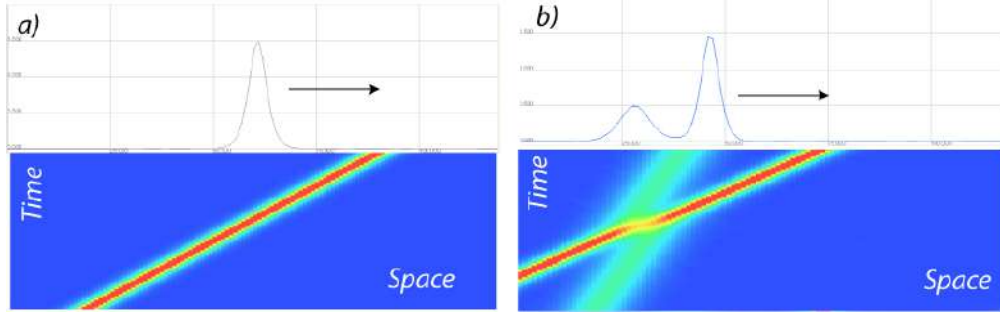


Figure 2.6: Solitary waves exhibited by the Korteweg-de Vries equation (2.13). a) a solitary wave and its respective evolution in the space-time diagram; b) collision of two solitary waves.

Introduciendo el cambio de variable $u(\tau, \zeta) = \partial_{\zeta} f$ y normalizando el tiempo en unidades de la velocidad de propagación de las ondas, satisface la ecuación de *Korteweg-de Vries*

$$\partial_{\tau} u = -\gamma \partial_{\zeta \zeta \zeta} u - u \partial_{\zeta} u. \quad (2.12)$$

Usually, this model is called the KdV equation. This model was proposed to explain shallow water surface waves by Diederik Korteweg and Gustav de Vries (Korteweg and de Vries 1895) [128]². It is particularly noteworthy that KdV is exactly solvable, that is, a nonlinear partial derivative equation whose solutions can be exactly and with calculated precision an integrable system.

Let us consider the moving system $\tau = t$ and $\zeta = \xi - vt$, then

$$0 = \partial_{\xi} \left(-\gamma \partial_{\xi \xi \xi} u - \frac{u^2}{2} + vu \right). \quad (2.13)$$

If the system does not have external flows, the constant of integration of the previous equation is zero. Then, the stationary solutions of this system satisfy the following Newton-type equation

$$\gamma \partial_{\xi \xi \xi} u = vu - \frac{u^2}{2}. \quad (2.14)$$

The equilibria of this system are $u = 0$ and $u = 2v$. Linear analysis around the origin tells us that this is a center ($u = 2v$) and that the other equilibrium is a hyperbolic point

²the first time the KdV equation is derived is by Boussinesq [33].

($u = 0$). In Figure 2.8, the respective phase space is illustrated. Where the equilibria represent the uniform states, only the hyperbolic equilibrium point is stable, the orbits around the center account for propagative periodic solutions. The solutions of equation (2.14) can all be calculated analytically by means of elliptic functions [8]. However, these solutions are unstable for the spatiotemporal system. The most attractive solution is the homoclinic solution that connects the stable and unstable variety, respectively, of the hyperbolic point. This solution accounts for a solitary wave (see figure 2.8). This wave is a stable solution of the space-time system. The homoclinic can be obtained by direct integration of the Newton-type equation (2.14), which has the solution (solitary wave)

$$u(\zeta - v\tau) = 3v \operatorname{sech}^2 \left[\sqrt{\frac{v}{4\gamma}} (\zeta - v\tau) \right]. \quad (2.15)$$

The previous solution is illustrated in Figure 2.8. We note that for the larger amplitude of the localized solution, the speed is more significant and the relationship between them is given by a power law of the square root type. Then solitary waves of greater amplitude trap the smaller solitons (see figure 2.8). Because the equation is nonlinear, the superposition principle is not valid. When the solitons collide, the amplitude of the largest decreases and that of the smallest increases and also the largest and smallest one is ahead and behind in their movement, respectively.

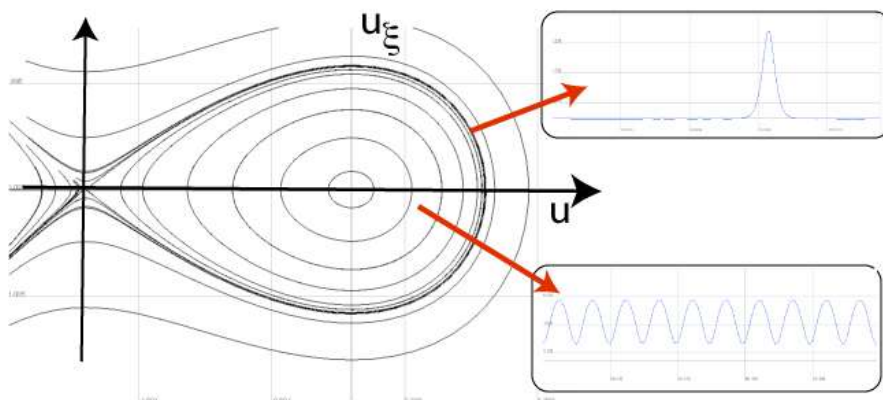


Figure 2.7: Phase space of the Newton-type equation (2.14). Periodic solutions account for periodic waves. propagative and the homoclinic accounts for a localized wave.

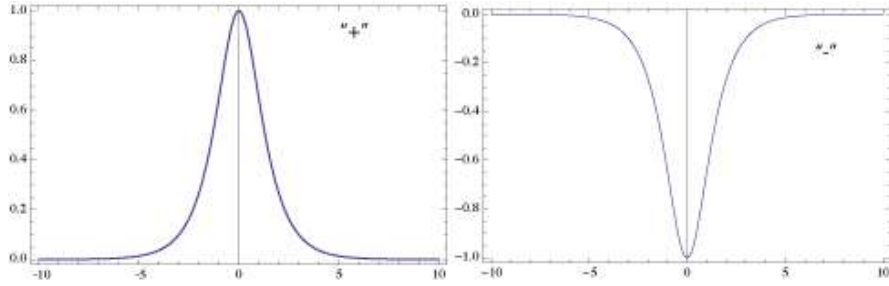


Figure 2.8: Bright and dark solitons obtained from the KdV equation (2.13) for positive and negative nonlinearity.

By introducing the field $u(x, t)$ we have succeeded in deducing the Korteweg and de Vries equation, equation (2.13), which has solitary waves like those illustrated in figure (2.6). In the case of considering a reflection in the field $u(x, t)$ of the form $u \rightarrow -u$, the KdV equation is only modified by means of the change of sign of the nonlinear term

$$\partial_\tau u = -\gamma \partial_{\zeta\zeta\zeta} u + u \partial_\zeta u. \quad (2.16)$$

This equation now exhibits depletion solitons, often referred to in the literature as *dark solitons*, particularly in the context of nonlinear optics, which are associated with the optical medium being of the focusing type. Then, we will say that when this sign is positive (negative), the medium is of the focusing (defocusing) type.

2.2.2 Dynamics of counterpropagating solitons: Boussinesq equation

The Boussinesq equation (2.9) is invariant by spatial reflection, $x \rightarrow -x$. Unlike the KdV model (2.13), which accounts for nonlinear waves propagating towards a given flank³. Therefore, a finite localized perturbation of the Boussinesq equation is characterized by the emergence of counterpropagating solitons to the left and to the right. Figure 2.9 illustrates the propagation of a disturbance for the Boussinesq equation. In order to describe this dynamic, let us consider an ansatz analogous to the one we use

³It is worthy to note that this model has broken the symmetry of spatial reflection.

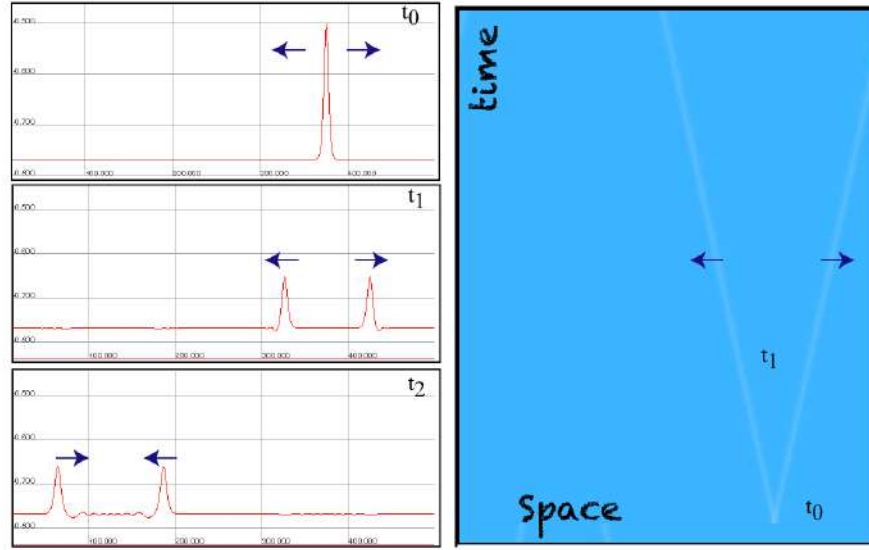


Figure 2.9: Propagation of two counterpropagating solitons of the Boussinesq equation (2.9). The panels on the left side show different instants of the profile ($t_0 < t_1 < t_2$). The right panel gives an account of the space-time evolution of the solitons.

to describe the traveling wave to the right flank

$$u(x, t) = \epsilon f [\zeta = \epsilon^{1/2}(x - ct), T = \epsilon^{3/2}t] + \epsilon g [\theta = \epsilon^{1/2}(x + ct), T] + \epsilon^2 w(\zeta, \theta, T), \quad (2.17)$$

where $\epsilon \ll 1$ is a multiple scaling control parameter [122] and w is a small correction function. Introducing the previous ansatz in Eq. (2.9), we obtain a hierarchy of equations in powers of ϵ . Note that differential operators are calculated using the following rules

$$\frac{\partial}{\partial t} = \frac{\partial}{\partial \zeta} \frac{\partial \zeta}{\partial t} + \frac{\partial}{\partial \theta} \frac{\partial \theta}{\partial t} + \frac{\partial}{\partial T} \frac{\partial T}{\partial t} = -\epsilon^{1/2}c \frac{\partial}{\partial \zeta} + \epsilon^{1/2}c \frac{\partial}{\partial \theta} + \epsilon \frac{\partial}{\partial T}, \quad (2.18)$$

$$\frac{\partial}{\partial x} = \frac{\partial}{\partial \zeta} \frac{\partial \zeta}{\partial x} + \frac{\partial}{\partial \theta} \frac{\partial \theta}{\partial x} = \epsilon^{1/2} \frac{\partial}{\partial \zeta} + \epsilon^{1/2} \frac{\partial}{\partial \theta}. \quad (2.19)$$

At the order ϵ^2 , we get a trivial equality

$$c^2 \partial_{\zeta \zeta} f + c^2 \partial_{\theta \theta} g = c^2 \partial_{\zeta \zeta} f + c^2 \partial_{\theta \theta} g. \quad (2.20)$$

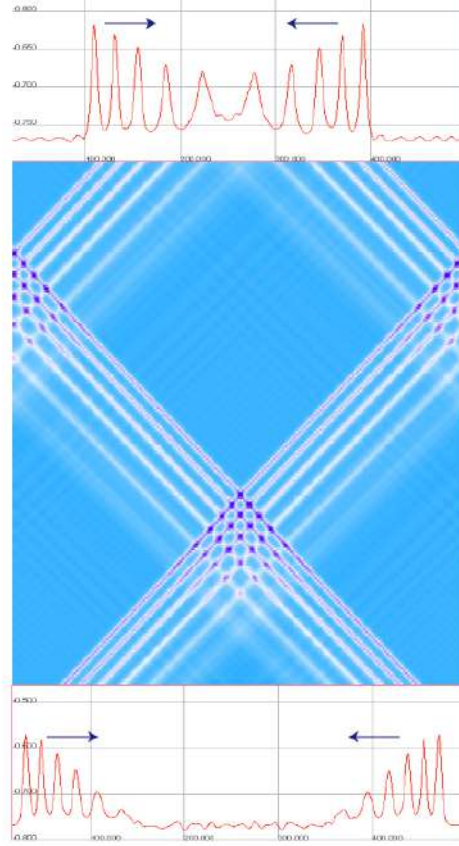


Figure 2.10: Gas evolution of counterpropagating solitons of the Boussinesq equation (2.9). The lower and upper panels give an account of the initial and final conditions.

To the next order ϵ^3 , we obtain the linear equation

$$\begin{aligned} \partial_{\zeta\theta} w - 2c\partial_{\zeta T} f + 2c\partial_{\theta T} g &= \partial_{\zeta}(f\partial_{\zeta} f) + \partial_{\theta}(g\partial_{\theta} g) \\ &+ g\partial_{\zeta\zeta} f + f\partial_{\theta\theta} g + \gamma\partial_{\zeta\zeta\zeta} f + \gamma\partial_{\theta\theta\theta} g, \end{aligned} \quad (2.21)$$

we can write the previous equation as follows

$$\begin{aligned} \partial_{\zeta\theta} w(\theta, \zeta) &= \partial_{\zeta}(2c\partial_T f + f\partial_{\zeta} f + \gamma\partial_{\zeta\zeta} f) + \partial_{\theta}(-2c\partial_T g + g\partial_{\theta} g + \gamma\partial_{\theta\theta} g) + \\ &+ g(\theta)\partial_{\zeta} f(\zeta) + f(\zeta)\partial_{\theta} g(\theta). \end{aligned} \quad (2.22)$$

To solve this linear equation for w , we introduce an inner product $\langle h(\zeta, \theta) | p(\zeta, \theta) \rangle \equiv \int h(\zeta, \theta) p(\zeta, \theta) d\theta d\zeta$. Using this inner product the linear operator $\mathcal{L} = \partial_{\zeta\theta}$ is self-adjoint, $\mathcal{L} = \mathcal{L}^\dagger$. The element of the kernel of \mathcal{L} , $\mathcal{L}\psi = 0$, is any function of a single variable,

that is, $\psi(\zeta, \theta) = \psi(\theta)$ or $\psi(\zeta, \theta) = \psi(\zeta)$. Then applying the solvability condition of the previous equation [95], we obtain

$$-2c\partial_T f = f\partial_\zeta f + \gamma\partial_{\zeta\zeta} f, \quad (2.23)$$

$$2c\partial_T g = g\partial_\theta g + \gamma\partial_{\theta\theta} g. \quad (2.24)$$

The solvability condition is equivalent to imposing that the w function must explicitly depend on both variables. Therefore, both functions f and g satisfy two independent equations of KDV. From the previous model, we conclude that solitons that propagate in opposite directions do not interact. Figure 2.10 shows the temporal evolution of a soliton gas. From this chart, we conclude that the vortices that propagate in the opposite direction are non-interacting at the dominant order.

2.2.3 Solitary waves in fluidized granular matter

Granular matter, when fluidized by continuous energy injection exhibits a variety of phenomena that resemble those of molecular fluids like waves propagation, pattern formation, and phase transition, to mention a few. The main difference with molecular fluids is that, at collisions, grains dissipate kinetic energy into the internal degrees of freedom of grains. Hence, energy must be supplied continuously to sustain a fluidized

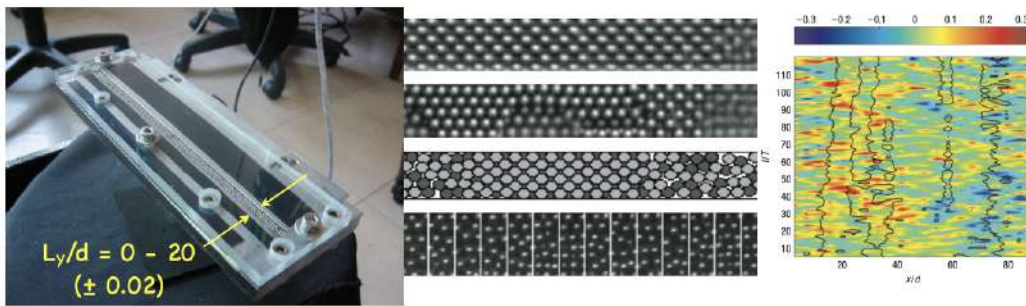


Figure 2.11: Liquid-solid-like transition in quasi-one-dimensional driven granular media [51]. In the left, middle, and right panel are a snapshot of the experiment, snapshots of the phase separation, and a spatiotemporal diagram illustrating the propagation of waves.

regime. Experimentally, energy is usually injected through vibrating walls or by the gravitational field. It has been shown that a fluidized granular system in two spatial dimensions with a vibrating wall and without gravity exhibits a phase separation [12, 36, 38, 51, 143], analogous to the spinodal decomposition of the gas-liquid transition in the van der Waals model [134]. Molecular dynamics simulations of a granular system at the onset of phase transition reveal a rich dynamical behavior characterized by appearance, coalescence, and disappearance of bubbles (or clusters). The mechanism for this phase separation is triggered by a negative compressibility [12, 38]. Namely, the origin of this phase separation is of mechanical origin.

A continuous macroscopic description of granular flows is still an open fundamental question. There are several models with different approximation schemes that produce different hydrodynamic models. Nevertheless, using simple generic arguments, independent of the specific macroscopic model, in Refs. [12, 38] it is shown that a fluidized granular system that exhibits phase separation can be described, close to the critical point, in a quite good agreement by *the van der Waals normal form (VdW)*. This model shows that the appearance, coalescence, interaction, and disappearance of bubbles is mediated by nonlinear waves.

The VdW normal form is [12, 38]

$$\partial_{tt}u = \partial_{xx}(\varepsilon u + u^3 - \partial_{xx}u + \nu\partial_t u), \quad (2.25)$$

where $u(x, t)$ is the field that describes the correction to the critical average vertical density, x is the coordinate that describes the horizontal direction of the granular system, ε is the bifurcation parameter which is proportional to the compressibility coefficient, ν is the effective viscosity. The two first terms in the right hand side give account of the pressure around the critical average vertical density. The term with high spatial derivative depicts the interface tension [38]. It is important to note that this model is similar to the Boussinesq equation (2.9) but with cubic nonlinearity.

The inviscid VdW model, $\nu = 0$, has the form $\partial_{tt}u = \partial_{xx}(\varepsilon u + u^3 - \partial_{xx}u)$. In the moving framework, $\zeta = x - ct$, the stationary solutions satisfy a Newton-type equation

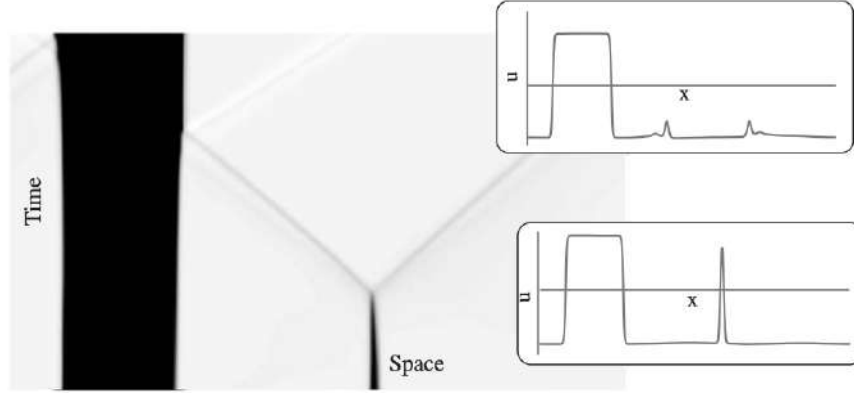


Figure 2.12: Spatiotemporal evolution of the VdW model at the onset of the phase transition, with time running up. The gray scale is proportional to the field u , with darker regions representing denser regions in the system. The inset figures illustrate two different snapshots before and after solitary wave emission.

of the form

$$\frac{d^2u}{d\zeta^2} = (\varepsilon - c^2)u + u^3 - \lambda, \quad (2.26)$$

where λ is an integration constant related to the total mass, compatible with periodical or zero flux boundary conditions. The equilibrium fixed points (u_0) of this system satisfy $\lambda = (\varepsilon - c^2)u_0 + u_0^3$. It is easy to show that, when $|\lambda| < 2(c^2 - \varepsilon)/3\sqrt{3}$ and $\varepsilon < c^2$, this cubic equation has three real solutions, otherwise it just has one equilibrium. In the first case, two of them are hyperbolic fixed points, while the other is a center fixed point. Then, Newton-type equations in general, have an homoclinic curve, which corresponds to a traveling solitary wave of the inviscid VdW model. To have a solitary wave solution, we must impose

$$u_0^2 + \varepsilon < c^2 < v_s^2 \equiv 3u_0^2 + \varepsilon. \quad (2.27)$$

Hence, the wave speed is bounded. v_s is the sound speed about the homogeneous state u_0 , therefore the *solitary waves are subsonic*. Due to the symmetry of $\lambda \rightarrow -\lambda$ and $u \rightarrow -u$, we will suppose without loss of generality $\lambda > 0$. In that case, the homoclinic orbit lies below the negative state $u_0 < 0$ (the lowest fixed point). And we have *bright*

solitary wave solutions [49]

$$u = u_0 + \frac{2(3u_0^2 + \varepsilon - c^2)}{\sqrt{2(c^2 - u_0^2 - \varepsilon)} \cosh \left[\sqrt{3u_0^2 + \varepsilon - c^2} ((x - x_0) - ct) \right]} - 2u_0 \quad (2.28)$$

In the opposite case, $\lambda < 0$, we have *dark solitary wave solutions*, which hold up the upper fixed point. In the limiting case, $\lambda = 0$, there are two heteroclinic connections. Hence, we have kink or anti-kink solutions. Figure 2.12 illustrates the solitary wave solution.

2.3 Chain of coupled pendulums

Nonlinear oscillators such as the pendulum have played a primary role in the understanding of complex dynamics since the dawn of modern science [16, 98]. Even a simple two-oscillators coupled system shows interesting behavior such as synchronization [171]. A chain of coupled oscillators to nearest neighbors also can present a rich spatiotemporal dynamics [171, 130, 117], such as phase turbulence [130], synchronization [171], defects turbulence [180], random occurrence of coherence events [151], defect-mediated turbulence [71], spatiotemporal intermittency [41], quasiperiodicity in extended system [62] and coexisting of coherent and incoherent behavior, known as chimera states [65, 67]. A prototype model of coupled nonlinear oscillators to nearest neighbors is the Frenkel-Kontorova model [35, 127]. Figure 2.13 illustrates a chain of coupled pendula. In the context of condensed matter, it is the simplest model that describes the dynamics of a chain of particles interacting with the nearest neighbors under the influence of an external periodic potential [35, 127]. The Frenkel-Kontorova has been used to model several nonlinear phenomena such as solitons, kinks, breathers, and glass-like behavior. Likewise, this model has been used to describe cluster of atoms in DNA-like chain, spin in magnetic chain, fluxon in coupled Josephson junctions and plastic deformations in metals (see textbook [35] and references therein).

Let us consider a chain of dissipative coupled pendulums, which is described by the damped Frenkel- Kontorova equation, Let us consider a chain of dissipative coupled

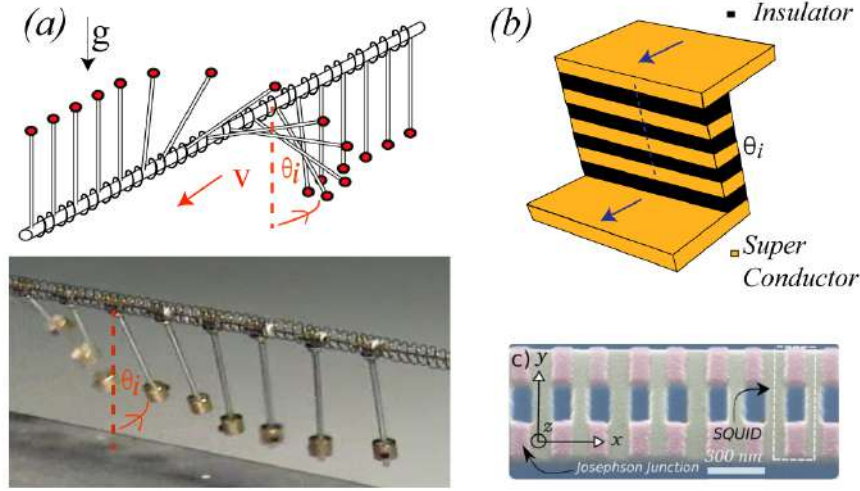


Figure 2.13: Frenkel-Kontorova model. (a) Schematic representation and snapshot of a chain of coupled pendulums. (b) Schematic representation and snapshot of a coupled Josephson junctions.

pendula, which is described by the damped Frenkel-Kontorova equation,

$$\ddot{\theta}_i = -\omega^2 \sin \theta_i - \mu \dot{\theta}_i + \kappa (\theta_{i+1} - 2\theta_i + \theta_{i-1}), \quad (2.29)$$

where $\theta_i(t)$ is the angle formed by the pendulum and the vertical axis in the i -position at time t , $\theta_i = 0$ ($\theta_i = \pi$) corresponds to upright (upside-down) position of pendulum. i is the index label of the i -th pendulum, ω is the pendulum natural frequency, μ accounts for the damping coefficient, and κ stands for the coupled interaction between adjacent pendulums. Notice each pendulum is coupled to the nearest neighbors. The model Eq. (2.29) can be also applied to coupled identical Josephson junctions [42, 138]. A scheme of this system is depicted in Fig. 2.13b, where $\theta_i(t)$ accounts for the phase difference between the wave function of each superconductors in the i -th junction.

To model these quantum elements, one can consider a quantum system consisting of two superconductors described by two wave functions ψ_1 and ψ_2 which is separated by an insulating film (see Fig. 4.2). When one applies a voltage difference, classically one does not expect to observe electrical conduction, however, quantitatively one observe a current through the device, even without voltage. To describe this phenomenon, one

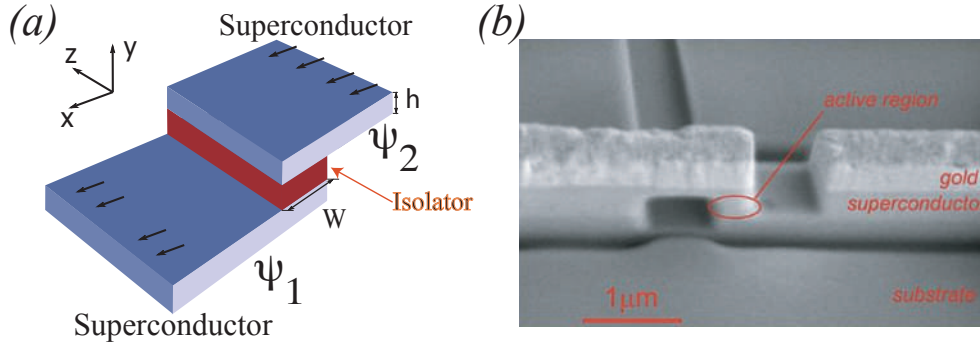


Figure 2.14: Josephson junctions. (a) Schematic representation of the Josephson junctions. ψ_1 and ψ_2 account for the amplitude probability of the superconductor state of the respective superconductor. (b) snapshots of the Josephson junction

can consider a two-state quantum system described by

$$i\hbar\partial_t\psi_1 = E_1\psi_1 + k\psi_2, \quad (2.30)$$

$$i\hbar\partial_t\psi_2 = E_2\psi_2 + k\psi_1, \quad (2.31)$$

where \hbar is the Planck constant, E_1 and E_2 account for the energy of the superconductor, $E_2 - E_1 = -qV$, where V is the voltage between superconductors and q the electrical charge, and k accounts for the coupling between superconductors, which is determined by the properties and geometry of the insulating material. Introducing polar representation $\psi_l(t) \equiv \sqrt{\rho_l(t)}e^{i\phi_l(t)}$ ($l = \{1, 2\}$), where $\rho_l(t)$ accounts for the density of cooper pair, the set of equations read

$$\partial_t\rho_1 = \frac{k\sqrt{\rho_2\rho_1}}{\hbar} \sin(\phi_2 - \phi_1), \quad (2.32)$$

$$\partial_t\rho_2 = -\frac{k\sqrt{\rho_2\rho_1}}{\hbar} \sin(\phi_2 - \phi_1), \quad (2.33)$$

$$\partial_t\phi_1 = -\frac{E_1}{\hbar} - \frac{k}{\hbar} \sqrt{\frac{\rho_2}{\rho_1}} \cos(\phi_2 - \phi_1), \quad (2.34)$$

$$\partial_t\phi_2 = -\frac{E_2}{\hbar} - \frac{k}{\hbar} \sqrt{\frac{\rho_1}{\rho_2}} \cos(\phi_2 - \phi_1). \quad (2.35)$$

the current between superconductors is given by

$$J_s \equiv \partial_t\rho_1 = -\partial_t\rho_2 = \frac{k\sqrt{\rho_2\rho_1}}{\hbar} \sin(\phi_2 - \phi_1). \quad (2.36)$$

Hence, if there is a phase difference $\phi \equiv \phi_2 - \phi_1$ between the superconductors, there is a current. This phase difference satisfies

$$\partial_t \phi = \frac{qV}{\hbar} - \frac{k}{\hbar} \cos(\phi) \left[\sqrt{\frac{\rho_2}{\rho_1}} - \sqrt{\frac{\rho_1}{\rho_2}} \right]. \quad (2.37)$$

Considering that both states have the same density $\rho_0 \equiv \rho_1 = \rho_2$, one finds Josephson's relationships

$$J_s = \frac{k\rho_0}{\hbar} \sin(\phi), \quad (2.38)$$

$$\partial_t \phi = \frac{qV}{\hbar}. \quad (2.39)$$

Note that even without voltage ($V = 0$), but with a phase difference, one can see a quantum current (*Josephson effect*). On the other hand, the current and the voltage are connected by means of Maxwell equations, particularly by

$$\left(\frac{\partial_{tt}}{c^2} - \nabla^2 \right) \vec{E} = \mu_0 \partial_t \vec{J}, \quad (2.40)$$

where \vec{E} and \vec{J} are the electric field and current between the superconductor, respectively. If the insulator is a thin film then $\vec{E} \approx -V/d \hat{y}$ with d the thickness of the insulator, and the current is composed of a normal and a superconductor current, $\vec{J} = (J_s + J_n)\hat{y}$. The normal current satisfies the Ohm law $J_n = -V/\eta d$ with η is the resistivity. Using the Maxwell equation, Josephson relations, the previous approximation and assuming that phase difference depend of the transversal coordinate $\phi(x, t)$, one gets

$$\partial_{tt}\phi = -\frac{c^2 k \rho_0 d \mu_0}{\hbar^2 q} \sin \phi - \frac{c^2 \mu_0}{\eta} \partial_t \phi + c^2 \partial_{xx} \phi. \quad (2.41)$$

Hence, the Josephson junctions is describe by sine-Gordon equation, where the natural frequency depends of the density of cooper pairs, electric charge, constant of coupled between the superconductor, and the thickness of the insulator. Hence, in the sine-Gordon equation (2.43) the parameter ω^2 stands for the superconductor current in the junctions, and its value is determined by the particular characteristics of the junction. The parameter μ accounts for the normal current and the parameter k accounts for the

coupling between nearest junctions. Likewise, the model Eq. (2.29) accounts for the coupling superconducting quantum interference devices (SQUIDS, see [42] and references therein). In this latter case, θ_i accounts for the magnetic flux over i -th SQUIDS. These devices have played a fundamental role in detecting small magnetic fields in prospecting for mineral deposits, magnetoencephalography, and cosmic waves [42].

2.3.1 sine-Gordon Equation

In the continuous limit, considering $\theta(x, t) = \lim_{dx \rightarrow 0} \theta_i(t)$, $x = \lim_{dx \rightarrow 0} idx$, $\kappa \rightarrow \infty$, and $\kappa dx^{-2} \rightarrow C^2$ (C is a finite constant that stand for the elastic coefficient), equation (2.29) becomes in the damped sine-Gordon equation [76].

$$\partial_{tt}\theta = -\omega^2 \sin \theta - \mu \partial_t \theta + C^2 \partial_{xx}\theta. \quad (2.42)$$

When we neglect the damping effect $\mu = 0$, the system is described by the sine-Gordon equation [76].

$$\partial_{tt}\theta = -\omega^2 \sin \theta + C^2 \partial_{xx}\theta. \quad (2.43)$$

It was originally introduced by Edmond Bour (1862) in the course of study of surfaces of constant negative curvature as the Gauss-Codazzi equation for surfaces of curvature [32] and rediscovered by Frenkel and Kontorova (1939) in their study of crystal dislocations known as the Frenkel-Kontorova model [35, 127]. The trivial solution is that the pendulums are in the upright state, $\theta = 0$. By uniformly disturbing the pendulums, with small amplitud, they all oscillate close to the natural omega frequency which depends on the square root of the length established by Galileo Galilei [98]. Figure 2.15 shows the spatiotemporal evolution of a uniform disturbance of small and long amplitude. Therefore, for small amplitudes, we conclude that the pendulums can be synchronized [171]. Conversely, when the coupled oscillators are near the homoclinic bifurcation of an elementary oscillator, the synchronization becomes unstable [12]. Namely, the previous phenomenon corresponds to the emergence of space-time chaos by a homoclinic bifurcation, a phenomenon established for low-dimensional systems by Andronov [7].

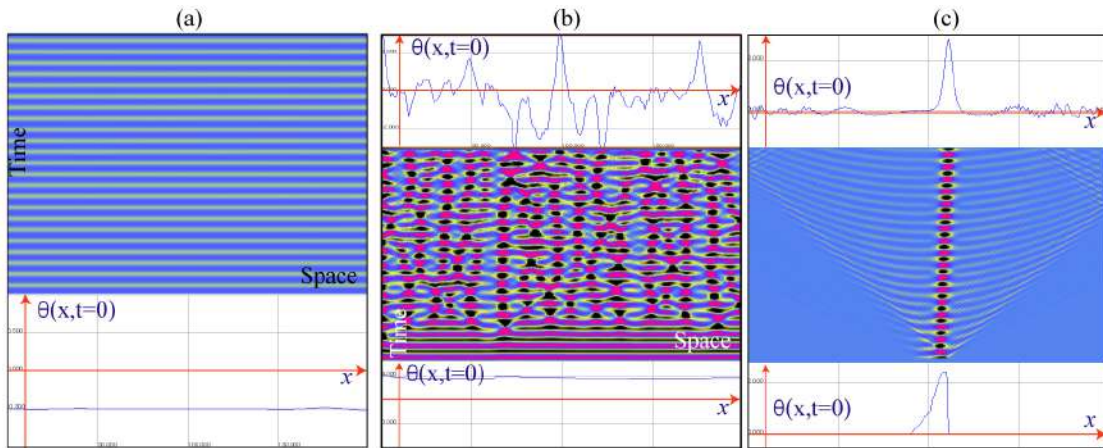


Figure 2.15: Numerical simulation of sine-Gordon equation (2.43) with $\omega = 1$ and $C = 1$. The lower and upper panels account for the initial and final conditions, respectively. Spatiotemporal evolution of a small (a) and large (a) uniform angle amplitude initial condition. (c) Spatiotemporal diagram of an asymmetrical localized initial condition.

Unexpectedly, the last scenario changes when one makes an asymmetrically localized disturbance, which generates a solitary wave that spreads surrounded by a sea of waves of small amplitude. Figure 2.15c shows the spatiotemporal diagram of a localized disturbance. Depending on the initial conditions, we observe different speeds of propagation of the solitary waves. Observe that these waves always have a bell-like shape.

To shed light on the observed dynamics, let us consider the dynamics of the sine-Gordon equation (2.43) around the upright pendula, $\theta \ll 1$, that is,

$$\partial_{tt}\theta = -\omega^2\theta + C^2\partial_{xx}\theta. \quad (2.44)$$

This equation is known in the literature as the Klein-Gordon equation [105, 126]. Proposed scalar model to describe the relativistic quantum mechanics of electrons; however, electrons have spin, the correct theory of electron is the Dirac equation [84]. From a point of view of quantum mechanics, this model describes particles with mass without spins, so it adequately describes pions and Higgs bosons.

The origin of the name of the sine-Gordon equation is simply the sine of the above equation [76]. The Klein-Gordon equation (2.44) is a dispersive linear wave equation.

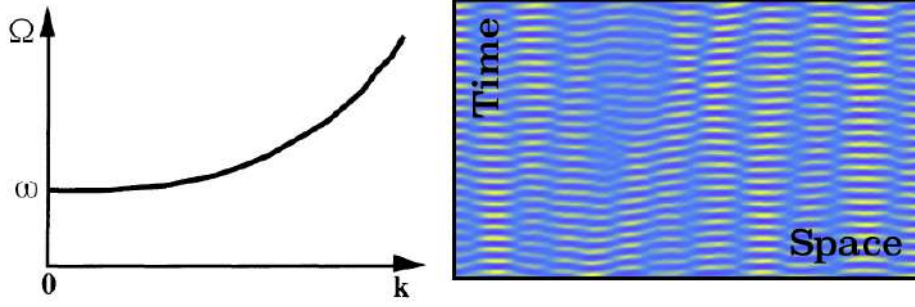


Figure 2.16: Dispersion relationship of the Klein-Gordon equation (2.45) and space-time evolution of waves.

Let us consider the following ansatz $\theta = Ae^{i(\Omega t - kx)}$, we obtain the relation dispersion

$$\Omega = \sqrt{\omega^2 + C^2 k^2}. \quad (2.45)$$

Figure 2.17 shows the relation dispersion and spatiotemporal evolution of waves in the sine-gordon Equation. Therefore, this model has a cutoff frequency equal to ω ; that is, only waves with higher frequencies are allowed. Frequencies lower than ω have imaginary wave numbers, so they are waves that are damped. Another important property of sine-Gordon and Klein-Gordon is that they are invariant under Lorentz transformation

$$x' = \frac{x - vt}{\sqrt{1 - \frac{v^2}{C^2}}} \quad \text{and} \quad t' = \frac{t - \frac{vx}{C^2}}{\sqrt{1 - \frac{v^2}{C^2}}}, \quad (2.46)$$

where $v < C$ is an arbitrary speed. To show this property, let us rewrite the sine Gordon equation as follows

$$(\partial_{tt} - C^2 \partial_{xx})\theta = (\partial_t - C\partial_x)(\partial_t + C\partial_x)\theta = -\omega^2 \sin \theta. \quad (2.47)$$

Using the Lorentz transformation one have

$$\frac{\partial}{\partial t} = \frac{\partial}{\partial t'} \frac{\partial t'}{\partial t} + \frac{\partial}{\partial x'} \frac{\partial x'}{\partial t} = \frac{1}{\sqrt{1 - \frac{v^2}{C^2}}} \left(\frac{\partial}{\partial t'} - v \frac{\partial}{\partial x'} \right), \quad (2.48)$$

$$\frac{\partial}{\partial x} = \frac{\partial}{\partial t'} \frac{\partial t'}{\partial x} + \frac{\partial}{\partial x'} \frac{\partial x'}{\partial x} = \frac{1}{\sqrt{1 - \frac{v^2}{C^2}}} \left(\frac{\partial}{\partial x'} - \frac{v}{C^2} \frac{\partial}{\partial t'} \right). \quad (2.49)$$

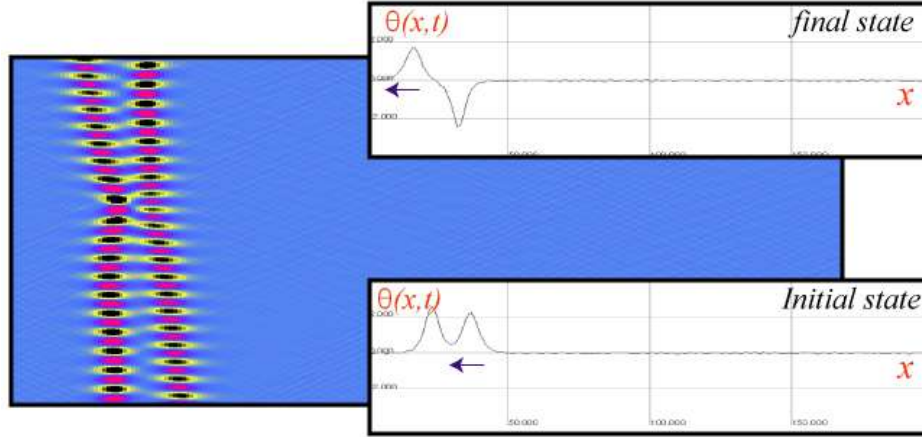


Figure 2.17: Collisions of breather solitons in the sine-Gordon equation (2.43) with $\omega = 1$ and $C = 1$. The insets show the initial and final conditions, respectively.

It is trivial to show that

$$(\partial_t - C\partial_x)(\partial_t + C\partial_x) = (\partial_{t'} - C\partial_{x'})(\partial_{t'} + C\partial_{x'}). \quad (2.50)$$

Hence, the sine-Gordon equation is invariant under the Lorentz boost. Namely, any solution of the sine-Gordon can be propagative when applying this transformation.

2.3.2 Breather solitons and weak nonlinear analysis

As illustrated in Figure 2.15, the system exhibits localized propagative oscillatory solutions, *breather solitons* [1]. This intriguing dynamical behavior was characterized analytically by using the inverse scattering method [1]. The breather solitons have the expression [185]

$$\theta(x, t) = 4 \arctan \left[\frac{\sqrt{1 - \Omega^2}}{\Omega} \operatorname{sech} \left(\sqrt{1 - \Omega^2} \frac{x - vt}{\sqrt{1 - \frac{v^2}{C^2}}} \right) \sin \left(\Omega \frac{t - \frac{vx}{C^2}}{\sqrt{1 - \frac{v^2}{C^2}}} \right) \right] \quad (2.51)$$

where Ω accounts for the amplitude and size of the soliton. In other words, solitons are a family of solutions parameterized by Ω . For small disturbances, the solitons have bell-like shapes, as illustrated in figure 2.15. Notice that in this limit, the system has some similarities with the solitons observed in the Boussinesq and Korteweg de Vries

equation. To emphasize this, we consider in figure 2.17 the collision of two solitons with different speed and amplitude. From this chart, we conclude that the solitons collide in a non-linear way so that there is a displacement of the solitons when they collide, similar to that observed in Korteweg de Vries.

In order to achieve a better understanding of this type of solitons and to describe them in a universal manner, we will now consider the weakly nonlinear analysis. Let us consider the ansatz

$$\theta(x, t) = A(X, T)e^{i\omega t} + \bar{A}(X, T)e^{-i\omega t} + W(A, \bar{A}, t), \quad (2.52)$$

where A is a slowly variable amplitude in time and space ($\partial_{TT}A \ll \omega\partial_TA \ll \omega^2A$ and $\partial_{XX}A \ll (C/\omega)\partial_XA \ll (C/\omega)^2A$), which accounts for the envelope concerning the upright position of the pendulum. X , T , and t account for the slow spatial and temporal variable and the fast temporal variable, respectively. \bar{A} stand for the complex conjugate of the amplitude A . W accounts for nonlinear corrections in the amplitude.

Introducing the ansatz (2.52) in equation (2.43) and linearizing in w , one obtain

$$\begin{aligned} \partial_{tt}\theta &= -\omega^2 A e^{i\omega t} + i2\omega\partial_TA e^{i\omega t} + \partial_{TT}A e^{i\omega t} + \partial_{tt}W + c.c. \\ &= -\omega^2 \sin\theta + C^2\partial_{xx}\theta \approx -\omega^2\left(\theta - \frac{\theta^3}{6}\right) + C^2\partial_{xx}\theta \\ &\approx -\omega^2 W - \omega^2 \left(A e^{i\omega t} - \frac{A^3 e^{i3\omega t} + 3|A|^2 A e^{i\omega t}}{6} \right) + C^2\partial_{XX}A e^{i\omega t} + c.c, \end{aligned} \quad (2.53)$$

where the symbol $c.c.$ accounts for complex conjugate. Considering the dominate terms the above equation reads

$$(\partial_{tt} + \omega^2)W = \left(-i2\omega\partial_TA + \omega^2\frac{|A|^2 A}{2} + C^2\partial_{XX}A \right) e^{i\omega t} + \frac{\omega^2 A^3 e^{i3\omega t}}{6} + c.c. \quad (2.54)$$

To solve the linear equation in W , one can introduce the inner product (Fourier product)

$$\langle f|g \rangle = \frac{\omega}{2n\pi} \int_T^{T+n\frac{2\pi}{\omega}} \bar{f}(t)g(t)dt, \quad (2.55)$$

the linear operator $\mathcal{L} \equiv \partial_{tt} + \omega^2$ is self-adjoint. The element of the kernel of \mathcal{L} are of the form $\{e^{i\omega t}, e^{-i\omega t}\}$. Therefore, for the linear equation (2.54) to have a solution–solvability

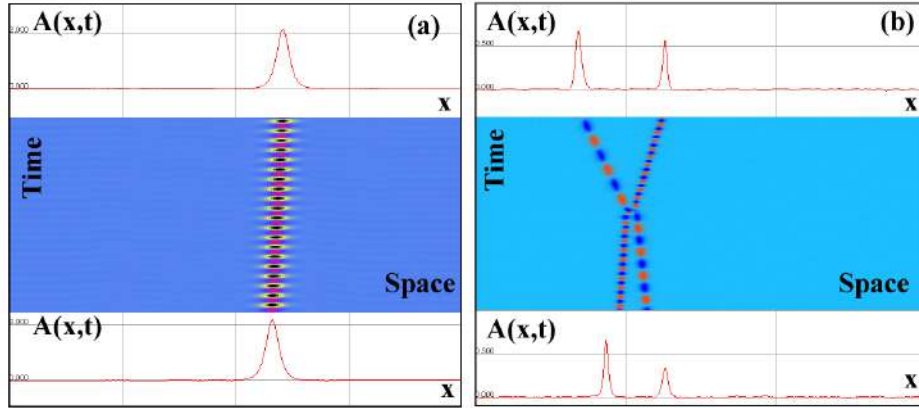


Figure 2.18: Solitons in the nonlinear Schrödinger equation (2.56) (a) Spatiotemporal evolution of solitary wave propagation. (b) counter propagative solitons collision. Top and bottom panels stand for the initial final condition.

condition [95]—the elements on the right side must not be proportional to $e^{i\omega t}$ or $e^{-i\omega t}$. Hence, the amplitude satisfies (*Nonlinear Schrödinger equation*, NLS [39, 94, 156, 164, 150, 195])

$$\partial_T A = -i\omega \frac{|A|^2 A}{4} - i \frac{C^2}{2\omega} \partial_{XX} A. \quad (2.56)$$

2.3.3 Nonlinear Schrödinger equation

Renormalizing space and the amplitude the above equation (2.56) can be written as

$$i\partial_T A = |A|^2 A + \partial_{XX} A. \quad (2.57)$$

This model is a nonlinear variation of the Schrödinger equation [39, 94, 156, 164, 150, 195]. Due to this model describes the envelope of coupled oscillators it has been used to describe the propagation of light in nonlinear optical fibers [3, 164], planar waveguides and Bose-Einstein condensates [173], small-amplitude gravity waves on the surface of deep inviscid fluid, and the Langmuir waves in hot plasmas [24]. The nonlinear Schrödinger equation (2.56) is not Lorentz invariant. However, this is invariant under

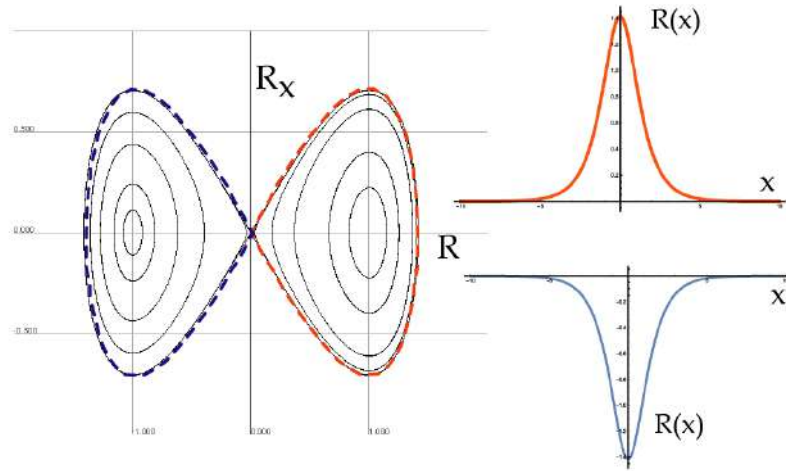


Figure 2.19: Phase space of the stationary system associated with the the nonlinear schrödinger equation (2.56). The red and blue curves account for bright and dark soliton.

the Galileo transformation

$$x \rightarrow x' = x + 2vt, \quad (2.58)$$

$$t \rightarrow t' = t, \quad (2.59)$$

$$A(x, t) \rightarrow A(x, t) = A'(x' - 2vt', t')e^{iv(x'-vt')}, \quad (2.60)$$

where A' satisfied the nonlinear schrödinger equation in the co-moving system $\{x', t'\}$. Hence, one found solutions of the NLS equation can inhibit propagative solutions.

When performing localized perturbations of the NLS equation, one observes the emergence of solitary waves, solitons. Figure 2.18 shows the typical soliton observed in the Nonlinear Schrödinger equation (2.56). To shed light on this solution, let us consider the following ansatz for the amplitude

$$A = R(x)e^{-i\omega_0 t}, \quad (2.61)$$

where R and ω_0 stand for the magnitud and oscillatory frequency of the amplitude, respectively. The magnitud of the amplitude satisfies (Newton type equation)

$$\partial_{xx}R = \omega_o R - R^3, \quad (2.62)$$

The trivial equilibria in this equation are $R = 0$ and $R = \sqrt{\omega_0}$, which is a hyperbolic and center equilibrium, respectively. The phase space of this equation is illustrated in figure 2.19. The only hyperbolic curve is the homoclinic curves, which represent the solitons. To account for this curve, we use the ansatz

$$\begin{aligned} R &= a \operatorname{sech}(bx), \quad \partial_x R = -ab \tanh(bx) \operatorname{sech}(bx), \\ \partial_{xx} R &= ab^2 \tanh^2(bx) \operatorname{sech}(bx) - ab^2 \operatorname{sech}^3(bx). \end{aligned} \quad (2.63)$$

The last relation can be rewritten as $\partial_{xx} R = ab^2 \operatorname{sech}(bx)[1 - 2\operatorname{sech}^2(bx)]$. Replacing these expressions in Eq. (2.62), one gets

$$ab^2 \operatorname{sech}(bx)[1 - 2\operatorname{sech}^2(bx)] = \omega_o a \operatorname{sech}(bx) - a^3 \operatorname{sech}^3(bx). \quad (2.64)$$

Equating the terms in the different powers of secants, it obtains $b = \sqrt{\omega}$ and $a = \sqrt{2\omega}$. Hence, the homoclinic curve has the form $R = \sqrt{2\omega} \operatorname{sech}(\omega x)$. Using the Galileo transformation (2.60) and the ansatz (2.61), the soliton has the form

$$A(x - 2vt, t, v, \omega_o) = \sqrt{2\omega_o} \operatorname{sech}[\omega_o(x - vt)] e^{i\omega_o t} e^{iv(x-vt)}, \quad (2.65)$$

where the solitons are parameterized by a family of two parameters ω and v . ω characterizes the height and width of the soliton, for larger, thicker, and thinner ω is the soliton. v characterizes the speed of propagation of the solitons. Figure 2.18 shows the typical soliton observed in the Nonlinear Schrödinger equation (2.56). Likewise, as the examples previously studied, solitons correspond to solitary waves that propagate without deformation, characterized by the fact that when they collide with other solitons, a shift of the position of the solitary waves occurs [177].

Based on weakly nonlinear analysis, Zakharov [211] shows that the envelope deep-water wave train is described by the nonlinear Schrödinger equation (2.57). Furthermore, this equation was solved exactly by Zakharov and Shabat [212] by using the inverse-scattering method. These solutions were verified experimentally by Yuen and Lake [199]. In the case of deep water, an envelope soliton consists of a sech-shaped hyperbolic secant envelope which modulates a periodic wave was observed. Likewise,

solitary wave of enveloped was observed in a single fiber [163]. Physically, these optical solitons originate from a simple kind of nonlinearity manifested through the intensity dependence of the refractive index.

2.3.4 Nonlinear enveloped equation in kerr media

Maxwell equations are characterized by accounting for electromagnetic waves. In a vacuum or uniform homogeneous dielectric and linear media, linear waveforms are observed [93]. The previous scenario changes radically when the dielectric medium has a nonlinear response [34, 164]. The propagation of the electric field \vec{E} in a nonlinear dielectric medium is describing by the Maxwell wave equation

$$\frac{1}{c^2} \partial_{tt} \vec{E} + \nabla \times \nabla \times \vec{E} = -\frac{1}{\epsilon_o c^2} \partial_{tt} \vec{P}, \quad (2.66)$$

where \vec{P} accounts for the polarization density of the medium. Unlike a uniform and linear medium, a nonlinear medium, the polarization density, and the electric field satisfy the relationship [27]

$$\vec{P} = \vec{P}_L + \vec{P}_{NL} = \epsilon_o \left(\chi^{(1)} * \vec{E} + \chi^{(2)} |E| * \vec{E} + \chi^{(3)} |E|^2 * \vec{E} + \dots \right), \quad (2.67)$$

Usually, it is assumed that the polarizing process is instantaneous, that is, $\chi^{(1)} * \vec{E} = \chi^{(1)} \vec{E}$. However, the response and organization of the charges is not instantaneous, generating a delayed response for the electric field of the form [133]

$$\chi^{(1)} * \vec{E} = \int_{-\infty}^t \chi^{(1)}(t - \tau) \vec{E}(\tau) d\tau, \quad (2.68)$$

where $\chi^{(1)}(t - \tau)$ is the linear kernel response. In the case of a system that presents instantaneous response, this response function can be modeled by $\chi^{(1)}(t - \tau) = 2\chi_0^{(1)} \delta(t - \tau)$, i.e., $\chi^{(1)} * \vec{E} = \chi_0^{(1)} \vec{E}(t)$. The formula (2.68) can rewrite as

$$\chi^{(1)} * \vec{E} = \int_{-\infty}^t \chi^{(1)}(t - \tau) \vec{E}(\tau) d\tau = \int_0^{\infty} \chi^{(1)}(\tau') \vec{E}(t - \tau') d\tau'. \quad (2.69)$$

Assuming that the kernel is a good function that decays fast enough, one can expand the above expression as follows

$$\chi^{(1)} * \vec{E} = \int_0^{\infty} \chi^{(1)}(\tau') \vec{E}(t - \tau') d\tau' = \chi_0^{(1)} \vec{E}(t) + \dots + \chi_n^{(1)} \frac{d^n \vec{E}(t)}{dt^n} + \dots, \quad (2.70)$$



Figure 2.20: Light propagation in a nonlinear medium, Kerr medium. The left panel shows the propagation of light in a nematic liquid crystal. The right panel realizes the propagation of light in an optical fiber.

where

$$\chi_n^{(1)} = \frac{(-1)^n}{n!} \int_0^\infty \chi^{(1)}(\tau') \tau'^n d\tau'. \quad (2.71)$$

The index of refraction of the linear medium has the form $n = 1 + \chi_0^{(1)}$. The physical system has the time reflection symmetry ($t \rightarrow -t$) then $\chi_{2p}^{(1)} = 0$, $p = 1, 2, \dots$. For the sake of simplicity, it will consider that the nonlinear terms are instantaneous. Hence, nonlinear polarization density reads

$$\vec{P}_{NL} = \epsilon_o \left(\chi^{(2)} |E| \vec{E} + \chi^{(3)} |E|^2 \vec{E} + \dots \right), \quad (2.72)$$

and $\chi^{(n)}$ constant accounts for the n -th nonlinearity. A Kerr medium is called when the first nonlinearity is cubic [121]. In optical fibers, the nonlocal delayed response is provided by the Raman effect [3], which occurs spontaneously when an intense optical beam is passed through a fiber. Figure 2.20 sketches the propagation of light on an optical fiber.

Assuming the hypothesis that the medium has no free charges, then $\nabla \vec{E} = 0$, the wave equation reads

$$\nabla^2 \vec{E} - \frac{1}{c^2} \partial_{tt} \vec{E} = \frac{1}{\epsilon_o c^2} \partial_{tt} \vec{P}. \quad (2.73)$$

finally, considering the dominant terms in the linear response, temporal reflection invariance, and assuming that the medium is of the Kerr type, it is obtained

$$\nabla^2 \vec{E} - \frac{n^2}{c^2} \partial_{tt} \vec{E} = \frac{\chi^{(3)}}{c^2} \frac{\partial^2}{\partial t^2} |E|^2 \vec{E} + \frac{\chi_2^{(1)}}{c^2} \frac{\partial^4}{\partial t^4} \vec{E} \quad (2.74)$$

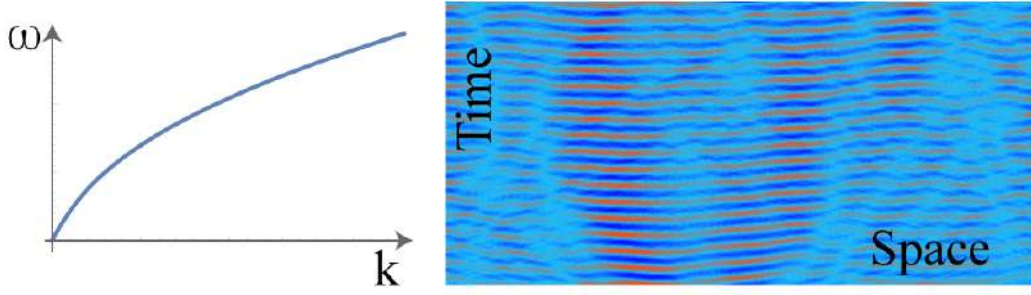


Figure 2.21: Dispersion relationship of the Maxwell wave equation (2.74) with normal dispersion $\chi_2^{(1)} < 0$, formula (2.21), and space-time evolution of waves in the Nonlinear Schrödinger equation.

To figure out the dynamics of linear waves, let us consider the following ansatz $\vec{E} = Ae^{i(kx-\omega t)}\hat{x}$ in equation (2.74), it is obtained the relation dispersion

$$k^2 = \frac{n^2}{c^2}\omega^2 - \frac{\chi_2^{(1)}}{c^2}\omega^4. \quad (2.75)$$

Figure 2.21 shows the relation dispersion. Hence, fiber optics is a dispersive medium as a consequence of the non-instantaneous response of the polarization. To account for nonlinearities, one can consider the limit of weak amplitude and slow spatial and temporal variation, that is,

$$\vec{E} = [A(X, T)e^{i(kx-\omega t)} + \bar{A}(X, T)e^{-i(kx-\omega t)} + W(A, \bar{A}, t, x)]\hat{x}, \quad (2.76)$$

where W is a nonlinear correction ($W \ll A$). Introducing the previous ansatz in the nonlinear Maxwell wave equation (2.74), and assuming the wavenumber and the frequency satisfies the relation dispersion (2.75), at dominate order one get

$$\begin{aligned} \left[\nabla^2 \vec{E} - \frac{n^2}{c^2} \partial_{tt} \vec{E} \right] \cdot \hat{x} &= \left(-k^2 + \frac{n^2 \omega^2}{c^2} \right) Ae^{i(kx-\omega t)} + (2ik\partial_x - 2i\frac{\omega n^2}{c^2} \partial_T) Ae^{i(kx-\omega t)} + \\ &\left(\partial_{xx} + \frac{n^2 \omega^2}{c^2} \partial_{tt} \right) W + c.c. = -\frac{3\chi^{(3)}\omega^2}{c^2} |A|^2 Ae^{i(kx-\omega t)} - \frac{9\chi^{(3)}\omega^2}{c^2} A^3 e^{i3(kx-\omega t)} + \\ &+ \frac{\chi_2^{(1)}\omega^4}{c^2} Ae^{i(kx-\omega t)} + i\frac{\chi_2^{(1)}4\omega^3}{c^2} \partial_T Ae^{i(kx-\omega t)} - \frac{\chi_2^{(1)}6\omega^2}{c^2} \partial_{TT} Ae^{i(kx-\omega t)} + \\ &+ \frac{\chi_2^{(1)}}{c^2} \frac{\partial^4}{\partial t^4} W + c.c. \end{aligned} \quad (2.77)$$

rewriting the above expression

$$\begin{aligned} & \left(\partial_{xx} + \frac{n^2 \omega^2}{c^2} \partial_{tt} - \frac{\chi_2^{(1)}}{c^2} \frac{\partial^4}{\partial t^4} \right) W = \\ & \left(-2ik \partial_x + \left[2i\omega \frac{n^2}{c^2} - i \frac{\chi_2^{(1)} 4\omega^3}{c^2} \right] \partial_T - \frac{3\chi^{(3)} \omega^2}{c^2} |A|^2 - \frac{\chi_2^{(1)} 6\omega^2}{c^2} \partial_{TT} \right) A e^{i(kx - \omega t)} \\ & - \frac{9\chi^{(3)} \omega^2}{c^2} A^3 e^{i3(kx - \omega t)} + c.c. \end{aligned} \quad (2.78)$$

To solve this linear equation, we impose the solubility condition, which sets that all the terms proportional to $e^{i(kx - \omega t)}$ are zero, that is,

$$2i \left(k \partial_x - \left[\omega \frac{n^2}{c^2} - \frac{2\chi_2^{(1)} \omega^3}{c^2} \right] \partial_T \right) A = -\frac{3\chi^{(3)} \omega^2}{c^2} |A|^2 A - \frac{\chi_2^{(1)} 6\omega^2}{c^2} \partial_{TT} A. \quad (2.79)$$

Introducing the co-moving frame coordinate system

$$\zeta = x - \frac{\omega \frac{n^2}{c^2} - \frac{2\omega^3 \chi_2^{(1)}}{c^2}}{k} t, \quad (2.80)$$

$$Z = t. \quad (2.81)$$

the amplitude equation reads (the Nonlinear Schrödinger equation) [3, 111]

$$-2i \partial_\zeta A = \frac{3\chi^{(3)} \omega^2}{c^2} |A|^2 A + \frac{\chi_2^{(1)} 6\omega^2}{c^2} \partial_{TT} A. \quad (2.82)$$

where $\beta_2 \equiv \chi_2^{(1)} 6\omega^2 / c^2$ is the dispersion. When this quantity is negative or positive this coefficient accounts for normal or abnormal dispersion [3, 111]. It is important to note that in the case of abnormal dispersion, the dispersion relationship should be multi-evaluated. The nonlinear term accounts for self-phase modulation.

In the case dispersion is abnormal, and the nonlinearity is positive, the optical fiber can present soliton solutions, see formula (2.65). In optics, these solitons are called bright solitons. It is important to note that these solitons represent the envelope of the wave. That is, the soliton represents a propagative wave that describes a ripple that increases and decreases. Figure 2.22 show a schematic representation of a bright soliton.

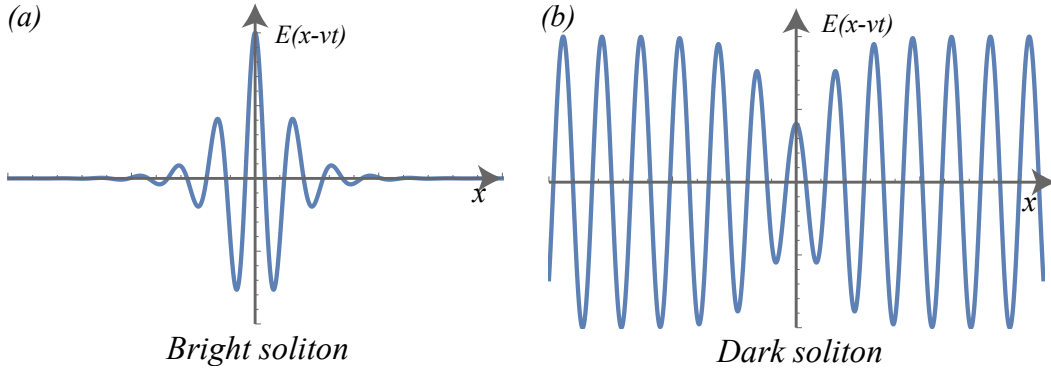


Figure 2.22: Dispersion relationship of the Maxwell wave equation (2.74) with normal dispersion $\chi_2^{(1)} < 0$, formula (2.21), and space-time evolution of waves in the Nonlinear Schrödinger equation.

Dark soliton in NLS

In the case of normal dispersion, the nonlinear Schrödinger equation can be written as follows after normalizing the Z coordinate and magnitude of the amplitude

$$i\partial_\zeta A = -|A|^2 A + \partial_{ZZ} A. \quad (2.83)$$

This equation supports hole-type solutions [124, 206], which has the form

$$A = A_o \sqrt{1 - m^2 \operatorname{sech}^2 \left(\frac{m}{\sqrt{2}} (z - v\zeta) \right)} e^{i\phi}, \quad (2.84)$$

where $\phi = \frac{m}{\sqrt{2}} \left[A_o \sqrt{1 - m^2} (z - v\zeta) + \arctan \left(\frac{m}{\sqrt{1-m^2}} \tanh \left(\frac{mA}{\sqrt{2}} (z - v\zeta) \right) \right) \right] - \frac{(3-m^2)A_o^2 Z}{2}$.

In summary, bright and dark solitons have been observed in optical media, however nonlinear and nonlocal responses and higher-order dispersive effects are critical to understanding the nonlinear wave dynamics observed in optical fibers, non-linear crystals, liquid crystals, and nonlinear optical media in general. Therefore, the generalizations of nonlinear Schrödinger equation that include the nonlinear and nonlocal responses and higher-order dispersive effects are better suited to describe experimental observations [3, 111].

Chapter 3

Dissipative solitons in parametric systems

Macroscopic systems spontaneously transmit energy at their internal degrees of freedom. As a consequence of this process, the dynamics of macroscopic variables are characterized by including dissipative energy processes. The inclusion of this type of process produces the degradation and disparity of the solitons or solitary waves. Figure 3.1 illustrates the degradation of solitons under the presence of a damped effect. To ensure that these solutions do not degrade, it is necessary to inject energy into the system. An efficient way to inject energy into an oscillator is to force it with an external oscillatory force at a frequency close to its natural frequency, a phenomenon known as resonance¹. A similar phenomenon can be achieved by means of the temporal modulation of some physical parameter in a multiple of half of the natural frequency, which can generate linear instabilities of the equilibria under study. This phenomenon is known as parametric resonance [131]. A generalization of resonance phenomenon to a system that is not an oscillator can also be achieved, that is when a system is simply subjected to frequency forcing ω , and it responds to the subharmonic frequency $\omega/2$.

¹Since the dawn of modern physics, this phenomenon was recognized and characterized by one of the founders of modern physics, Galileo Galilei [98].

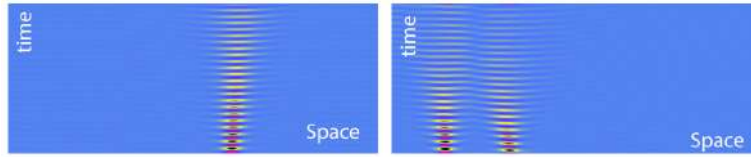


Figure 3.1: Degradation of solitons. Spatiotemporal evolution of numerical simulations of the non-linear Schrödinger equation under the effect of a damping term, imaginary term proportional to the amplitude.

This phenomenon can be understood by means of forcing inducing an oscillator and in turn making it resonate, self-parametric resonance [60]. Then to account for the dynamics exhibited by these systems, it is necessary to take into account the mechanisms of energy dissipation. The balance between dissipation and energy injection will generate attractive behaviors, which are usually called self-organization equilibrium [149].

3.1 Experimental observations of dissipative solitons in parametric systems

When one considers a channel with water, and it oscillates vertically, dissipative solitons are observed for adequate initial conditions and parameters (see Fig. 3.2) [207], in this particular context they are called *non-propagative hydrodynamic solitons*. However, when one considers a container extended in two dimensions with water or other Newtonian fluids, the same type of localized behavior is not observed. In this case, localized propagative solutions are observed (c.f. Fig 3.2b)[140]. The direction of propagation is chosen by a spontaneous break in the symmetry of revolution of the solution. However, if one considers other types of more complex fluids parametrically forced as colloidal fluids [141] or fluidized granular media [198], in two spatial dimensions, one can observe stable localized solutions (cf. Fig. 3.3). These types of solutions are often referred to as *oscillons*. since it corresponds to localized and oscillatory particle type solutions. All these solutions are characterized by being found in the region where the uniform state

3.1. EXPERIMENTAL OBSERVATIONS OF DISSIPATIVE SOLITONS IN PARAMETRIC SYSTEMS

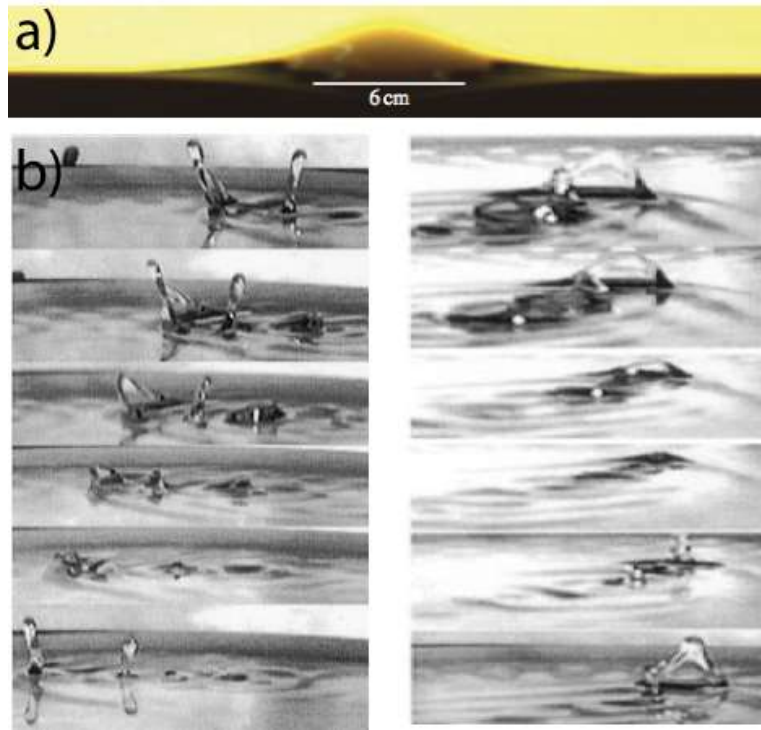


Figure 3.2: Observed parametric dissipative solitons: a) in a vertically driven oscillating water channel [207], these localized structures are stationary. b) Vertically driven vibrated cylindrical container [140], in this case, the localized structures are of propagative nature.

that supports these solutions is stable. Furthermore, this occurs in the parameter region close to where the system presents pattern formation. Then there are two simple ways to observe these solutions: i) perform a localized finite disturbance, which overcomes a nucleation barrier, which originates the localized structure, ii) Inherent fluctuations can excite various spatial modes; in particular, they can excite localized modes, which give rise to localized oscillatory localized solutions, dissipative breathers. iii) be in the parameter region where patterns are observed and move the parameters to the localized structure region. In this last region, the pattern breaks down into a sum of localized structures [53].

From all the examples mentioned above, one can conclude that localized structures or dissipative solitons belong to a universal class of phenomena in parametric systems. To understand this, in the next section, we will analyze a prototype example of a

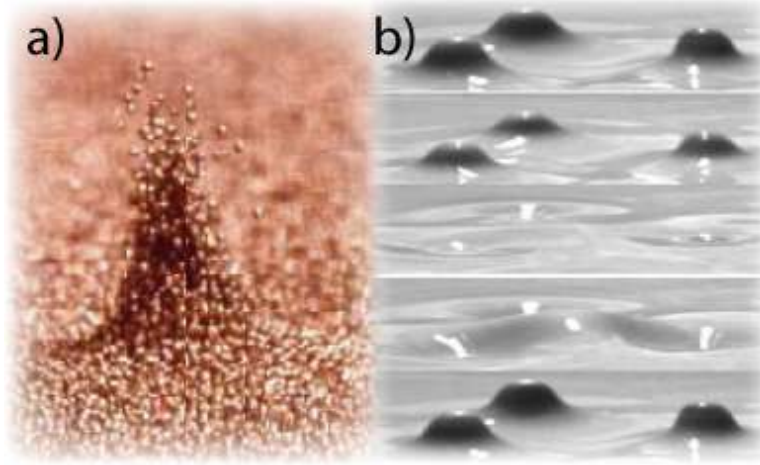


Figure 3.3: Observed parametric dissipative solitons: a) vertically vibrated granular medium, *oscillons* [198]. b) vertically vibrated colloidal fluid [141].

parametric system.

3.2 Parametrically forced pendulum chain

A prototype physical system exhibiting a parametric resonance is a vertically driven, damped, and coupled pendulum chain, illustrated in Fig. 3.4, which is described in the continuous limit by

$$\ddot{\theta}(z, t) = - [\omega_o^2 + \gamma \sin(\omega t)] \sin \theta - \mu \dot{\theta} + \kappa \partial_{zz} \theta, \quad (3.1)$$

where $\theta(z, t)$ accounts for the angle of the pendulum with the vertical at position x at an instant t , ω_o is the natural frequency of the pendulums, which corresponds in the idealized case to $\omega_o = \sqrt{g/l_o}$ with $g = 9.8m/s^2$ and l_o is the pendulum length. γ accounts for the amplitude of the forcing, which is related to the displacement of the vertical bar a , through the relation $\gamma = a\omega^2/l_o$ and ω is the frequency of the forcing. μ accounts for the energy dissipation mechanisms and κ accounts for the elastic coupling between pendulums.

In the limit $\gamma = \nu = 0$, the previous equation corresponds to a Hamiltonian system known in the literature as the sine-Gordon model, which is also temporally reversible,

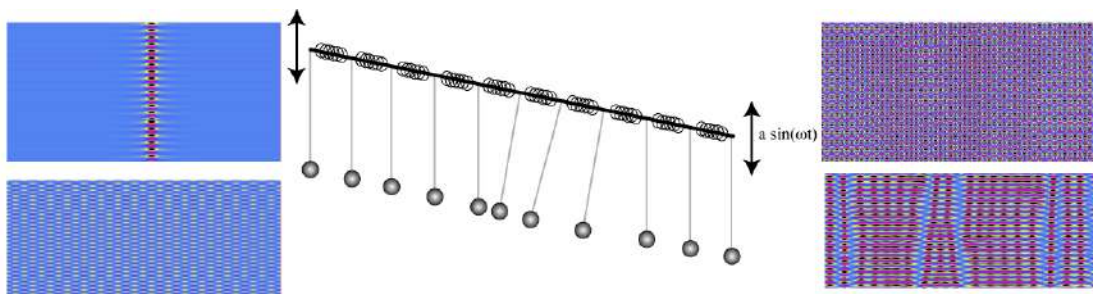


Figure 3.4: Schematic representation of chain of vertically driven coupled pendulums. Insets account for the spatiotemporal evolution of the pendula chain for different parameters. In particular, these insets illustrate localized and extended dissipative structures, spatiotemporal chaos, and intermittency.

when one considers the transformation $t \rightarrow -t$ and $\theta \rightarrow \theta$. A trivial solution of the previous system, equation (4.13), is the upright pendula $\theta(x, t) = 0$, which corresponds to the solution of the pendulums that oscillate simultaneously vertically. If one forces the system to a frequency close to the natural frequency $\omega = 2(\omega + \nu)$, where ν is the mismatch parameter between the frequencies². A linear analysis of the vertical solution shows that this solution is unstable within the region $\nu^2 + \mu^2/4 = \gamma^2/16$ for small detuning and forcing amplitude. This region is usually called the Arnold language [14]. Figure 3.5 illustrates this Arnold language in the parameter space $\{\gamma, \nu\}$. In addition, this figure illustrates some of the dynamic behaviors observed by this system, such as uniform oscillations, dissipative solitons, localized structures, fronts, and kink solutions.

Due to the complex dynamics exhibited by the pendulum chain, one strategy is to study equation (4.13) analytically. However, this equation is from a complex analytical study. A second possibility is to study this equation numerically accompanied simultaneously by simplified equations valid in certain limits. Which will allow us to make approximate analytical calculations.

²This parameter is known as detuning.

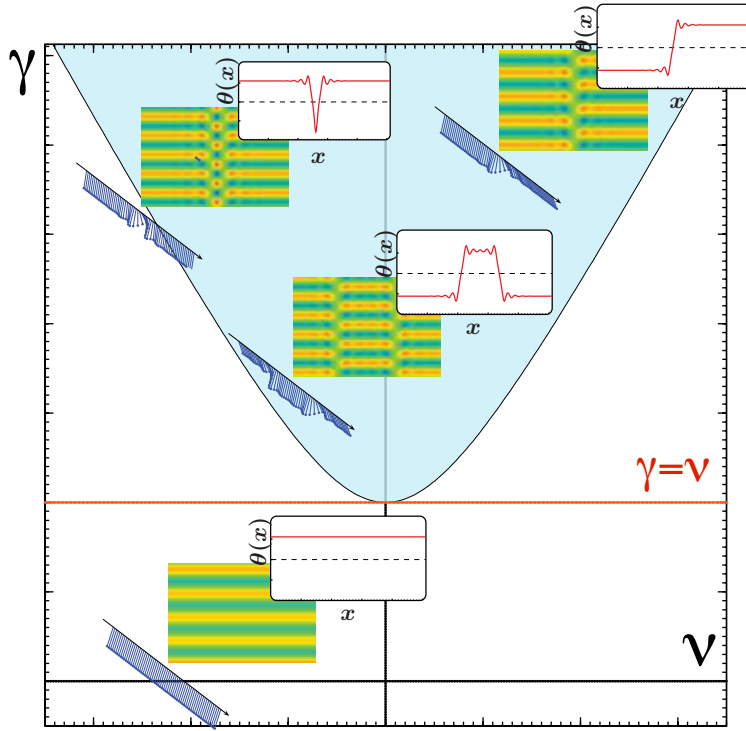


Figure 3.5: Arnold's tongue, bifurcation diagram of the chain of vertically coupled pendulums.

3.2.1 Quasi-reversible limit: parametrically forced nonlinear Schrodinger equation

It is considered the limit where the injection and dissipation of energy are small [45], that is, $\gamma \sim \mu \sim \epsilon \ll 1$ where ϵ is a small scale control parameter. Therefore, we will consider the disturbed Sine-Gordon limit. In addition, for the energy injection to be efficient, one will consider the forcing frequency is close to twice the natural frequency, that is, $\omega = 2(\omega_0 + \nu)$, where ν is the detuning parameter and satisfies $\nu \sim \epsilon$. Then equation (4.13) can be rewritten

$$\ddot{\theta}(z, t) = -\omega_0^2 \sin \theta + \kappa \partial_{zz} \theta - \mu \dot{\theta} + \gamma \sin(2(\omega + \nu)t), \quad (3.2)$$

where the colored terms are perturbative nature of order ϵ . Introducing the following ansatz based on the nonlinear perturbation of the oscillatory field [52].

$$\begin{aligned} \theta(z, t) = & 2\sqrt{\frac{\epsilon}{\omega_o}}A(x, \tau)e^{i(\omega_o+\nu)t} - 2\sqrt{\frac{\epsilon}{\omega_o}}\left\{\frac{A^3(x, \tau)}{48} \right. \\ & \left. + \frac{i\gamma}{16\omega_0^2}A(x, \tau) - \frac{i\gamma\epsilon}{8\omega_0^3}|A(x, \tau)|^2A(x, \tau)\right\}e^{3i(\omega_o+\nu)t} \\ & +c.c. + h.o.t, \end{aligned} \quad (3.3)$$

where $A(x, \tau)$ is the envelope of the uniform vertical oscillation, $\tau \equiv \epsilon t$, and $x \equiv \sqrt{2\epsilon\omega_0/k}z$ are slow variables, that is, they account for the slow variation of this system. Which is a consequence of the separation of scales between the oscillation and the dynamics of the envelope. The symbols *c.c.* and *h.o.t.* account for the complex conjugate and higher corrective terms, respectively.

By introducing the above ansatz into equation (3.2) and after a lot of direct steps one can obtain the following equation for the envelope to the dominant order (this model is known as the *parametrically driven nonlinear Schrödinger equation* [17, 161, 162, 214])

$$\partial_\tau A = -i\nu A - i|A|^2 A - i\partial_x^2 A - \tilde{\mu}A + \tilde{\gamma}\bar{A}, \quad (3.4)$$

where $\tilde{\mu} \equiv \mu/2$, $\tilde{\gamma} \equiv \gamma/4$, and \bar{A} stands for the complex conjugate of the amplitude A . The terms of the previous equation are of order $\epsilon^{3/2}$ and the first corrections are of order $\epsilon^{5/2}$. This model has been used extensively to describe the formation of patterns and localized structures in various physical systems such as: vertically forced water channel [162, 54], spatial structures in non-linear networks [86], parametric optical oscillators [144], magnetic strands forced with an oscillatory field [17, 55], fluidized granular media by means of temporally modulated fluxes [100], to name a few. From the previous examples, we infer that model (3.4) is universal since it accounts for a wide range of physical systems. Therefore, its understanding will allow us to understand various physical systems that share various phenomena. The change of variable (1) corresponds to a transformation of a variable to a periodic coefficient, which transforms the system into a nonlinear equation with coefficients independent of time. Which corresponds to

a nonlinear extension of the Floquet transformation [97, 108]. Through the use of the theory of normal forms this method can be systematized [89].

It is important to mention that the previous equation in the reversible limit, that is, not considering energy injection and dissipation ($\gamma = \mu = 0$), describes the nonlinear Schrödinger equation, which has the form

$$\partial_t A = -i\nu A - i|A|^2 A - i\partial_x^2 A. \quad (3.5)$$

This is a reversible Hamiltonian equation³, and perhaps its most surprising property is that it is integrable, then it exhibits solitons or solitary waves [150], see chapter 2. This classic field equation presents applications in optics, Bose-Einstein condensate, and water waves. A simple interpretation of the above equation is that it accounts for the enveloped dynamics of the chain of coupled nonlinear oscillators.

Dissipative Solitons

The figure (3.6) illustrates the bifurcation diagram of the parametrically driven nonlinear Schrodinger equation (3.4). In which the region where localized solutions exhibited by this model are observed, which accounts for breather solutions of the pendulum chain (4.13), is illustrated. In order to obtain these solutions, one can introduce the following polar representation $A(x, t) = R(x, t)e^{i\theta(x, t)}$, then the equations take the form

$$\partial_t R = 2\partial_x R \partial_x \theta + R \partial_{xx} \theta - \mu R + \gamma R \cos(2\theta), \quad (3.6)$$

$$R \partial_t \theta = -\nu R - R^3 - \partial_{xx} R + R(\partial_x \theta)^2 - \gamma R \sin(2\theta). \quad (3.7)$$

The solution that accounts for the vertical pendulums is $R = 0$ and θ arbitrary. Let us consider the following ansatz $A(x, t) = R(x)e^{i\theta_0}$ [17, 161], that is, the phase is constant and the amplitude is just a function of space. Then

$$0 = -\mu R + \gamma R \cos(2\theta_0), \quad (3.8)$$

$$0 = -\nu R - R^3 - \partial_{xx} R - \gamma R \sin(2\theta_0). \quad (3.9)$$

³Reversibility transformation is $t \rightarrow -t$ and $A \rightarrow -A$.

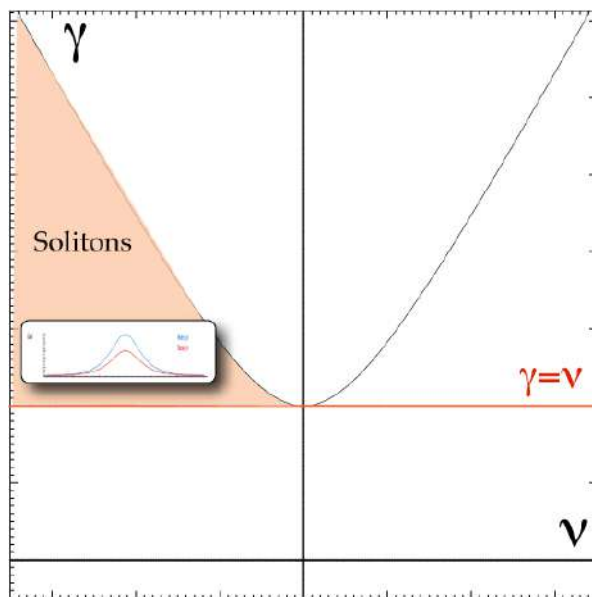


Figure 3.6: Bifurcation diagram of the parametrically driven nonlinear Schrodinger equation. The red line shows the saddle-node fork where these solutions are born. In the Arnold curve, these solutions disappear because the homogeneous support is unstable.

Then one finds that

$$\cos(2\theta_0) = \frac{\mu}{\gamma}. \quad (3.10)$$

The second equation takes the form of a Newton-type equation [see chapter 2 and Eq. (2.62)]

$$\partial_{xx}R = \delta_{\pm}R - R^3. \quad (3.11)$$

where $\delta_{\pm} \equiv -\nu - \gamma \sin(2\theta) = -\nu \pm \sqrt{\gamma^2 - \mu^2}$. The Newton equation has a characterized phase space symmetric with respect to the $\partial_x R$ axis, then it has three equilibrium points $R = 0$ y $R = \sqrt{\delta_{\pm}}$, respectively one is hyperbolic and the others are centers. Since this system is conservative and Hamiltonian. Families of periodic orbits surround centers; their respective separatrices or homoclinic orbits separate these families associated with each center. All this is illustrated in the respective figure of the phase portrait (see figure 3.7). The homoclinic curves correspond to dissipative solitons [73]. To obtain

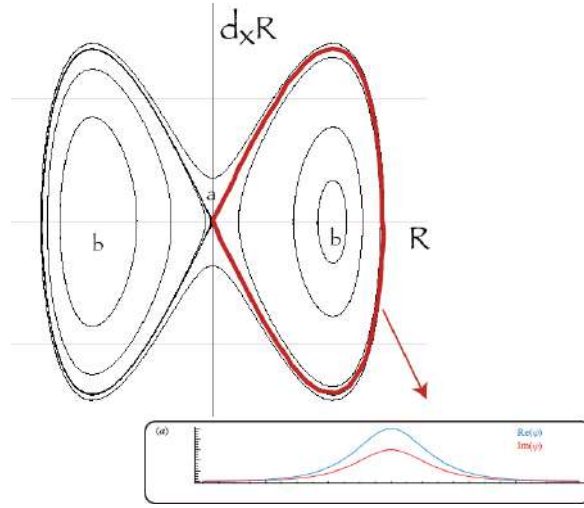


Figure 3.7: Phase portrait of the Newton-type equation 3.11. The points a, b account for the equilibrium points of the system. The red curve represents the homoclinic solution.

these solutions, we integrate Newton type equation

$$E = \frac{(\partial_x R)^2}{2} - \delta_{\pm} \frac{R^2}{2} + \frac{R^4}{4},$$

where E is the respective effective energy associated with the Newton-type equation, considering that the solution asymptotically converges to the zero states. The energy of these homoclinic curves is zero, then we integrate the previous equation and obtain

$$\int \frac{\sqrt{2}dR}{R\sqrt{2\delta_{\pm} - R^2}} = \int dx = x - x_o.$$

Introducing the change of variable $u(x) = 1/R(x)$, then $du = dr/R^2$

$$\int \frac{\sqrt{2}du}{\sqrt{2\delta_{\pm}u^2 - 1}} = x - x_o.$$

Later one considers the change $u(x) = \cosh(\phi(x))/\sqrt{2\delta_{\pm}}$, thereby

$$\int d\phi = \phi = \sqrt{\delta_{\pm}}(x - x_o),$$

taking the hyperbolic cosine of this expression we obtain and dividing by $\sqrt{2\delta_{\pm}}$

$$u = \frac{\cosh \phi}{\sqrt{2\delta_{\pm}}} = \frac{\cosh\left(\sqrt{\delta_{\pm}}(x - x_o)\right)}{\sqrt{2\delta_{\pm}}},$$

finally, the dissipative soliton solution has the form

$$R_{\pm}(x) = \frac{1}{u} = \sqrt{2\delta_{\pm}} \operatorname{sech}\left(\sqrt{\delta_{\pm}}(x - x_o)\right), \quad (3.12)$$

$$\cos(2\theta) = \frac{\mu}{\gamma}, \quad (3.13)$$

The amplitude and the respective width of the soliton are characterized by the parameter δ_{\pm} . On the other hand, the phase of the soliton is fixed by the balance between dissipation and energy injection. El parámetro $\delta_{\pm} = -\nu \pm \sqrt{\gamma^2 - \mu^2}$. Where the curve $\nu^2 = \gamma^2 - \mu^2$, Arnold's language, accounts for the region in the parameter space where the uniform solution of upright oscillating pendulums $\theta = 0$ ($A = 0$) is unstable. We note that the expression δ_{\pm} only real for $\gamma^2 > \mu^2$, that is, when the energy injection exceeds the dissipation, the system exhibits the emergence of localized solutions through a saddle-node bifurcation. Therefore, a pair of finite extended solutions emerge, and for topological reasons, one must be stable and the other unstable. As one continues to increase, for example, the forcing, these solutions become different as one increases in amplitude and decrease in width—which is determined by δ_{+} —and the other inversely decreases in amplitude and increases in width (see figure 3.8), which is determined by δ_{-} . Then when the forcing parameter coincides with Arnold's language δ_{-} it becomes zero, then the dissipative soliton of small amplitude collides with the uniform solution, causing it to become unstable. Notice that this corresponds to the parametric instabil-

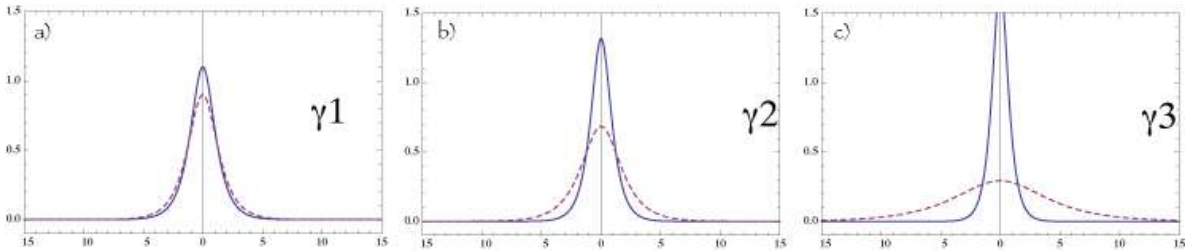


Figure 3.8: Schematic representation of solitons for different forcing amplitudes $\gamma_1 < \gamma_2 < \gamma_3$. The continuous and segmented solution corresponds to δ_{+} (stable) and δ_{-} (unstable), respectively.

ity of the vertical solution. Then by topological consistency, since the vertical uniform solution was stable, then the soliton of small amplitude (δ_-) must be unstable and then the other one with a large amplitude is stable. However, inside Arnold's tongue, the uniform solution that supports the soliton is unstable, so in this region, the soliton is also unstable. The reason for this is that a stable localized solution must be supported in a stable extended state because if it is stable, it must be stable at its asymptomatic ends. In summary, the largest dissipative soliton is stable and arises from saddle-node at $\gamma^2 = \mu^2$ and is unstable on the Arnold tongue curve. The colored region in figure 3.6 illustrates the zone where dissipative solitons are observed.

Another way to understand the mechanism of the appearance of these solutions is by geometrically analyzing the condition that sets the phase $\cos(2\theta) = \mu/\gamma$. Figure 3.9 illustrates the respective intercept of a constant with the trigonometric function in the range $(-\pi, \pi)$. Therefore for small γ , there is no intercept, that is, there are no solutions. Increasing γ until it is equal to μ , then the previous equation has solutions, which

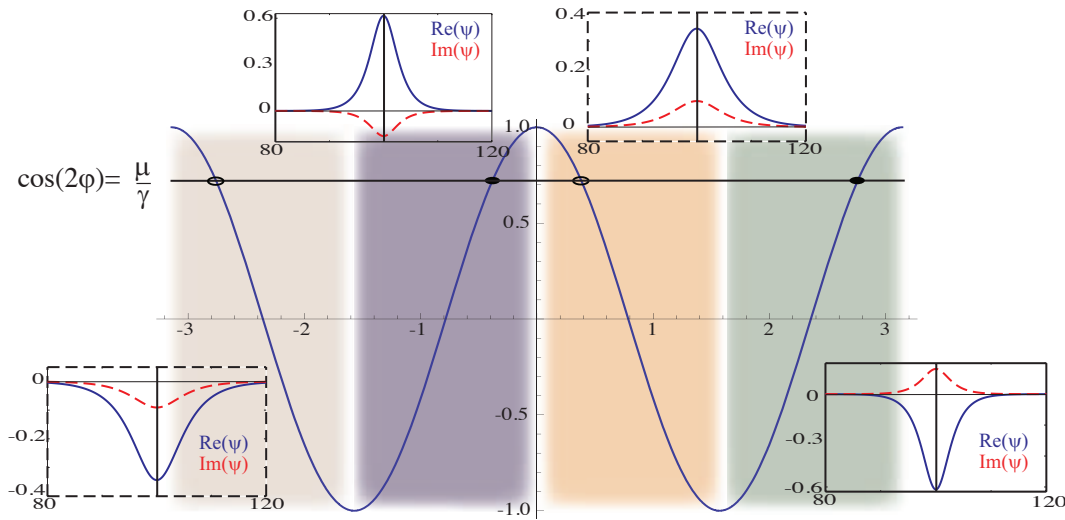


Figure 3.9: Schematic representation of the dissipative soliton emergence mechanism, *saddle-node*. The inserted figures give an account of the solutions in the respective Cartesian representation. Stable and unstable solutions are represented by solid (empty) circles or inset figures with continuous (segmented) frames.

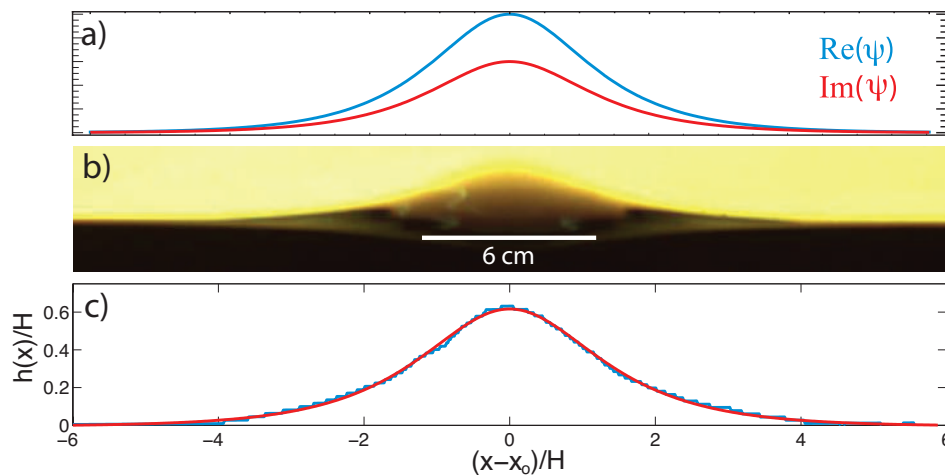


Figure 3.10: Dissipative solitons (a) Stable dissipative soliton observed in the model (3.4). (b) Image of a non-propagative hydrodynamic soliton observed in a 45 cm long and 2.54 cm rectangular container, filled with $H = 1.5$ cm of water and forced vertically. Only two-thirds of the carcass is shown. (c) profile of the instantaneous surface (blue line) with the image shown in (b). The solid red line shows the fit predicted by the solution (3.12).

appear in two pairs as illustrated in Fig. 3.9. The appearance of pairs is a consequence of the reflection symmetry of the parametrically forced non-linear Schrodinger equation ((3.4), that is, the system is invariant before the transformation $A \rightarrow -A$. Therefore the system exhibits both stable and unstable solutions. In Figure 3.9, stable and unstable solutions are represented by solid (empty) circles or inset figures with continuous (segmented) frames.

The previous analysis allows us to conclude that a natural mechanism for the emergence of localized solutions is the emergence of a pair of solutions with complementary stability (stable-unstable), saddle-node. This type of mechanism has been used to explain the emergence of pulses in generic oscillatory media [81].

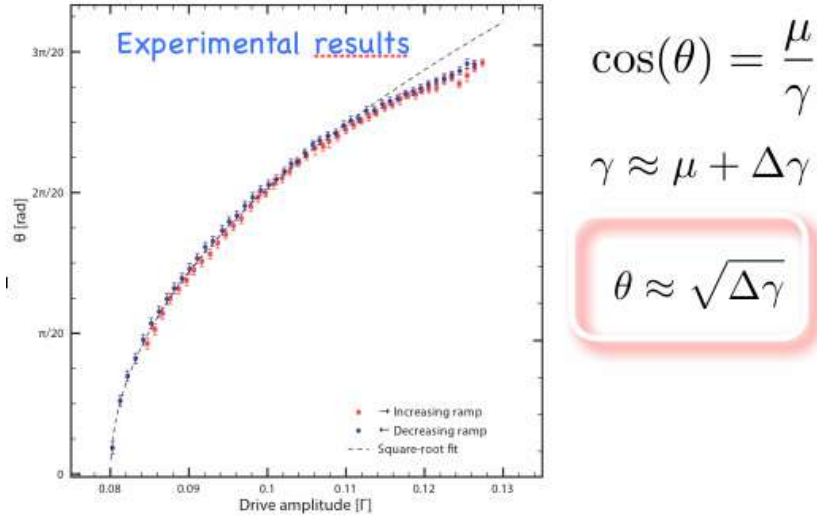


Figure 3.11: Equilibrium phase of the non-propagative soliton as a function of forcing. The points represent experimental data raising and lowering the forcing. The dashed line is obtained using formula (3.15).

Comparison with non-propagative hydrodynamic solitons in a vertically forced fluid

Theoretically, a channel with parametrically forced water is described by the parametrically forced nonlinear Schrodinger equation [162, 205, 104], where the amplitude A accounts for the transverse subharmonic mode for height⁴ and accounts for the potential for the fluid velocity. The amplitude equation with the dimensions of the channel's physical parameters takes the form

$$2i\omega\partial_t A - c^2\partial_{xx}A + (\omega_0^2 - \omega^2)A - a|A|^2A = 0, \quad (3.14)$$

where ω and ω_0 are the frequency of the vertical oscillation and the frequency sloshing motion. The channel dispersion (gravity wave dispersion) has the form $\omega^2 = kg \tanh(kd)$ where g is the gravity, k the wavelength of the mode, and d is the width of the channel. $a \equiv k^4(6T^4 - 5T^2 + 16 - T^{-2})/8$ accounts for the nonlinear self-modulation

⁴If h is the height, then $h = Ae^{\omega t}$ and ϕ is the velocity potential $\phi = Ae^{\omega t/2}$, i.e. $\vec{v} = -\vec{\nabla}\phi$.

where $T = \tanh(kd)$. In figure 3.10 the non-propagative hydrodynamic soliton observed in this system is illustrated and compared with the predicted solution, formula (3.12), which shows a quite fair good agreement.

Another interesting property that one can deduce from the geometric condition is the behavior of the phase as a function of the forcing parameter, in the case that the forcing is of the order of dissipation $\gamma = \mu + \Delta\gamma$, $\Delta\gamma \ll 1$, then

$$\cos(2\theta_0) = \frac{\mu}{\mu + \Delta\gamma} = \frac{1}{1 + \frac{\Delta\gamma}{\mu}} \approx 1 - \frac{\Delta\gamma}{\mu}$$

On the other hand, when the energy injection is of the order of dissipation, the angle is small (see figure 3.10), then θ_0 is small and then the $\cos(2\theta_0) \approx 1 - (2\theta_0)^2/2$, then one finds the relationship between the phase and the forcing increment

$$\theta_0 \approx \sqrt{\frac{\Delta\gamma}{2\mu}}, \quad (3.15)$$

that is, the phase grows with the square root of the forcing shift with respect to the critical point. In Figure 3.10, the above law is verified.

3.3 Effective parametric resonance

The previous analysis used as a *fundamental pillar* of the parametric resonance based on the fact that a system is forced at twice its natural frequency. However, this concept can be generalized as follows: *A system exhibits a parametric resonance when it is subjected to a frequency ω and it responds to a subharmonic frequency of the forcing $n\omega/2$.* This type of phenomenon can occur in any system that does not even have a natural frequency [60].

To emphasize the previous idea, we will follow the method proposed by E. Butikov [37], to analyze the parametric instability of a forced oscillator described by the equation.

$$\ddot{\theta}(t) = - [\omega_o^2 + \gamma \sin(\omega t)] \sin \theta - \mu \dot{\theta}. \quad (3.16)$$

First, we will consider that the angle is small, then the previous equation can be rewritten

$$\ddot{\theta}(t) \approx - [\omega_o^2 + \gamma \sin(\omega t)] \theta - \mu \dot{\theta}. \quad (3.17)$$

Let us consider the following ansatz

$$\theta(t) = \sum_{n=1}^{\infty} C_{2n-1} e^{i\omega t(2n-1)/2} + \bar{C}_{2n-1} e^{-i\omega t(2n-1)/2},$$

where C_n are constants. Introducing the ansatz above in equation (3.17) one finds a hierarchy of equations, where each term is proportional to $e^{i\omega t n/2}$. For simplicity, to first order we will consider the first modes and ignoring the higher modes⁵ which satisfy the equation

$$-\frac{\omega^2}{4} C_1 = - \left(\omega_0^2 + \mu \frac{i\omega}{2} \right) C_1 - i \frac{\gamma}{2} \bar{C}_1, \quad (3.18)$$

$$-\frac{\omega^2}{4} \bar{C}_1 = - \left(\omega_0^2 - \mu \frac{i\omega}{2} \right) \bar{C}_1 + i \frac{\gamma}{2} C_1, \quad (3.19)$$

⁵the galerkin methods [113].

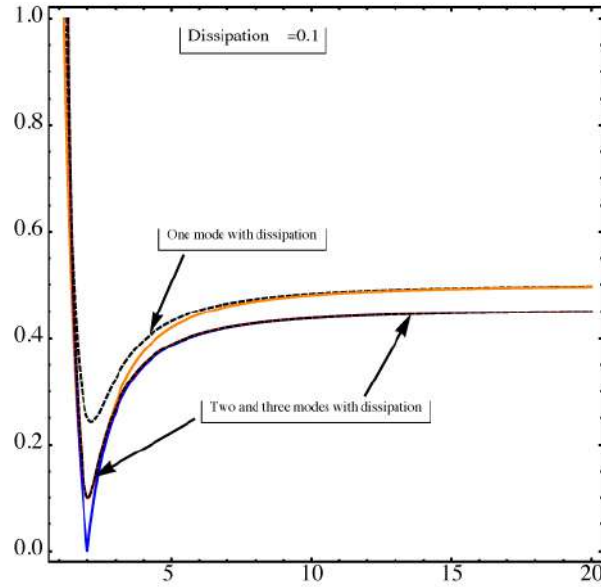


Figure 3.12: Parametric instability curves. the curves are obtained using different numbers of modes.

this expression can be rewritten

$$\begin{bmatrix} \omega_0^2 + \mu \frac{i\omega}{2} - \frac{\omega^2}{4} & i\frac{\gamma}{2} \\ -i\frac{\gamma}{2} & \omega_0^2 - \mu \frac{i\omega}{2} - \frac{\omega^2}{4} \end{bmatrix} \begin{pmatrix} C_1 \\ \bar{C}_1 \end{pmatrix} = 0,$$

this equation has a non-trivial solution if the determinant of the above matrix is zero, then

$$\left(\omega_0^2 - \frac{\omega^2}{4} \right)^2 - \left(\mu \frac{\omega}{2} \right)^2 = \left(\frac{\gamma}{2} \right)^2.$$

Introducing the pendulum displacement in units of pendulum length $\gamma = a\omega^2$, then the above relationship takes the form

$$\left(\frac{\omega_0^2}{\omega^2} - \frac{1}{4} \right)^2 - \left(\frac{\mu}{2\omega} \right)^2 = \left(\frac{a}{2} \right)^2.$$

In Figure 3.12, the black segmented curve illustrates the above formula. The above expression can be improved by considering the other modes. That is, increasing the size of the Galerkin understudy

$$\theta = C_1 e^{i\omega t/2} + \bar{C}_1 e^{-i\omega t/2} + C_3 e^{i3\omega t/2} + \bar{C}_3 e^{-i3\omega t/2},$$

then one gets the set of equations.

$$-\frac{\omega^2}{4} C_1 = -\left(\omega_0^2 + i\frac{\mu\omega}{2} \right) C_1 - i\frac{\gamma}{2} \bar{C}_1 - i\frac{\gamma}{2} C_3, \quad (3.20)$$

$$-\frac{\omega^2}{4} \bar{C}_1 = -\left(\omega_0^2 - i\frac{\mu\omega}{2} \right) \bar{C}_1 + i\frac{\gamma}{2} C_1 + i\frac{\gamma}{2} \bar{C}_3, \quad (3.21)$$

$$-\frac{\omega^2}{4} C_3 = -\left(\omega_0^2 + i\frac{\mu\omega}{2} \right) C_3 - i\frac{\gamma}{2} C_1, \quad (3.22)$$

$$-\frac{\omega^2}{4} \bar{C}_3 = -\left(\omega_0^2 - i\frac{\mu\omega}{2} \right) \bar{C}_3 + i\frac{\gamma}{2} \bar{C}_1. \quad (3.23)$$

Then writing the above expression in matrix form

$$\begin{bmatrix} -\frac{\omega^2}{4} + \left(\omega_0^2 + i\frac{\mu\omega}{2} \right) & i\frac{\gamma}{2} & 0 & 0 \\ -i\frac{\gamma}{2} & -\frac{\omega^2}{4} + \left(\omega_0^2 - i\frac{\mu\omega}{2} \right) & 0 & -i\frac{\gamma}{2} \\ i\frac{\gamma}{2} & 0 & -\frac{\omega^2}{4} + \left(\omega_0^2 + i\frac{\mu\omega}{2} \right) & 0 \\ 0 & -i\frac{\gamma}{2} & 0 & -\frac{\omega^2}{4} + \left(\omega_0^2 - i\frac{\mu\omega}{2} \right) \end{bmatrix} \begin{bmatrix} C_1 \\ \bar{C}_1 \\ C_3 \\ \bar{C}_3 \end{bmatrix} = 0,$$

and by calculating the determinant one can determine the critical relationship. In figure 3.12, this relationship and that also obtained using three modes is illustrated. An interesting if one continues using more modes the curves converge to a common curve. Which has one numerically can be verified and then find a fair good agreement with this approximation based on this method of truncating modes. Therefore, one can study the parametric instabilities away from the resonant condition. Even in the previous method, the system is not required to have a resonant frequency since the curve is well defined.

This method proposed by E. Butikov [37] has the advantage of transforming the time-dependent problem into one or more variables to time-independent coefficients.

In brief, the parametric resonance phenomenon is based on the fact that if a system is subjected to a frequency ω of parametric forcing and it responds to a subharmonic frequency of the forcing $n\omega/2$.

It is important to note that equation (3.17), through the change of variable, can be transformed into the equation

Mathieu Function comments

The equation for small amplitudes of the vertically driven pendulum chain is described by equation (3.17). In general, a linear equation with temporal periodic coefficients is not known how to solve. However, let us see how equation (3.17) was solved through the incorporation of new functions, Mathieu functions [159]. Introducing change the variable $\theta(t) = \psi(t)e^{-\mu t/2}$ and scaling time by $t = 2\tau/\omega$, thus equation (3.17) reads

$$\ddot{\psi}(\tau) = - [\Omega^2 + 2q \sin(2\tau)] \psi, \quad (3.24)$$

where $\Omega^2 \equiv (4\omega_o^2 - \mu^2)/\omega^2$ and $q \equiv \gamma/\omega$. This equation is known as the Mathieu equation [158, 159]. This model were first introduced by Émile Léonard Mathieu, who encountered them while studying vibrating elliptical drumheads [158]. To solve this equation, Mathieu, consider the following strategy, Ω can be written as follows

$$\Omega^2 = m^2 + q\alpha_1 + q^2\alpha_2 + q^3\alpha_3 + \dots, \quad (3.25)$$

where $m = 1, 2, \dots$ is an integer number and α_n are coefficients of expansion. To solve equation (3.24), Mathieu considers the ansatz

$$\psi = ce_n(\tau) \equiv \cos(m\tau) + qc_1(\tau) + q^2c_2(\tau) + q^3c_3(\tau) + \dots, \quad (3.26)$$

$$\psi = se_n(\tau) \equiv \sin(m\tau) + qs_1(\tau) + q^2s_2(\tau) + q^3s_3(\tau) + \dots, \quad (3.27)$$

with $c_n(\tau)$ and $s_n(\tau)$ are periodic functions. By replacing the previous Ansatz in equation (3.24), after imposing solvability conditions, one obtains a hierarchy of equations in q that do not explicitly depend on time. To explain how the method works, let us consider the ansatz (3.26) in equation (3.24), $m = 1$, and the first terms in the hierarchy, we get

$$\cos(\tau) = \cos(\tau), \quad (3.28)$$

$$\ddot{c}_1 + c_1 + \cos(3\tau) + (\alpha_1 - 1)\cos(\tau) = 0. \quad (3.29)$$

To solve the latter equation, we impose $\alpha_1 = 1$ and obtain $c_1(\tau) = \cos(3\tau)/8$. All other equations and unknowns are solved using this method. Therefore, this method allows systematically obtaining this type of solution of Eq. (3.24) [158, 159]. From these Mathieu functions, the bounded and divergent region of these functions can be

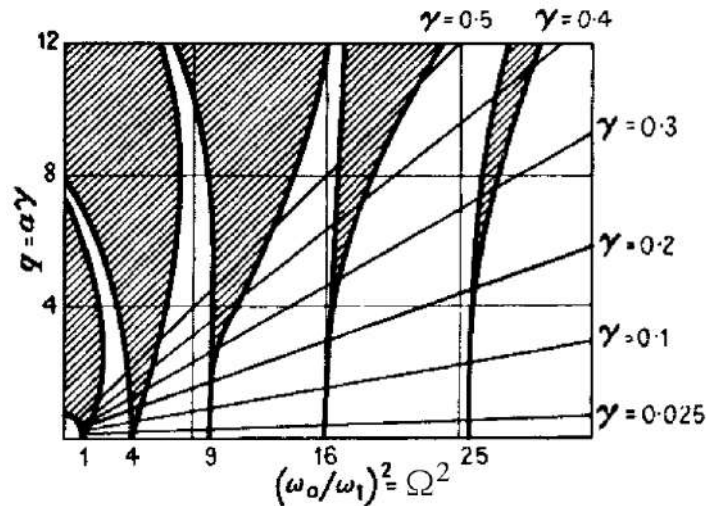


Figure 3.13: Stability chart for frequency modulation in the parameter space Ω and q obtaining used Mathieu function [159].

determined. Figure 3.13 illustrates these divergent regions by hatched areas. These regions are usually called Arnold's tongues.

Effective-parametric resonance in a non-oscillating system: self-parametric resonance

The parametric resonance is an instability of a dissipative oscillatory system where one or more parameters are modulated in time or space, injecting energy into the system. As one of the control parameters of the system overcomes a certain threshold, a coherent oscillatory response develops with an amplitude that depends on the the nonlinear saturation of the instability. The oscillation frequency is given by a resonance condition relating injection and dissipation of energy with the mismatch between forcing and natural frequencies. It must be noticed that the idea of energy storing and transferring due to resonances can be even generalized to fluctuating systems [99].

We present a phenomenon arising from parametric amplification with compromising potential applications: the generation of *self-parametric resonance* which induces oscillations in a non-oscillating system, that is, a system that without parametric forcing cannot present permanent oscillations. As we have mention, the parametric instabilities have been explained by the introduction of Mathieu functions. However, from such complex analysis no intuition can be drawn nor new insights can be given on how to extend it in other physical contexts. We study the self-parametric resonance in a simple prototype model that allows us to build a description based on a forced system with an effective potential and apply these results to a parametrically amplified over-damped pendulum. In this simple system, we show theoretically, numerically, and experimentally the appearance of sustained oscillations with a given frequency and amplitude, controlled externally by the parametric forcing.

To characterize the self-parametric resonance phenomenon, let us consider the following simple prototypical dynamical system

$$\ddot{x} = -\gamma \sin(\omega t)x - \mu\dot{x} - \alpha x^3, \quad (3.30)$$

where $x(t)$ is a variable that describes the state of system, the \dot{x} its time derivative, μ is a viscous damping parameter accounting for energy dissipation, α characterizes the nonlinear response of the system, and γ and ω are, respectively, the intensity and frequency of the external parametric forcing. Other models can be chosen to describe the emergence of permanent oscillations by self-parametric resonance, however Eq. (3.30) possesses the main ingredients necessary to describe this phenomenon.

To study the phenomenology of self-parametric resonance, we have performed numerical simulations of model Eq.(3.30) using a fourth order Runge-Kutta algorithm with time step $\Delta t = 0.02$ for several values of the control parameters. In the non-dissipative limit ($\mu = 0$) for $\alpha > 0$, model (3.30) exhibits chaotic behavior near the origin and quasi-periodic behavior away from it when ω is of order 1, as illustrated in Figure 3.14a. However, as ω increases sufficiently, the former scenario changes and the phase portrait described before is changed to the equivalent phase portrait of a simple oscillator, i.e. chaotic behavior is transformed into a harmonic behavior (cf. Fig. 3.14b). In the dissipative regime ($\mu > 0$), the dynamics of the system is characterized by the appearance of a chaotic attractor [114], as depicted in Fig. 3.14c. As ω increases sufficiently, the phase portrait displays the equivalent of a damped oscillator, as illustrated in Fig. 3.14d. Even, the effect of large ω can even stabilize a non-oscillating system with divergent trajectories ($\alpha < 0$) with or without dissipation. Fig. 3.14e shows the phase portrait of Model (1) for small ω displaying divergent trajectories. As ω increases, there is a qualitative change in the trajectories as oscillations develop around the fixed point $x = \dot{x} = 0$ and trajectories do not diverge, as it is shown in Fig. 3.14f. Therefore, for large ω and γ of order 1, Model (3.30) shows the emergence of oscillations.

Forced systems with explicit temporal dependence, as the one displayed in model (3.30), are usually studied in terms of first return maps using the time-dependent forcing period as the iteration period between two successive values of the map [167]. This approach will be of benefit in the case of low frequency forcing, where the dominant time scale is the forcing scale. In the case of high frequency forcing, first return maps describe basically the same dynamics as Model (3.30). Furthermore, first return maps,

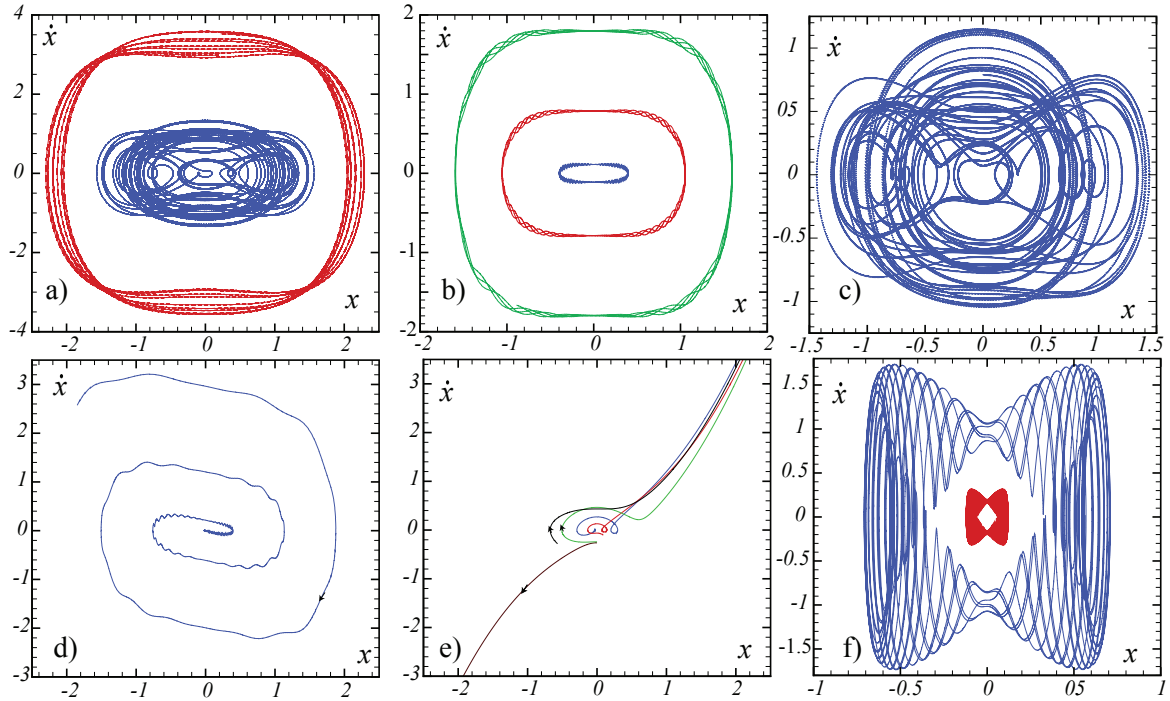


Figure 3.14: (color online) Phase portrait of Model (3.30) for a) $\alpha = 1.0$, $\gamma = 1.0$, $\mu = 0$ and $\omega = 0.5$, b) $\alpha = 1.0$, $\gamma = 1.0$, $\mu = 0$ and $\omega = 20.0$, c) $\alpha = 1.0$, $\gamma = 1.0$, $\mu = 0.02$ and $\omega = 0.5$, d) $\alpha = 1.0$, $\gamma = 0.3$, $\mu = 0.2$ and $\omega = 10.0$, e) $\alpha = -2.0$, $\gamma = 46.5$, $\mu = 0.0$ and $\omega = 1.0$, f) $\alpha = -2.0$, $\gamma = 46.5$, $\mu = 0.0$ and $\omega = 20.0$. Figure obtained from [60].

although useful for calculations of stability of fixed points, and hence limit cycles, do not give insight to the physical mechanism for the generation of the high frequency dynamics explained above. Another way to study the high frequency dynamics of Eq. (3.30) that can present a way to interpret and understand the dynamics is the strategy proposed by Kapitza [118]: the previous high frequency dynamics can be understood as a result caused by the separation of time scales between the forcing and the state variable $x(t)$ itself, which can be explained the appearance of an effective force. Unlike the linear analysis based on Mathieu functions, this strategy allows a global description that contains the nonlinear response of the system. Therefore, a generalization of this type of strategy may allow us to glimpse into non-trivial phenomena arising from the original forced system. Rigorous methods based on high frequency averaging, which justify the strategy proposed by Kapitza, was developed by Bogoliubov [28]. Following

the strategy proposed by Kapitza, the dynamics is decomposed as ($\omega \gg \mu$)

$$x(t) = z(t) + \frac{\gamma}{\omega^2} \sin(\omega t) z(t), \quad (3.31)$$

where $z(t)$ accounts for the slow dynamics and the second term on the right-hand side stands for the small and fast dynamics [28, 118]. Introducing the above Ansatz in Eq. (3.30), we obtain

$$\begin{aligned} \ddot{z} &= -\frac{\gamma^2}{2\omega^2} z - \mu \dot{z} - \frac{2\gamma}{\omega} \cos(\omega t) \dot{z} - \frac{\gamma}{\omega^2} \sin(\omega t) \ddot{z} \\ &+ \frac{\gamma^2}{2\omega^2} \cos(2\omega t) z - \frac{\mu\gamma}{\omega} \cos(\omega t) z - \frac{\mu\gamma}{\omega^2} \sin(\omega t) \dot{z} \\ &- \alpha z^3 \left[1 + \frac{\gamma}{\omega^2} \sin(\omega t) \right]^3. \end{aligned} \quad (3.32)$$

If one considers the limit, $\omega \gg 1$ and $\gamma/\omega^2 \ll 1$ and averaging in a period $2\pi/\omega$, we obtain (high frequency averaging dynamics)

$$\ddot{z} = -\gamma^2/2\omega^2 z - \alpha z^3 - \mu \dot{z}.$$

On the other hand, in the case of small z and considering that $\gamma/\omega^2 < 1$ but not small, the dominant order of Eq. (3.32) takes the form

$$\ddot{z} = -\frac{\gamma^2}{2\omega^2} z - \alpha z^3 - \mu \dot{z} - \frac{2\gamma}{\omega} \cos(\omega t) \dot{z}, \quad (3.33)$$

up to leading order resonant terms in γ/ω . In this effective dynamical system $z(t)$ is a variable that accounts for slow dynamics of $x(t)$. Hence, the slow dynamics corresponds to an oscillator with an induced natural frequency $\omega_I \equiv \gamma/\sqrt{2}\omega$. In the limit of high frequencies ($\gamma \ll \omega^2$), the last term is neglected as a result of the separation of scales between $z(t)$ and the forcing, which corresponds to Kapitza analysis [131]. Thus, using this approach, the first term of the right hand side is an effective force that leads the dynamics. Independently if at moderate frequencies model Eq. (3.30) has divergent trajectories ($\alpha > 0$) or not ($\alpha < 0$), in the above limit the system can be described as an oscillator. Model (3.33) allows us to intuitively understand the dynamics exhibited by model Eq. (3.30) in this limit providing a way to understand the emergence of oscillations in non-oscillating systems submitted to high frequency forcing. In brief, the

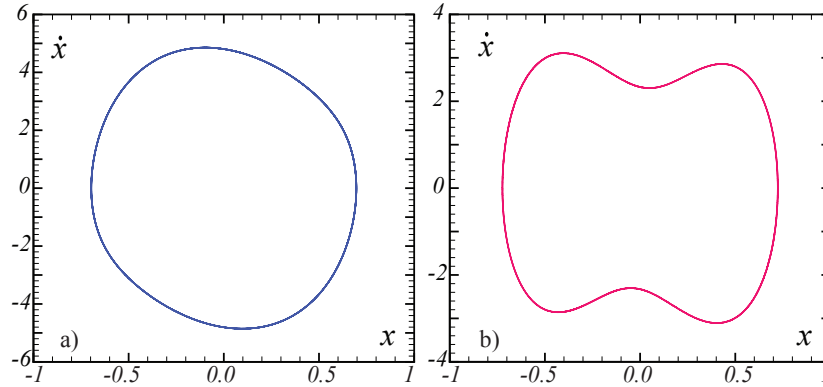


Figure 3.15: Phase portrait of prototype model (3.30) for $\alpha = 200.0$, $\gamma = 48.0$, $\mu = 1.0$ and $\omega = 14.0$ (a) and $\alpha = -1.0$, $\gamma = 47.0$, $\mu = 1.0$ and $\omega = 10.0$ (b). Figure obtained from [60]

non-oscillator system subjected to a high frequencies forcing (Eq. 3.30) is equivalent to a parametrically driven oscillator with a well defined natural frequency ($\gamma^2/2\omega^2$). Therefore, one expects intuitively that changing the value of the induced natural frequency one can observe the well-known characteristics of parametric resonance.

For large but fixed ω , as we increase γ , the induced natural frequency increases. Furthermore, the terms neglected in the strategy of Kapitza grow in their amplitudes. The combination of these effects can generate the phenomenon of *effective-parametric resonance*: as ω_I approaches $\omega/2$ and the forcing and dissipative terms can be balanced, the system can resonate by parametrically amplifying itself. Hence, by modifying γ appropriately, the system can display this phenomenon when $\gamma \sim \sqrt{2}\omega^2/2$. Therefore, $x = \dot{x} = 0$ becomes unstable and nonlinearity saturates this instability leading to attractive periodic solutions. Figs. 3.15a and 3.15b show the stable limit cycle generated by effective-parametric resonance for both positive and negative α . Thus, for large ω and γ which satisfy the above resonance condition, Model (3.30) induces simultaneously a natural frequency of oscillation and a parametric forcing, giving rise to effective-parametric resonance at half the forcing frequency even for large dissipation. From these simulations, we can infer that in the case of positive (negative) α , the observed limit cycle is dominated by the first dominant mode (first two dominant modes). This explains the different limit cycles in the $x - \dot{x}$ phase portrait displayed in Fig. 3.15.

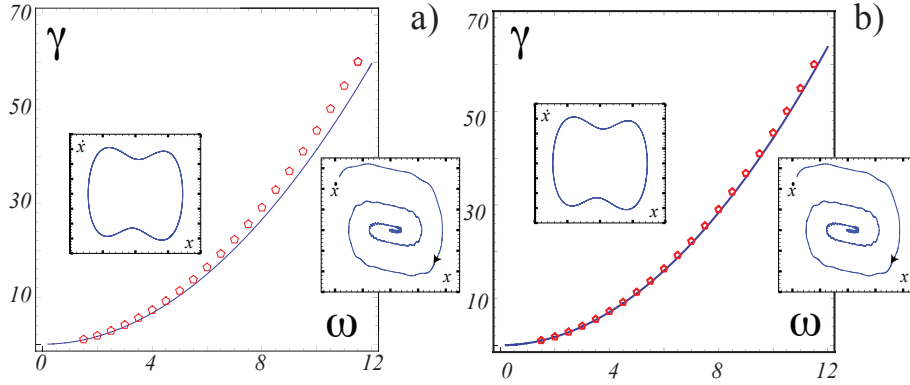


Figure 3.16: Effective-parametric resonance curve in $\gamma - \omega$ space for $\mu = 0.1$ and $\alpha = -1.0$. Above the dotted line, the system shows effective-parametric resonance. Pentagon symbols are obtained by numerical simulation of Model (3.30). The solid line in a) and b) are, respectively, deduced from Model (3.33) and (3.32). Left insets: Limit cycle. Right insets: Damped oscillations towards $x = 0$.

Performing a modal expansion–Galerkin expansion [113]–for Eq.(3.33) and, keeping the dominant terms of modal expansion up to order γ/ω , one finds the curve

$$(\gamma/2\omega)^2 = (\mu/2)^2 + (\omega/2 - \gamma/\omega\sqrt{2})^2 \quad (3.34)$$

for the stability of $x = 0$. To corroborate this prediction we have performed numerical simulations of model (3.30) in the $\omega - \gamma$ space, showing good agreement with the predicted curve. Figure 3.16a shows both theoretical and numerical results. On the other hand, using the same modal expansion in Eq. (3.32) allow us compute an amended instability curve, which improves the accuracy to within 3 % from the previous expression as it is shown in Fig. 3.16b, although the qualitative shape of the curve is remains the same. Thus, our first order approximation agrees consistently with numerical simulations of the instability curve. Above the curve a stable limit cycle in the $x - \dot{x}$ phase portrait develops (Fig. 3.16, left inset) whereas outside of it damped oscillations towards $x = \dot{x} = 0$ appear (Fig. 3.16, right inset). In the case of $\alpha < 0$, for small (large) μ compared with ω , effective-parametric resonance develops as a super(sub)-critical instability, that is, when one increases γ the system shows the appearance of a infinitesimal (finite) limit cycle. In the other case ($\alpha > 0$), one observes the opposite

behavior.

Effective parametric resonance in an upside-down vertically driven pendulum

As we have noted before, effective parametric resonance results from the effect the parametric amplification of a system by a large amplitude and high frequency forcing. A simple mechanical system that shows this effect is a vertically driven pendulum. The upside-down state becomes stable at high frequencies even for small displacement amplitudes of the support point, as a result of the emergence of an oscillator where the upside-down position is a stable fixed point [131]. This counter-intuitive fact was first predicted analytically in the pioneering work of Stephenson [191] which spanned a large amount of theoretical [131] and experimental discussions [96, 116, 160, 188] of the phenomenon. As the displacement amplitude is increased, it was observed numerically [26] and experimentally [188] the appearance of a nonlinearly saturated oscillation around the upside-down position. This is a limit cycle in the $\phi - \dot{\phi}$ phase portrait, where ϕ is the angle of the pendulum with respect to the vertical axis and $\dot{\phi}$ is the angular velocity. This phenomenon was associated with a Hopf bifurcation [26], which is related to a time-independent linear operator. This statement is inadequate for the upside-down position because the linear stability analysis of this state is related to a periodic time-dependent linear operator which requires the use of Floquet theory [108]. On the other hand, this behavior can be inferred as a consequence of the linear analysis based on Mathieu functions. Alternatively, using a weakly nonlinear analysis, one finds that the dynamics around the upside-down state is similar to Model (3.30) with negative α . Therefore, the appearance of permanent oscillations with respect to the vertical state is the result of effective parametric resonance. It is important to note that in the study of the Faraday instability for strong viscous fluid a similar resonant condition is established in Ref. [40].

Experimental observation of the self-parametric resonance: a parametrically excited pendulum is built to explore effective parametric resonance. A stainless steel

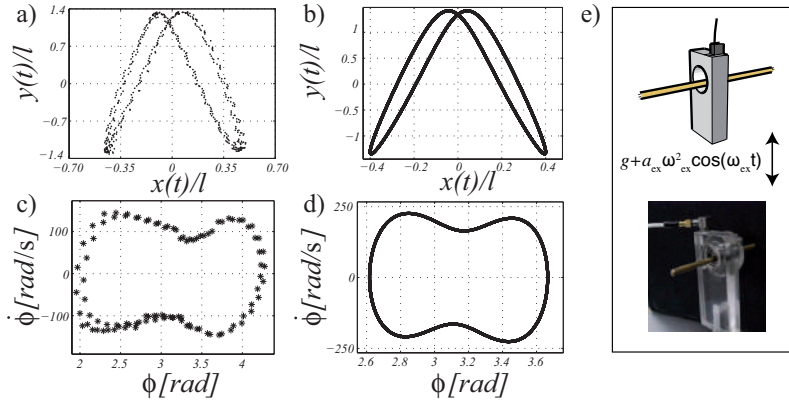


Figure 3.17: Lisajous figure of the nonlinear oscillations around the inverted pendulum position is obtained experimentally (a) and numerically (b). Limit cycle oscillating around the inverted position of a physical pendulum is found experimentally (c) and numerically (d). (e) Schematic representation and snapshot of the physical pendulum under consideration.

cylindrical roller bearing (internal diameter 8 mm, external diameter 15 mm) is mounted vertically into a plexiglass plate ($10 \times 15 \times 4 \text{ mm}^3$), see Fig. 3.17. A plexiglass cylinder is fixed solidary to a cylindrical roller bearing, which enables it to rotate smoothly in a plane. A massive bronze bar (length 60 mm, diameter 3 mm) is eccentrically positioned 2 mm from the center of the cylinder (cf. Fig. 3.17), displacing the center of mass from the center of the plexiglass cylinder. This asymmetry generates a physical pendulum with a natural frequency $f_0 \approx 10 \text{ Hz}$ ($\omega_0 \approx 30 \text{ rad/s}$) and oscillating radius $l \approx 2 \text{ mm}$. The whole system is then mounted over an electromechanical shaker driven sinusoidally by a frequency generator via a power amplifier. The modulation of the acceleration of gravity $a_{ex}\omega_{ex}^2 \cos(\omega_{ex}t)$ with $\omega_{ex} = 2\pi f_{ex}$ is measured directly by a piezoelectric accelerometer and a charge amplifier. The control parameters are then ω_{ex} and a_{ex} ($\gamma_{ex} = a_{ex}\omega_{ex}^2/l$). The motion of the pendulum is acquired with a high-speed camera at 500 fps in a 800×600 pixel window.

We explore the large frequency limit $\omega_{ex}/\omega_0 \gg 1$ in the particular case of $a_{ex}/l \sim 1$, which corresponds $\gamma_{ex} \sim \omega_{ex}^2$. For a given ω_{ex} , increasing the amplitude of modulation a_{ex} the inverted pendulum is stabilized. As a_{ex} continues to increase, new equilibria appear, namely a limit cycle, which oscillates at $f_{ex}/2$ around the inverted position

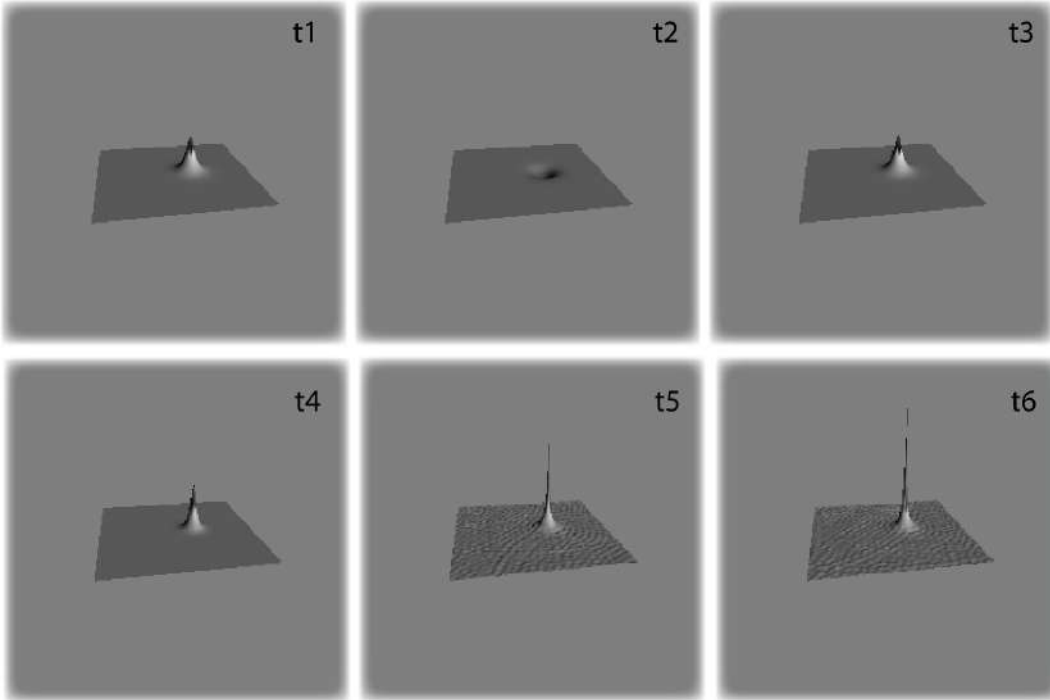


Figure 3.18: A blow-up of a soliton solution of the nonlinear Schrödinger equation in two-dimensions (3.35) with $\gamma = \mu = 0$. Snapshots of the real part of the amplitude for an evolution time sequence, $t_1 < t_2 < t_3 < t_4 < t_5 < t_6$.

$\phi = \pi$. This type of limit cycle also appears oscillating around $\phi = 0$. These oscillations cannot occur in the unforced system, due to its highly dissipative nature. Figure 3.17a shows a typical trajectory of the center of mass of the pendulum found experimentally for $\omega_{ex}/\omega_0 \approx 5$ and $a_{ex}/l \approx 2$, and in Fig. 3.17b the numerically computed trajectory. They display Lissajous figures on the phase portrait with two frequencies, one being f_{ex} and the other one being $f_{ex}/2$. We also show in Fig. 3.17c and 3.17d the phase portrait. Notice that the limit cycle is surrounding the inverted position $\phi = \pi$.

3.3.1 Dissipative solitons in two dimensions

In integrable conservative systems such as Korteweg de Vries, the nonlinear Schrödinger, and the Boussinesq equation, solitons are observed in one-dimensional systems (see Chapter 2). In two dimensions, these localized solutions are unstable, presenting a

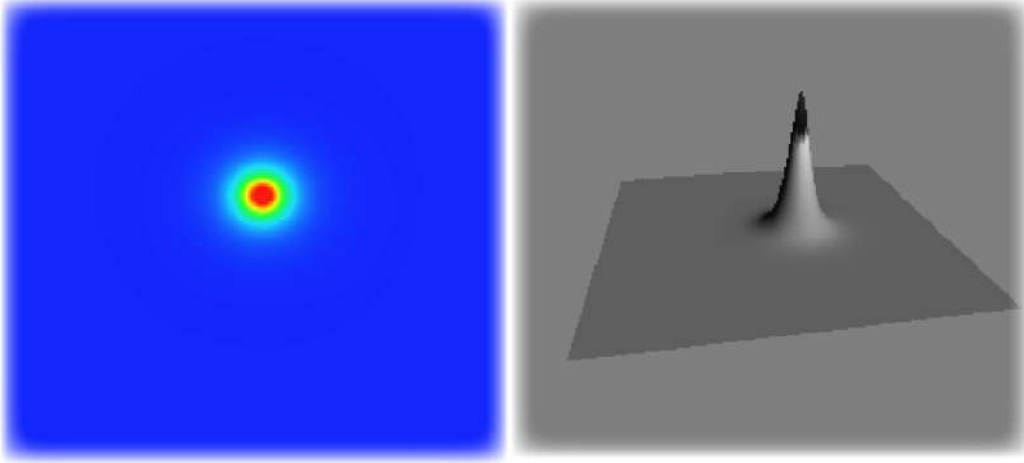


Figure 3.19: Dissipative structure of obtain from numerical simulation of parametrically drive nonlinear Schrödinger equation in two-dimensions (3.35).

singularity in finite time or *blow-up* [150]. Figure 3.18 shows the typical phase singularity obtained in the nonlinear Schrödinger equation in two dimensions. The injection and dissipation of energy can stabilize the explosion of localized structures. In driven systems, we experimentally observe stable localized structures (see Figs. 1.3 and 3.3). Let us consider the parametrically driven damped nonlinear Schrödinger equation in two-dimensions

$$\partial_t \psi = -i\nu\psi - i|\psi|^2\psi - i\nabla_{\perp}^2\psi - \mu\psi + \gamma\bar{\psi}. \quad (3.35)$$

It is well-known that Eq.(3.35) exhibits stable non propagative dissipative solitons in two spatial dimensions [20]. Figure 3.19 The localized states have the form $\psi = \pm R_s(r = |\vec{r}|)e^{i\theta_0}$, where $\cos(2\theta_0) = \mu/\gamma$, and R_s satisfies

$$\partial_{rr}R_s + \partial_r R_s/r - \lambda R_s + R_s^3 = 0, \quad (3.36)$$

where $\lambda \equiv -\nu + \sqrt{\gamma^2 - \mu^2} > 0$. To our knowledge, it does not exist analytical solution of the localized state. However the asymptotic behaviors of this solution are well defined, for instance $R(r \rightarrow \infty) \rightarrow e^{-\sqrt{\lambda}r}/\sqrt{r}$. Furthermore, using the variational method, one can also obtain a good approximation by [4]

$$R_s(r) = A_0 \sqrt{\lambda} \operatorname{sech} \left(B_0 \sqrt{\frac{\lambda}{2}} r \right), \quad (3.37)$$

where $A_0 = 2.166$ and $B_0 = 1.32$. From the approximated localized state (3.37), one can infer that for negative detuning, this solution appears by a saddle-node bifurcation when dissipation and energy injection are equal ($\gamma = \mu$ and $\nu < 0$). Furthermore, this solution is unstable when the uniform state $\psi = 0$ —which supports this localized state—becomes unstable at the Arnold’s tongue ($\gamma^2 = \nu^2 + \mu^2$, by $\nu < 0$). The characteristic size and amplitude of the localized precession states respectively are $1/\sqrt{\lambda}$ and $\sqrt{\lambda}$.

3.4 Interaction of parametric solitons

As we have already shown, dissipative solitons are solutions that have an identity in their shape (cf. expression 3.12) and are characterized by a position which corresponds to the maximum of their amplitude (see figures 3.8 and 3.10). Furthermore, as we have already mentioned, there are two types of solitons in phases and out of phase. Therefore, the natural question that arises is if these types of solutions can interact and if they interact, what is the law of interaction. Qualitative studies of the interaction between non-propagative hydrodynamic solitons have been reported in the literature [203, 204]. Motivated by the previous question, we have recently carried out a systematic and quantitative experimental study of the interaction of non-propagative hydrodynamic solitons in a narrow channel with water [54, 181]. Figure 3.20 shows a pair of solitons interacting in phase and in out of phase. To grasp the dynamics exhibited by this system, we will consider the interaction of a couple of dissipative solitons.

3.4.1 Interaction of a pair of solitons

To account for the interaction, we will consider the polar representation of the parametrically forced nonlinear Schrodinger equation, equations (3.6) and (3.7), we will introduce the following ansatz that describes two solitons interacting respectively

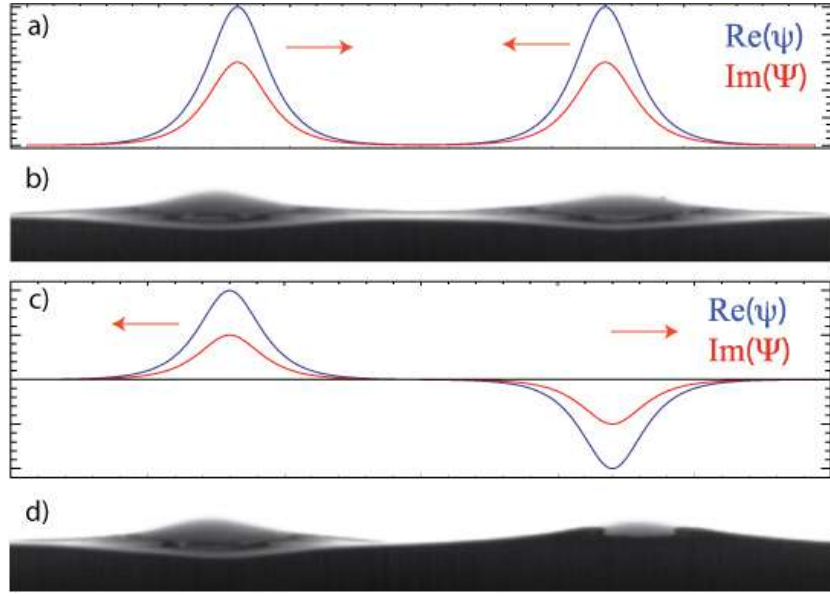


Figure 3.20: Interaction of non-propagative hydrodynamic solitons a), b) in-phase and c), d) in out-of-phase. Complex field profile ψ and snapshots obtained from a vertically vibrated channel [54].

in the positions $\Delta/2$ and $-\Delta/2$

$$R(x, t) = R_+ \left(x + \frac{\Delta(t)}{2} \right) + \chi R_+ \left(x - \frac{\Delta(t)}{2} \right) + \rho(x, \Delta), \quad (3.38)$$

$$\theta(x, t) = \theta_0 + \varphi(x, \Delta), \quad (3.39)$$

where R_+ accounts for the modulus of the stable soliton which is defined in expression (3.12) and $\Delta(t)$ accounts for the distance between solitons. To adequately account for the interaction, the position of the solitons has been promoted to a function of time. As a consequence of the equations being nonlinear, when the solitons are sufficiently separated ($\Delta \gg 1$), the modulus and phase are corrected by small functions $\rho(x, \Delta)$ and $\varphi(x, \Delta)$ ($\rho, \varphi \ll 1$). The parameter χ shows whether the solitons are in phase ($\chi = 1$) or in out-of-phase ($\chi = -1$). In the limit that the solitons are quite far apart (dilute solitons), one exponentially affects the other by means of its tail that decays asymptotically to zero. Then, one expects $\Delta(t)$ to be in this limit a slowly temporary

variable, that is, $\ddot{\Delta} \ll \dot{\Delta} \ll 1$.

For the sake of simplicity, we introduce the notation

$$R_{+,+}(z_+) = R_+(z_+ \equiv x + \Delta/2), \quad (3.40)$$

$$R_{+,-}(z_-) = R_+(z_- \equiv x - \Delta/2), \quad (3.41)$$

$$W = (R_{+,+} + \chi R_{+,-}), \quad (3.42)$$

where z_+ and z_- are the coordinates in the respective mobile systems. Introducing the ansatz of a pair of solitons [equations (3.38) and (3.39)] in equation (3.6) and linearizing in ρ and φ , we obtain after some straightforward calculations

$$\frac{\dot{\Delta}}{2} (\partial_{z_+} R_{+,+} - \chi \partial_{z_-} R_{+,-}) = W \partial_{xx} \varphi + 2 \partial_x W \partial_x \varphi - 2 \sqrt{\gamma^2 - \mu^2} W \varphi.$$

This equation does not depend on ρ , furthermore, this equation can be integrated by means of the integration factor W and integrating twice one obtains the following recursive relationship

$$\varphi = \int_{-\infty}^x dx' \frac{\sqrt{\gamma^2 - \mu^2}}{W^2} \int_{-\infty}^{x'} dy W^2 \varphi(y, t) + \int_{-\infty}^x \frac{dx' \dot{\Delta}}{2W^2} \int_{-\infty}^{x'} dy W (\partial_{z_+} R_{+,+} - \chi \partial_{z_-} R_{+,-}). \quad (3.43)$$

To solve the previous equation we will consider the limit of the saddle-node bifurcation where the solitons ($\gamma - \mu \ll 1$) are born, that is, the first term on the right side is small. Then in this limit, we can use the Born approximation, and then we obtain

$$\varphi = \dot{\Delta} \Theta(x, \Delta) + O(\sqrt{\gamma - \mu}), \quad (3.44)$$

with

$$\Theta(x, \Delta) \equiv \int_{-\infty}^x \frac{dx'}{2W^2} \int_{-\infty}^{x'} dy W (\partial_{z_+} R_{+,+} - \chi \partial_{z_-} R_{+,-}),$$

and $O(\sqrt{\gamma - \mu})$ accounts for corrections. Therefore, the phase corrections to the dominant order at this limit are of the order of the temporal variations of the distance between solitons. Then we have managed to obtain a suitable approximation of the phase.

For the module, analogously, we can introduce Ansatz (3.38) in equation (3.7) and linearizing for ρ and φ , we obtain

$$W\partial_t\varphi = \mathcal{L}\rho - 2\mu W\varphi - 3\chi R_{+,+}^2 R_{+,-} - 3R_{+,-} R_{+,+}^2 \quad (3.45)$$

with

$$\mathcal{L} \equiv -\nu + \sqrt{\gamma^2 - \mu^2} - 3(R_{+,+} + \chi R_{+,-})^2 - \partial_{xx}. \quad (3.46)$$

Using the approximation for phase (3.44) and neglected the high derivative in Δ , the above equation takes the form

$$\begin{aligned} \mathcal{L}\rho &= -2\mu W(x)\Theta(x)\dot{\Delta} - 3\chi R_{+,+}^2(x)R_{+,-}(x) \\ &\quad - 3R_{+,-}(x)R_{+,+}^2(x). \end{aligned} \quad (3.47)$$

Since this is a linear equation, to impose that there is a solution, we introduce the following scalar product in the Hilbert functional space

$$\langle f|g \rangle = \int_{-\infty}^{\infty} f(x)g(x) dx,$$

The linear operator \mathcal{L} is self-adjoint ($\mathcal{L} = \mathcal{L}^\dagger$). The kernel of this operator—set of functions $\{v\}$ that satisfies $\mathcal{L}v = 0$ —is of dimension 2. Since $\mathcal{L}\partial_x R_{+,+} \approx 0$ is exponentially small ($e^{-\delta_+^{1/2}\Delta}$), the $R_{+,+}$ functions are pseudo eigenvectors of the kernel of \mathcal{L} . Therefore, the field ρ has a solution if it is fulfilled (solubility condition)

$$\langle \partial_{z_+} R_{+,+} | 2\mu W\Theta \rangle \dot{\Delta} + \langle \partial_{z_+} R_{+,+} | 3\chi R_{+,+}^2 R_{+,-} \rangle + \langle \partial_{z_+} R_{+,+} | 3R_{+,+} R_{+,-}^2 \rangle = 0.$$

An equivalent result we get if we use the other kernel element $\partial_{z_+} R_{+,-}$, for $\partial_{z_+} R_{+,+}$. Since $\partial_{z_+} R_{+,+}$ is a function of order one near the position of the soliton $R_{+,+}$ and that it decays exponentially near the position of the soliton $R_{+,-}$, then the last term in the above equation is negligible compared to the second, that is,

$$\dot{\Delta} = -\frac{3\chi \langle \partial_{z_+} R_{+,+} | R_{+,+}^2 R_{+,-} \rangle}{2\mu \langle \partial_{z_+} R_{+,+} | W\Theta \rangle}, \quad (3.48)$$

where

$$\langle \partial_{z+} R_{+,+} | W\Theta \rangle = \int_{-\infty}^{\infty} dz \partial_z R_{+,+} W(z) \int_{-\infty}^x \frac{dx'}{2W^2(x')} \int_{-\infty}^{x'} dy W(y) \Lambda(y), \quad (3.49)$$

is a positive number by symmetry arguments, $\Lambda(y) \equiv \partial_{z+} R_{+,+}(y) - \chi \partial_{z-} R_{+,-}(y)$, and

$$\langle \partial_{z+} R_{+,+} | R_{+,+}^2 R_{+,-} \rangle = \int_{-\infty}^{\infty} dz \partial_z R_{+,+}(z) R_{+,+}^2(z) R_{+,-}(z + \Delta). \quad (3.50)$$

To estimate the previous integral, we evaluate it near the position of the soliton $R_{+,+}$, where $R_{+,-}(z + \Delta) \approx \sqrt{2\delta_+} e^{-\delta_+(z+\Delta)}$ and then

$$\langle \partial_{z+} R_{+,+} | R_{+,+}^2 R_{+,-} \rangle \approx \sqrt{2\delta_+} e^{-\delta_+\Delta} \int_{-\infty}^{\infty} dz \partial_z R_{+,+}(z) R_{+,+}^2(z) e^{-\delta_+z}. \quad (3.51)$$

Finally, we obtain the law of interaction of a pair of solitons

$$\dot{\Delta} \approx -\mathcal{R} \chi e^{-\delta_+\Delta}, \quad (3.52)$$

where

$$\mathcal{R} = \frac{3\sqrt{2\delta_+} \int_{-\infty}^{\infty} dz \partial_z R_{+,+}(z) R_{+,+}^2(z) e^{-\delta_+z}}{\mu \int_{-\infty}^{\infty} dz \partial_z R_{+,+} W(z) \int_{-\infty}^x \frac{dx'}{2W^2(x')} \int_{-\infty}^{x'} dy W(y) \Lambda(y)},$$

is a positive constant. Therefore, the interaction between two dissipative solitons for a parametrically forced medium is characterized by an exponential interaction as a function of the distance between solitons. This interaction is attractive (repulsive) when the solitons are in phase (anti-phase), that is, for $\chi = 1$ ($\chi = -1$).

Given the simplicity of the dynamics that describe the interaction between solitons, if one considers an arbitrary initial condition, we can integrate the above equation and find

$$\Delta(t) = \delta_+^{-1} \ln[-\chi \delta_+ \mathcal{R}(t - t_0)], \quad (3.53)$$

Where t_0 is determined by the initial condition

$$t_0 = \chi \frac{e^{\delta_+\Delta(t=0)}}{\delta_+ \mathcal{R}}$$

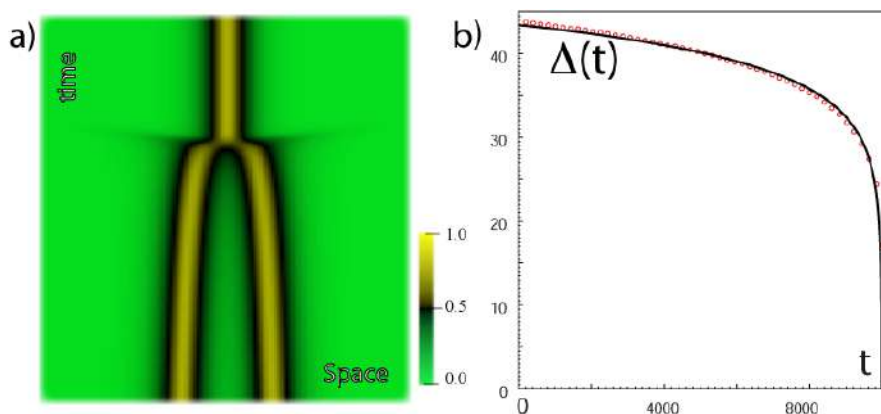


Figure 3.21: Interaction of dissipative solitons in the parametrically forced non-linear Schrödinger equation (3.4). a) Space-time diagram of the module $R(x,t)$. b) Temporal evolution of the distance between the solitons $\Delta(t)$.

Therefore, two dissipative solitons that are in phase (anti-phase) are characterized by a logarithmic decrease (increase) in the soliton separation distance. Figure 3.21 shows the temporal evolution of the distance between solitons for two dissipative solitons in phase. The red points show the position of the solitons obtained numerically and the continuous curve is obtained from formula (refE-Delta). It is important to note that this expression shows an adequate agreement, even for small distances where the calculation loses validity. In the case ($\chi = 1$) the previous expression is only valid $t \leq \tau \equiv -1/\delta_+ \mathcal{R} + t_0$, where τ accounts for the collapse time, that is, the instant in which both solitons merge. Numerically, one observes after the collapse between the solitons only one soliton survives. Furthermore, this fusion process is accompanied by radiation in both directions, see figure 3.21. A similar process is observed in the function of two solitons in Hamiltonian non-integral systems [85]. In this context, the self-similar soliton fusion process has been developed based on a statistical theory based on entropic arguments [179]. It is important to note that the described interaction process only takes into account when the solitons are distant and then the fusion process is not described. In the case that the solitons are in anti-phase ($\chi = -1$), the law of interaction of a pair of solitons is valid for $t > t_0$, where the parameter t_0 is related to

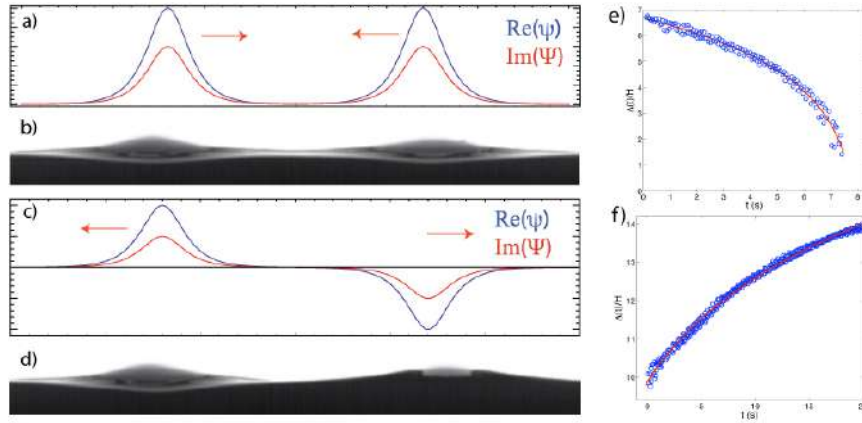


Figure 3.22: Interaction of non-propagative hydrodynamic solitons in a vertically forced water channel. Instant image of solitons in phase $\{a, b\}$ and in anti-phase $\{c, d\}$, c) evolution of the distance of the solitons as a function of time. The blue circles are values ??obtained experimentally and the red curve is through the use of formula (3.66).

the initial condition.

In Reference [54], we have experimentally verified the law of interaction pairwise, equation (3.52), in the case of considering two solitons in phase or masks. The results show an adequate agreement, which emphasizes that one dissipative soliton exponentially affects the other.

3.5 Interaction pair law of localized states in two-dimensions

As we showed in section 3.4.1, there are localized structures in two-dimensions. In this section, we will characterize the interactions of these localized structures. We consider two localized states sufficiently separated, i.e. the distance between them is greater than the characteristic size of localized states. Hence, we can introduce the following Ansatz $\psi(r, t) = R(r, t)e^{i\theta(r, t)}$,

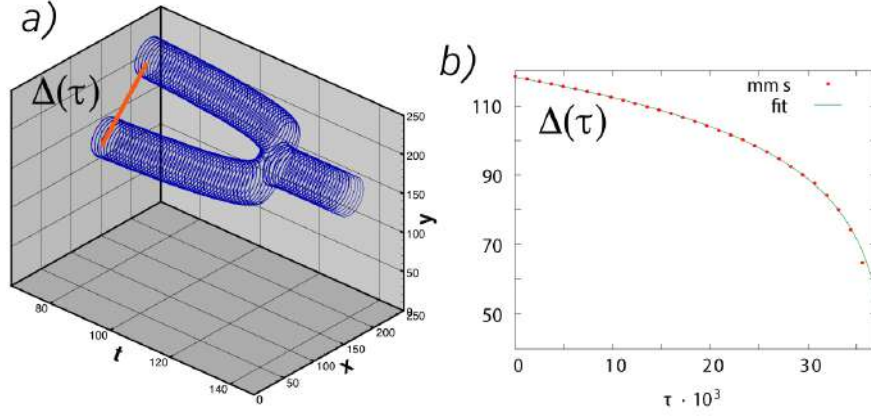


Figure 3.23: Interaction of localized states in the parametrically driven damped nonlinear Schrödinger equation. a) Spatiotemporal diagram of interaction of a pair of localized states obtained from model Eq. (3.35). The circles represent the core of the localized states, i.e. the isolines of the full width at half maximum of the localized state, counterplot chart. $\Delta(\tau)$ accounts for the distance between localized states at given time τ . Temporal evolution of the separation distance $\Delta(\tau)$.

$$\begin{aligned} R &= R_s^+ \left(r + \frac{\Delta(t)}{2} \hat{r} \right) + \chi R_s^- \left(r - \frac{\Delta}{2} \hat{r} \right) + \rho(\vec{r}, \Delta), \\ \theta &= \theta_0 + \varphi(\vec{r}, \Delta), \end{aligned} \quad (3.54)$$

where R_s^\pm are non propagative dissipative solitons, $\Delta(t)$ stand for the distance between the localized states ($\Delta \gg \sqrt{\lambda}$), \hat{r} is the unit vector in the direction between localized states, $\chi = \pm 1$ is a sign that accounts if the solutions are in- or out of phase, $\rho(\vec{r}, \Delta)$ and $\varphi(\vec{r}, \Delta)$ are respectively the corrections functions. The coordinate system is chosen at the centroid between the two located structures. Defining $W \equiv R_s^+ + \chi R_s^-$, considering the parameter region where the dissipation and injection of energy are similar ($0 < \gamma - \mu \ll 1$), introducing the above Ansatz into Eq. (3.4) and linearizing in correction functions we obtain

$$W \partial_t W = \vec{\nabla}_\perp \left(W^2 \vec{\nabla}_\perp \varphi \right), \quad (3.55)$$

$$W \partial_t \varphi = \mathcal{L} \rho - 2\mu \varphi - 3\chi R_s^+ R_s^- W, \quad (3.56)$$

To solve the above equations we need to derive φ . However finding a global solution

of φ remains a difficult task. Nevertheless, if localized states are diluted we can find φ around the center of each dissipative soliton. In order to get φ , we changed our reference system by $\vec{r}' = \vec{r} + \hat{r}\Delta/2$, and in consequence, approximating the functions $W(r' = |\vec{r}'|) \approx R_s^+(r')$ and $\partial_t W \approx \dot{\Delta} \partial_{r'} R_s^+/2$. Next, using the approximation (3.37) and integrating Eq.(3.55), after straightforward calculations we find out

$$\varphi(r') = -\frac{\dot{\Delta}}{4} \left(r' - \frac{1}{2B} \text{Shi}(2Br') \right) \equiv \dot{\Delta} \Theta(r'), \quad (3.57)$$

where $\text{Shi}(2Br')$ is the hyperbolic sine integral.

Replacing expression (3.57) into Eq. (3.56), we find a linear equation in ρ . To solve this linear equation we use the Fredholm alternative [95]. Therefore we introduce the following inner product $\langle f|g \rangle = \iint fg \, dx dy$, where \mathcal{L} is self-adjoint and its kernel is characterized by $\{\partial_{r'} R_s^\pm\}$. To determine the interaction it is essential to know the asymptomatic behavior of the localized solution. R_s satisfied the equation

$$\partial_{rr} R_s + \partial_r R_s / r - \lambda R_s + R_s^3 = 0, \quad (3.58)$$

where $\lambda \equiv -\nu + \sqrt{\gamma^2 - \mu^2} > 0$. To our knowledge, it does not exist analytical solution of the localized state. However the asymptotic behaviors of this solution are well defined, for instance

$$R(r \rightarrow \infty) \rightarrow e^{-\sqrt{\lambda}r} / \sqrt{r}. \quad (3.59)$$

Then applying this product to Eq. (3.56), we find the following solvability condition (*pair interaction law*)

$$\begin{aligned} \dot{\Delta} &= -\chi \frac{3}{a\mu} \int_0^{r'} \partial_{r'} R_s^- (R_s^-)^2 R_s^+ (\hat{\mathbf{r}}' - \Delta \hat{\mathbf{x}}) r' dr' d\theta \\ &\approx -\chi \frac{b}{a\mu} \frac{e^{-\sqrt{\lambda}\Delta}}{\sqrt{\Delta}}, \end{aligned} \quad (3.60)$$

where $a = \langle \partial_{r'} R_s^- | \Theta \rangle$ and $b \equiv 3A \int_0^{r'} \partial_{r'} R_s^- (R_s^-)^2 - e^{-\sqrt{\lambda}r \cos \theta} dr'$. The pair interaction law is derived using the asymptotic behavior of the localized state. Hence, the localized precession states experience a exponential force of attraction ($\chi = 1$) or repulsion ($\chi = -1$) if they are in- or out of phase. In the limit of diluted localized states the

prefactor $1/\sqrt{\Delta}$ is a correction of the dominant term which is exponential. However, when these states are located closer to this prefactor becomes more relevant.

Hence the interaction of precession localized states is like over-damped two-dimensional particles with two types of charges where the interaction is only radial. Figure 3.23 compares the evolution of the distance between the localized states obtained using the pair interaction law and compared to those obtained from the numerical simulations of the parametrically driven damped nonlinear Schrödinger equation. We find a remarkable agreement.

In the case of reversible two-dimensional systems, using Lagrangian methods one can derive a similar interaction law, however the radial dynamics can be enhanced by the appearance of tangential forces [190, 107].

3.5.1 Interaction far from the appearance of localized structures.

To characterize the interaction between localized structures, we have considered the approximation that the forcing strength is of the order of dissipation, $\gamma - \mu \ll 1$. Then in this so-called Born approximation, the phase is proportional to the rate of temporal variation of the phase. $\varphi \sim \dot{\Delta}\Theta(x, \Delta)$ (cf. formula 3.43). Corrections can strongly modify the interaction. Experimentally it is observed that for forcing strength small but greater than dissipation, dissipative solitons in phase attract and annihilate, resulting in a new soliton [54, 204]. The interaction law—formula (3.52)—describes the attraction process; however, it does not represent the collision of dissipative localized structures. Experimentally it is observed when increasing the value of the intensity of the forcing different regimes. The terms considered in the temporal variation of the phase must be included $O(\ddot{\Delta}, \dot{\Delta}^2)$. Note that in this regime, In particular, a bouncing movement is observed between the localized structures. Further when increasing the intensity of the forcing the bounced state is replaced by a bounded state. Figure 3.24 summarizes the type of dynamics observed experimentally and numerically. The amplitude equation

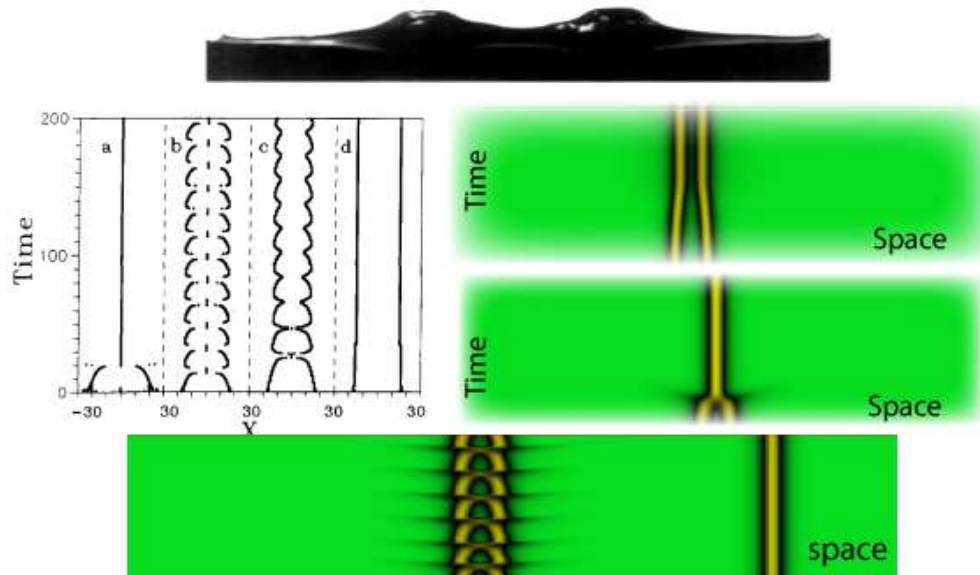


Figure 3.24: Interaction of localized structures far from the appearance of localized states. The left panel account for the experimental results obtained in Ref. [204]. The panel on the right accounts for the numerical results simulated by the parametrically driven nonlinear Schrödinger equation.

does not wholly describe the complete description of the observed dynamics but rather qualitatively describes the observed dynamics.

3.5.2 Self-similar dynamics of a soliton gas

In the parameter space inside Arnold's language, one observes periodic solutions. From these solutions, if one moves to the region of solitons then these solutions are transformed into a gas of solitons that begin to interact. The time evolution of a soliton gas is illustrated in Figure 3.25. Due to the interaction, the solitons merge in pairs, therefore, as time evolves, the remaining solitons separate from each other each time (see figure 3.25). Then, if the system were infinite, the evolution of the system would be static, since we would permanently be in the state of a gas of interacting solitons that move away, where the only sensation would be that the temporal evolution would be slower and slower. Due to the process described above, the interaction of distant

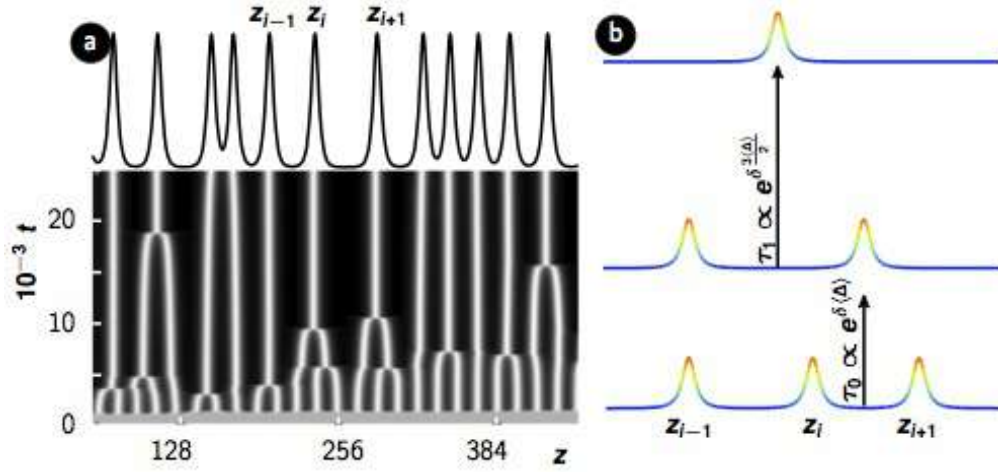


Figure 3.25: Dinámica de interacción de gas de solitones. a) Siulación numérica de la ecuación de Schrodinger no-lineal forzada parametricaménte. b) Representación esquemática de la interacción de solitones disipativos.

solitons is negligible, since these are exponentially suppressed by neighboring solitons. Then the interaction of n -solitons is given by

$$\dot{z}_i = \sum_{j=1} (-1)^j \mathcal{R} e^{-\delta(z_i - z_{i-j})} + \mathcal{R} e^{-\delta(z_{i+j} - z_i)}, \quad (3.61)$$

where z_i is the position of the i -th soliton. Then the interaction with first neighbors is given by

$$\dot{z}_i = -\mathcal{R} e^{-\delta(z_i - z_{i-1})} + \mathcal{R} e^{-\delta(z_{i+1} - z_i)}. \quad (3.62)$$

This equation is self-similar if we consider the following transformation of dilation in the coordinates and in time

$$z_{i+1} - z_{i-1} \rightarrow z_{i+1} - z_{i-1} + \langle \Delta \rangle_0, \quad (3.63)$$

$$t \rightarrow t e^{3\delta \langle \Delta \rangle_0 / 2}. \quad (3.64)$$

Namely, if we separate the dissipative solitons, the dynamics displayed will simulate that given by the dissipative solitons without separating, but the time scale will be exponentially smaller. The factor will depend on the separation distance. Then one

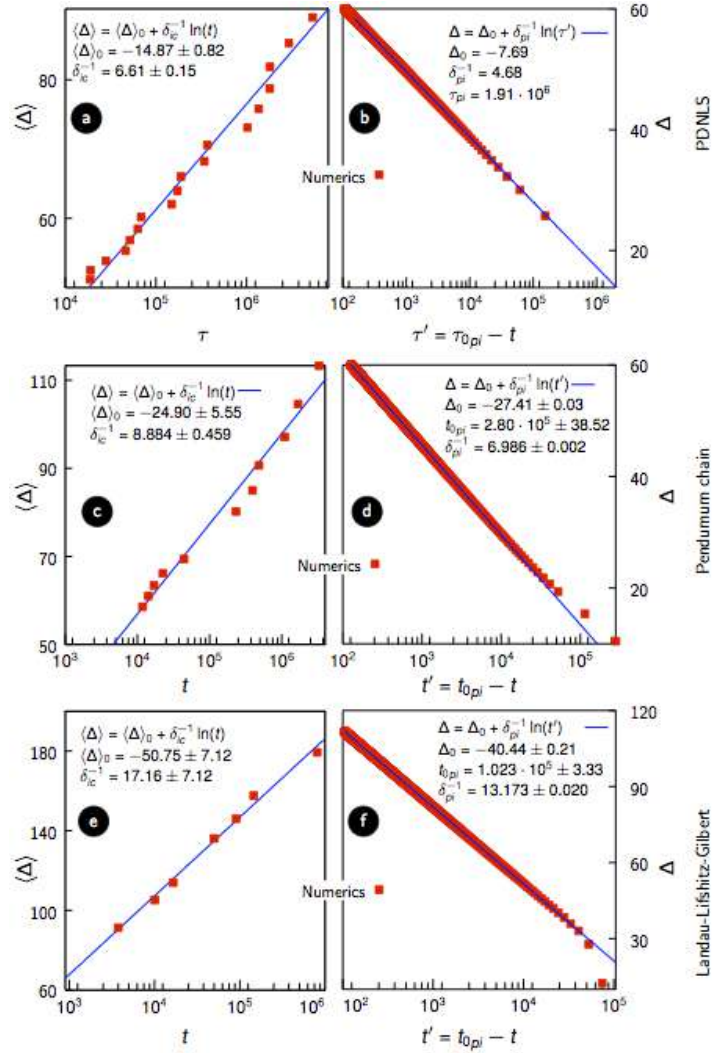


Figure 3.26: Ley de la distancia promedio entre solitones o dinámica de dominios para a) la ecuación paramétrica de Schrodinger no-lineal, b) cadenas de péndulos forzado verticalmente, c) modelo magnético forzado.

hopes to find laws that characterize the dynamics of the time evolution of the average distance between solitons. The characteristic distance between s solitons is given by

$$\langle \Delta(t) \rangle = \frac{\sum_{i=0}^{s-1} (z_{i+1} - z_i)}{N}, \quad (3.65)$$

with N the number of dissipative solitons. The dynamics of this function must be given by the interaction between solitons, equation (3.62). Therefore this must also be invariant by the law of self-similarity, that is,

$$\Delta(t) \rightarrow \Delta(t) + \langle \Delta \rangle_0, \quad (3.66)$$

$$t \rightarrow t e^{3\delta \langle \Delta \rangle_0 / 2}, \quad (3.67)$$

Therefore the only function that respects this type of symmetry is

$$\langle \Delta \rangle = \langle \Delta \rangle_0 + \frac{2}{3\delta} \ln t, \quad (3.68)$$

Then the average distance as time evolves increases with a logarithmic law. Figure 3.26 shows the time evolution of the distance of parametrically forced dissipative solitons for various systems. In which a close agreement is found between theory and simulations [57]. Experimentally, it is complex to be able to create a soliton gas to verify the above law. In the vertically forced water channel, at least the order of up to four solitons is observed [57].

3.6 Solitons in an inhomogeneous medium

As we have seen in the previous sections, dissipative solitons exhibit properties similar to particles. A question of interest that naturally emerges is the possibility of being able to manipulate or control the positions of dissipative solitons. An intuitive way of causing solitons to propagate is by breaking the invariance of spatial translation, that is, the medium that supports the solitons is inhomogeneous. The above can be achieved considering that the parameters are inhomogeneous

$$\begin{aligned} \mu &\rightarrow \mu_0 + \mu_1(x), \\ \gamma &\rightarrow \gamma_0 + \gamma_1(x), \\ \nu &\rightarrow \nu_0 + \nu_1(x). \end{aligned} \quad (3.69)$$

For the sake of simplicity, we will only consider that a single parameter is inhomogeneous, but the results obtained are similar if we consider the other inhomogeneous

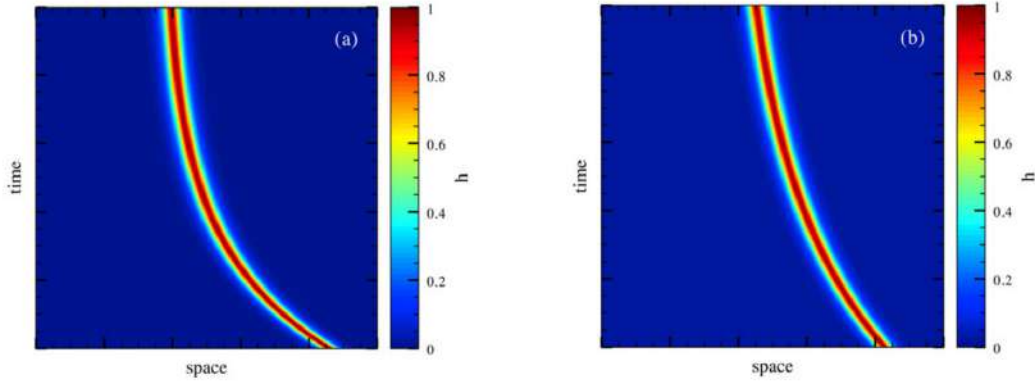


Figure 3.27: Spatiotemporal diagram of dissipative solitons in inhomogeneous media obtained through numerical simulations of the parametrically forced non-linear Schrödinger equation [103].

parameters.

$$\mu = \mu_0 + \mu_1(x),$$

and the rest are homogeneous. For example, in the case of a vertically driven channel, a small angle of inclination of the channel could induce a small inhomogeneous dissipation ($\mu_1(x) \ll 1$). Then equations (3.6) and (3.7) take the form

$$\begin{aligned} \partial_t R &= 2\partial_x R \partial_x \theta + R \partial_{xx} \theta - \mu R + \gamma R \cos(2\theta) - \mu_1(x) R, \\ R \partial_t \theta &= \nu R - R^3 - \partial_{xx} R + R(\partial_x \theta)^2 - \gamma R \sin(2\theta). \end{aligned} \quad (3.70)$$

One expects that for small angles, dissipative solitons are persistent. However, the lack of homogeneity generates two effects: (i) localized states are modified by the disturbance, they become asymmetric solutions, and (ii) the dissipative solitons' spatial translation mode—the Goldstone mode—acquires a dynamics as a result of the breaking of translational symmetry. Figure 3.27 shows the typical behavior of a dissipative soliton when one considers inhomogeneous dissipation that increases quadratically with the position. Therefore the dissipative solitons move towards the region of least dissipation. numerically, it was observed that the amplitude of the dissipative soliton increases when penetrating the regions of less dissipation.

To take these effects into account, the following ansatz is considered

$$\begin{aligned} R(x, t) &= R_+(x - x_0(t)) + r(x, x_0), \\ \theta(x, t) &= \theta_0 + \varphi(x, x_0), \end{aligned}$$

where $r(x, x_0)$ and $\varphi(x, x_0)$ are corrective functions, respectively. In addition, we will consider that the variable $x_0(t)$ is a slow temporary variable, that is, $\ddot{x}_0 \ll \dot{x}_0 \ll 1$, where $\dot{x}_0(t)$ is of the order of the disturbance. Introducing the above expressions into the set of equations (3.70) and linearizing in the disturbances after direct calculations, one finds

$$\begin{aligned} 2\partial_x \varphi \partial_x R_+ + \partial_{xx} \varphi R_+ &= 2\gamma \varphi \sin(2\theta_0) R_+ + \mu_1(x) R_+ \\ &\quad - \partial_z R_+ \dot{x}_0, \end{aligned} \quad (3.71)$$

$$\begin{aligned} R_+ \partial_t \varphi &= [\nu - \gamma \sin(2\theta_0) - 3R_+^2 - \partial_{xx}] r + \\ &\quad - 2\gamma R_+ \cos(2\theta_0) \varphi, \end{aligned} \quad (3.72)$$

where $z \equiv x - x_0(t)$ is the coordinate in the co-movable reference frame. Multiplying equation (3.71) by the integration factor R_+ and after simple calculations one obtains

$$\begin{aligned} \varphi(x) &= \int^x \frac{dx'}{R_+^2(x')} \int^{x'} dx'' \mu_1(x'') R_+^2(x') - \int^x \dot{x}_0 dx' \\ &\quad + \int^x \frac{2\gamma \sin(2\theta_0) dx'}{R_+^2(x')} \int^{x'} dx'' \varphi(x'') R_+(x'), \end{aligned} \quad (3.73)$$

which is a Fredholm integral for the field $\varphi(x)$ [10]. To solve the previous integral equation, we will consider the limit $\gamma \sin(2\theta_0) = \sqrt{\gamma^2 - \mu^2} \ll 1$, which is equivalent to considering an injection and dissipation of similar energy ($\gamma \sim \mu$). Based on this assumption, we can use the approximation

$$\varphi \approx \int^x \frac{dx'}{R_+^2(x')} \int^{x'} dx'' \mu_1(x'') R_+^2(x') - \int^x \dot{x}_0 dx'. \quad (3.74)$$

It is important to note that the corrections to the previous approximation can be calculated iteratively in a series of powers in the small parameter $\sqrt{\gamma^2 - \mu^2}$ [10]. Introducing the linear operator

$$\mathcal{L} \equiv \nu - \gamma \sin(2\theta_0) - 3R_+^2 - \partial_{xx},$$

equation (3.72) can be rewritten as

$$\mathcal{L}r = R_+ \partial_t \varphi + 2\gamma R_+ \cos(2\theta_0) \varphi. \quad (3.75)$$

To solve this linear equation, the Fredholm alternative is used. Consequently, the following inner product is introduced

$$\langle f|g \rangle = \int_{-\infty}^{\infty} f(x)g(x) dx.$$

The linear operator \mathcal{L} is self-adjoint ($\mathcal{L} = \mathcal{L}^\dagger$). The kernel of this linear operator is of dimension 1. As a result of the spatial translation invariance, one has $\mathcal{L}\partial_x R_+ = 0$, where $\partial_x R_+$ is the Goldstone mode associated with the spatial translation invariance. Then the field r has a solution if it is satisfied

$$0 = \langle \partial_x R_+ | R_+ \partial_t \varphi \rangle + \langle \partial_x R_+ | 2\gamma R_+ \cos(2\theta_0) \varphi \rangle. \quad (3.76)$$

Using the approximation (3.74), considering the dominant terms and after direct calculations one obtains Usando la aproximación (3.74), considerando los términos dominantes y después de cálculos directos uno obtiene

$$\dot{x}_0 = \frac{\int_{-\infty}^{\infty} dz \partial_z R_+ \int^z \frac{dx'}{R_+^2} \int^{x'} dx'' \mu_1(x'' + x_0) R_+(x'')}{\int_{-\infty}^{\infty} dz R_+ z \partial_z R_+}. \quad (3.77)$$

This equation accounts for the dynamics of the soliton as a consequence of inhomogeneity. It is trivial for parity arguments to see that, if $\mu_1(x)$ is an even function, then there are no corrections. Motivated by the experiment of the channel with water we can consider in the case of a small angle [103]

$$\mu_1(x) = \alpha x.$$

Then the formula (3.77) can be rewritten as

$$\begin{aligned} \dot{x}_0 = & \alpha \frac{\int_{-\infty}^{\infty} dz \partial_z R_+ \int^z \frac{dx'}{R_+^2} \int^{x'} dx'' x'' R_+(x'')}{\int_{-\infty}^{\infty} dz R_+ z \partial_z R_+} \\ & + \alpha x_0 \frac{\int_{-\infty}^{\infty} dz \partial_z R_+ \int^z \frac{dx'}{R_+^2} \int^{x'} dx'' R_+(x'')}{\int_{-\infty}^{\infty} dz R_+ z \partial_z R_+}. \end{aligned} \quad (3.78)$$

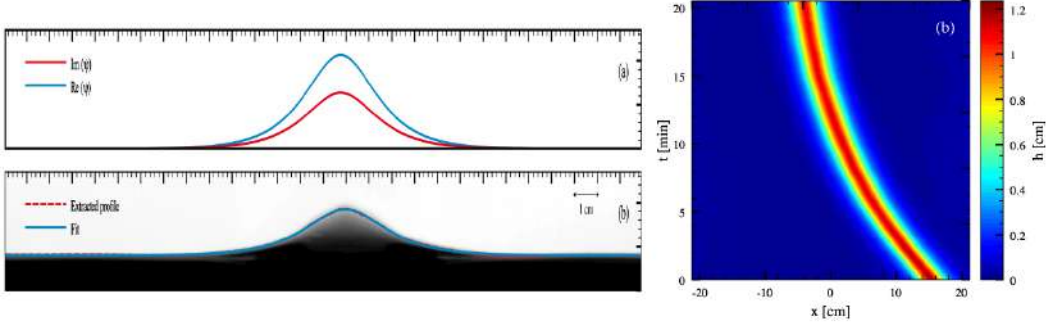


Figure 3.28: Hydrodynamic soliton evolution in a chute. a) snapshot image and b) space-time diagram [103].

Using expression (3.38) and parity arguments

$$\dot{x}_0 \approx \alpha \frac{\int_{-\infty}^{\infty} dz \partial_z R_+ \int^z \frac{dx'}{R_+} \int^{x'} dx'' x'' R_+(x'')}{\int_{-\infty}^{\infty} dz R_+ z \partial_z R_+}. \quad (3.79)$$

The previous integral can be estimated numerically, then we obtain [103]

$$\dot{x}_0 \approx -\frac{1.65327}{\delta^{3/2}} \alpha.$$

In the limit under consideration, the soliton propagates with constant speed. Therefore, if one considers a branch which can be changed $\alpha(t)$, then one can position the soliton wherever one wants. However, as the soliton propagates it changes its shape and this can generate new corrections for velocity.

Experimentally, it is observed that detuning is quadratic (see reference [103]), this is because the edges of the channel induce an effective force that forces the soliton to propagate to the center of the container. This type of inhomogeneity plus the inclination make the hydrodynamic soliton tend to carry out relaxation paths at equilibrium. This type of trajectory is illustrated in Figure 3.28.

3.7 Phase Shielding Dissipative solitons

Recently, numerical observations of dissipative solitons of the parametrically forced nonlinear Schrödinger equation show that the phase has a complex structure [58, 63],

called *phase shielding dissipative solitons*. Figure 3.29a illustrates the dissipative soliton studied in the previous sections, that is, a soliton characterized by a bell shape in the amplitude module and homogeneous phase described by formulas 3.12. Figure 3.29b illustrates a phase shielding dissipative soliton. These solutions are characterized by a similar bell structure for the module and a structure with different phase jumps. These solutions were discovered by simply disturbing the dissipative soliton and observing the evolution of its respective phase. It is important to mention that the phase presents a slower dynamic than the module. Initially, the phase exhibits complex transients. Later, two counterpropagating fronts emerge that connect two homogeneous states that propagate with a relatively constant speed, away from the heart or position of the soliton (which is given by the position of the maximum in the soliton module). Finally, this front stops giving rise to the stationary solution that is dissipative solitons with armor. Figure 3.30 shows the temporal evolution of the counterpropagating phase fronts, where the speed as the counterpropagating phase fronts propagate is shown.

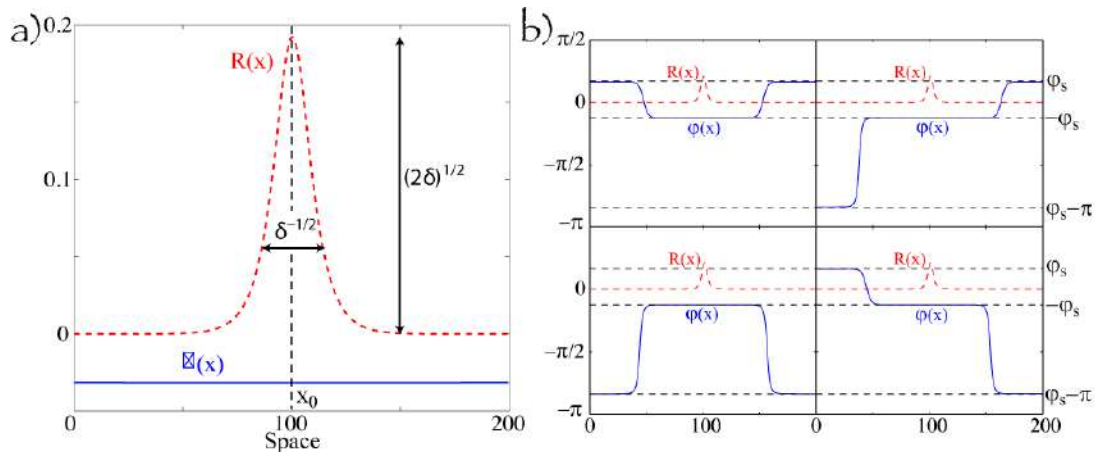


Figure 3.29: Dissipative solitons of the parametrically forced non-linear Schrödinger equation. a) homogeneous phase solitons, b) dissipative solitons with armor.

3.7.1 Analytical description

To understand the origin of these solitons, for the sake of simplicity, we will consider a coordinate system such that the position of the soliton is at the origin, and we will only consider the positive spatial coordinates. We will only consider a single-phase front for understanding the dynamics of dissipative phase shielding solitons. Naturally, the other half will be understood by a trivial extension of the above discussion. In figure 3.31a, the type of coordinate system under consideration is sketched. In this representation system, we observe that the front emerges away from the soliton's position (see 3.31a). Therefore for the dynamics of the phase front, the modulus can be approximated in this region to

$$R(x \gg \Delta, x_0) = 2\sqrt{2\delta_+}e^{-f(x, x_0)}, \quad (3.80)$$

and

$$\varphi(x) = \varphi_F(x - x_f), \quad (3.81)$$

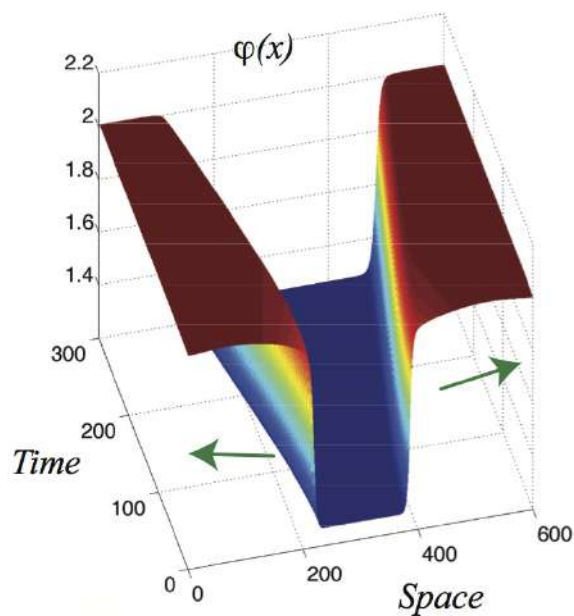


Figure 3.30: Spatiotemporal diagram of the phase fronts observed in the parametrically forced nonlinear Schrödinger equation (3.35).

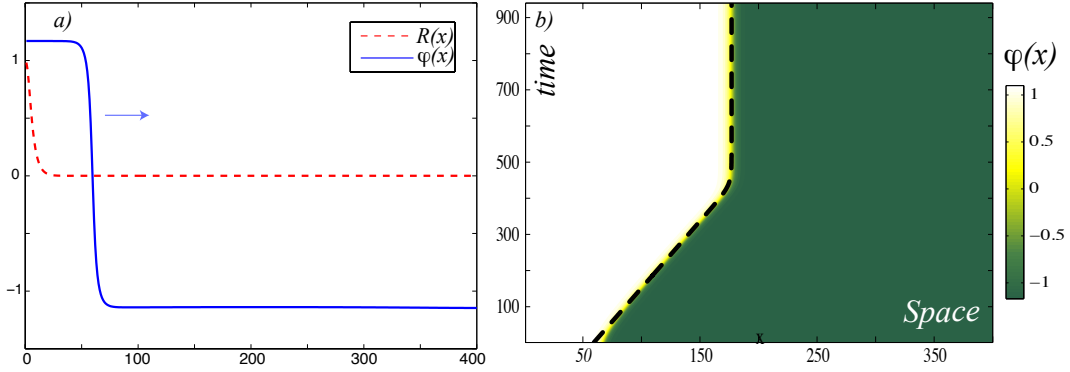


Figure 3.31: Phase front of a phase shielding dissipative soliton. a) profile of the phase front (continuous blue line) and modulus (dashed red curve), b) spatiotemporal diagram of the phase front.

Where x_f accounts for the position of the phase front. In the dominant order we can consider $f(x, x_0) \approx \sqrt{\delta_+}(x - x_0)$. In this approximation, $R(x, x_0)$ coincides with the exponential decay of the stable dissipative soliton solution with a homogeneous phase. Substituting the previous ansatz in the equations of the modulus and phase, equations (3.6) and (3.7), we obtain two different equations. The first allows us to obtain the dominant profile of the phase front analytically. The second describes the dynamic behavior versus phase; that is, it describes the equation for the phase front. Consequently, the phase profile is characterized by the equation

$$\partial_{xx}\varphi_F = 2\sqrt{\delta_+}\partial_x\varphi_F + \mu - \gamma \cos(2\varphi_F). \quad (3.82)$$

Introducing the following effective potential $U(\varphi_F) \equiv -\mu\varphi_F + \gamma/2 \sin(2\varphi_F)$, equation (3.82) can be written as a Newton-type equation, which describes a particle at a periodic potential with a constant force, with an energy injection term proportional to speed ($\partial_x\varphi_F$), that is,

$$\partial_{xx}\varphi_F = -\frac{\partial U}{\partial \varphi_F} + 2\sqrt{\delta_+}\partial_x\varphi_F. \quad (3.83)$$

Then, the solutions of the previous equation correspond to stationary solutions. In particular, the phase fronts correspond to heteroclinic solutions. The uniform equilibria in equation (3.82) coincide with the phase equilibria, that is, $\cos(2\varphi_s) = \mu/\gamma$ in the range of interest $-\pi$ to π . Therefore, the phase fronts represent homoclinic solutions in

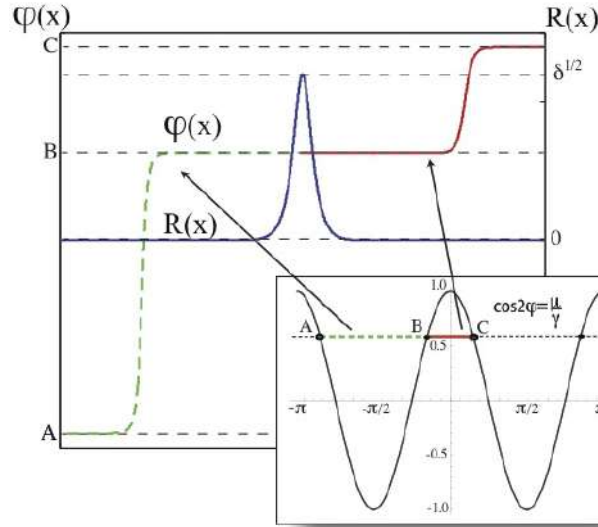


Figure 3.32: Phase shielding soliton, an illustration of phase fronts as heteroclinic curves.

the space $\{\varphi, \varphi_x\}$, which correspond to orbits that connect one equilibrium of Newton's equation with another state (3.83) (see Fig. 3.32).

Introducing the following change of variable $x = 2\sqrt{\delta_+}x'$ in Eq. (3.83), one can consider the following asymptotic series

$$\varphi_F(x) = \varphi_0 + \Gamma\varphi_1(x) + \Gamma^2\varphi_2(x) + \dots,$$

with $\Gamma \equiv 1/4\delta \ll 1$, which to the dominant order has the following analytic form

$$\varphi_F(x, x_f) \approx \varphi_0 = \begin{cases} f_{sol} - \pi, & [-\pi, -\frac{\pi}{2}) \\ f_{sol}, & [-\frac{\pi}{2}, \frac{\pi}{2}) \\ f_{sol} + \pi, & [\frac{\pi}{2}, \pi) \end{cases}$$

where

$$f_{sol} = \arctan \left[\sqrt{\frac{\gamma \pm \mu}{\gamma \mp \mu}} \tanh \frac{\sqrt{\gamma^2 - \mu^2}(x - x_f)}{2\sqrt{\delta_+}} \right]. \quad (3.84)$$

It is important to note that the phase fronts are parameterized by the x_f parameter. Figure 3.31a shows the phase front calculated numerically, which has a difference of 1 % with respect to the previous analytical expression. If one considers the corrections $\varphi_F \approx \varphi_0 + \partial_x \varphi_0 / 4\sqrt{\delta}$ the difference is reduced to 0.8 %.

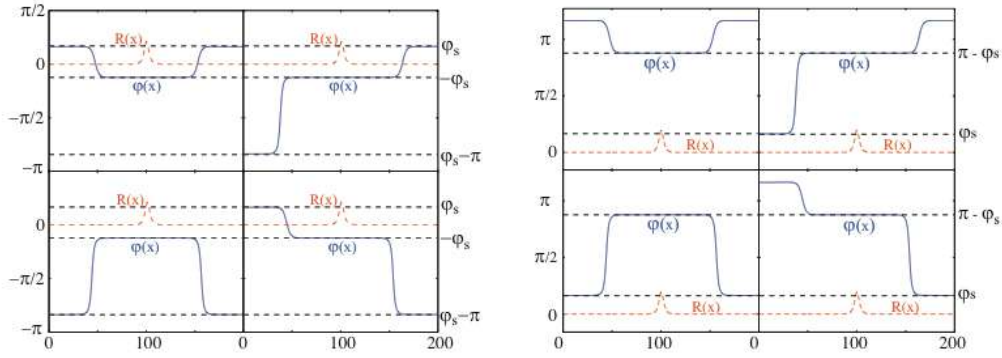


Figure 3.33: Phase shielding soliton family. The segmented curves account for the amplitude, and the continuous curves account for the different phase structures.

Considering the complete domain of the soliton, we obtain the eight possible configurations of armored solitons that we have previously observed in numerical simulations. The family of different armored solitons is illustrated in Figure 3.33.

A more careful analysis of numerical simulations reveals that phase shielding solitons are made up of two qualitatively different regions: the inner and outer regions. The inner and outer regions are highlighted by the central and asymptotic part of the phase shielding soliton. Note that the asymptotic phase of armored solitons in the inner and outer regions coincides with the phase of stable and unstable homogeneous phase solitons, respectively (see Figure 3.34). Therefore, phase shielding solitons can be understood as a soliton built by the stable (inner zone) and the unstable (outer zone) of solutions with homogeneous phases.

To illustrate this statement, Fig. 3.34 shows the logarithm of the modulus of phase shielding solitons as a function of space. Clearly, there is an intermediate region between the two exponential decay rates of solitons with a homogeneous phase that is characterized by a transition point. This point describes the transition between the inner and outer regions and corresponds to the center position versus phase x_f . Therefore, the exponential decay rate $f(x, x_0)$ of the armored solitons must be modified by

$$f(x, x_0) \approx \sqrt{\delta_+}(x - x_0) + B(x, x_f) \quad (3.85)$$

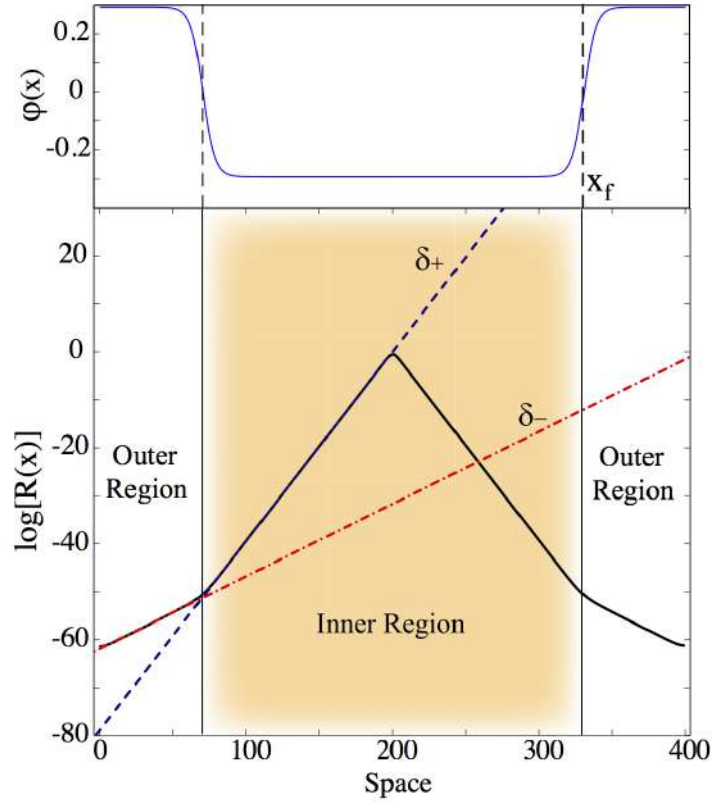


Figure 3.34: Structure of the phase shielding soliton. The upper image accounts for the phase structure, and the lower image accounts for the logarithm of the amplitude, which allows revealing the soliton's structure. The dotted curves account for the two asymptotic behaviors of the solitons with a uniform phase.

with

$$B(x, x_f) \equiv \left[\sqrt{\delta_-} - \sqrt{\delta_+} \right] \Theta(x - x_f)(x - x_f) \quad (3.86)$$

where $\Theta(x - x_f)$ accounts for the step function. It is important to note that the function $f(x, x_0)$ is a smooth function. However, approximation (3.85) is continuous but not differentiable at $x = x_f$.

Using the corrected ansatz 3.85, in equations (3.82-3.83), one can re-obtain the previous results in the inner and outer region. In the interior region, Eqs. (3.82-3.83) remain unchanged. On the other hand, these equations are modified by replacing δ_+ por δ_- in the outer region. Following the procedure shown above, one finds after direct

calculations the following expression for the phase front,

$$\varphi_0(x) = \arctan \left[\sqrt{\frac{\gamma \pm \mu}{\gamma \mp \mu}} \tanh \frac{\sqrt{\gamma^2 - \mu^2}(x - x_f)}{2\delta(x, x_f)} \right] \quad (3.87)$$

with

$$\delta(x, x_f) \equiv \left[\sqrt{\delta_+} + (\sqrt{\delta_-} - \sqrt{\delta_+})\Theta(x - x_f) \right]. \quad (3.88)$$

In this approximation, the phase fronts are continuous but not differentiable at $x = x_f$. Emphasizing that the phase shielding solitons are constituted by the stable and unstable soliton of the homogeneous phase.

Note that ansatz (3.80) considers a uniform exponential decay rate of the modulus. This assumption, to the dominant order, to obtain solutions versus phase (formula 3.84). Higher-order corrections allow us to obtain an improved description of the phase armored soliton in which the module also presents a shielding structure in the amplitude (see figure 3.34). However, this structure is suppressed exponentially compared to the soliton height $\sqrt{2\delta_+}$, by several orders of magnitude in the numerical simulations, at least 50 orders of magnitude are observed. In contrast, the phase structure is of order one. Therefore, a possible experimental characterization of phase shielding solitons must be achieved by means of phase measurements.

3.7.2 Phase dynamics

As discussed in the previous section, the transient behavior before forming the phase front is governed by the dynamics of the phase fronts. Here we propose an analytical study of the dynamic evolution of these fronts. To do this, we will consider the typical evolution of a soliton in a semi-infinite system, as shown in figure 3.31b. As can be seen from this figure, the front shows a dynamic behavior that is characterized by a non-trivial movement. For the sake of simplicity, consider the ansatz (3.80)-(3.81) to the dominant order that $f(x, x_0) \approx \sqrt{\delta}(x - x_0)$ and $\delta \equiv \delta_+$. Replacing in equation (3.7), the equation of the front position is obtained,

$$-\dot{x}_f \partial_x \varphi_F = -(\nu + \delta) - 8\delta e^{-2\sqrt{\delta}x} + (\partial_x \varphi_F)^2 - \gamma \sin(2\varphi_F). \quad (3.89)$$

To derive the dynamics of the phase front $x_f(t)$, one allows the position of the phase front to be promoted to a time function. The time derivative of x_f is given by \dot{x}_f . One assumes that this variable x_f is a slow variable.

Multiplying the above equation by $\partial_z \varphi_F(z)$ with $z \equiv x - x_f$, and introducing the following inner product $\langle f|g \rangle \equiv \int f g dz$, we obtain, after simple calculations, an ordinary differential equation for the position of the front phase,

$$\dot{x}_f = A + B e^{-2\sqrt{\delta} x_f}, \quad (3.90)$$

where

$$A \equiv \frac{\langle (\nu + \delta + \gamma \sin(2\varphi_F) - (\partial_z \varphi_F)^2) | \partial_z \varphi_F \rangle}{\langle \partial_z \varphi_F | \partial_z \varphi_F \rangle},$$

and

$$B \equiv 8\delta \frac{\langle e^{-2\sqrt{\delta} z} | \partial_z \varphi_F \rangle}{\langle \partial_z \varphi_F | \partial_z \varphi_F \rangle}.$$

$\{A, B\}$ are real numbers, which can be positive or negative depending on the shape of the phase front.

For example, when considering a phase front that increases monotonically with the spatial coordinate, A (B) has a constant negative (positive) value. The term proportional to A in the kinematic equation for the position of the front (Eq. 3.90) represents the constant speed at which the phase with the highest value invades the smallest, giving rise to a phase front that propagates towards the position of the soliton x_0 . This speed can be understood as a consequence of the difference in effective potential energy ($U(\varphi_F)$) between both equilibria. In contrast, the term proportional to B accounts for the effect of the spatial variation of the tail of the soliton in the amplitude or modulus, which induces a force that leads the phase fronts to move away from the position of the soliton. Consequently, the superposition of these two antagonistic forces generates a stable equilibrium of the position of the phase front, which is consistent with the dynamic behavior illustrated by the spatiotemporal diagram of Figure 3.31b. Solving equation (3.90), an analytical solution for the typical trajectory is obtained,

$$x_f(t) = \frac{\log\left(\frac{B}{A}\right)}{2\sqrt{\delta}} + \frac{\log\left(e^{-2\sqrt{\delta}A(t-t_0)} - 1\right)}{2\sqrt{\delta}} - A(t-t_0). \quad (3.91)$$

The dashed curve shown in figure 3.31b is obtained using the above formula where A and B are used as fit parameters. It is important to note that the constant $\log(B/A)/2\sqrt{\delta}$ describes the equilibrium position of the front, which corresponds to the characteristic size of the shell structure in phase. For higher-order phase corrections, a similar expression is obtained for the phase front dynamics.

3.7.3 Soliton stability with homogeneous phase

As we have already shown, solitons, with uniform phase and phase structure, are solutions of the parametrically forced non-linear Schrodinger equation (3.4). Therefore, a natural question that arises is: what are the fork scenarios of these solutions? In order to examine this question, one can perform a numerical linear stability analysis similar to that performed in Ref. [17]. Given the complexity of the linear operator, an analytical stability analysis is not affordable. We consider that a small disturbance ρ and Ω around the solution of $R_s(x)$ and φ_0 , respectively, that is,

$$R = R_s(x) + \rho(x, t) \quad \text{and} \quad \varphi = \varphi_0 + \Omega(x, t), \quad (3.92)$$

where $\rho, \Omega \ll 1$. Introducing in (3.6), (3.7) and linearizing, one obtain

$$\partial_t \rho = 2\partial_x R_s \partial_x \Omega + R_s \partial_{xx} \Omega + 2\sqrt{\gamma^2 - \mu^2} \Omega R_s, \quad (3.93)$$

and

$$R_s \partial_t \Omega = \delta \rho - 3R_s^2 \rho - \partial_{xx} \rho - 2\mu R_s \Omega, \quad (3.94)$$

respectively. The above equation can be rewritten as follows

$$\begin{pmatrix} \dot{\rho} \\ \dot{\Omega} \end{pmatrix} = M \begin{pmatrix} \rho \\ \Omega \end{pmatrix} \quad (3.95)$$

where

$$M \equiv \begin{pmatrix} 0 & 2\partial_x R_s(x)\partial_x - R_s(x)\partial_{xx} - 2R_s(x)\sqrt{\gamma^2 - \mu^2} \\ \frac{1}{R_s(x)}(\delta - 3R_s(x)^2 - \partial_{xx}) & -2\mu \end{pmatrix} \quad (3.96)$$

Analytical solutions of equation (3.95) is a complex task [17]. Therefore, one must use numerical analysis as a study strategy, that is, by means of numerical methods, one must determine the set of eigenvalues (*spectrum*). Then to calculate this spectrum, one proceeds to discretize the space, $x \rightarrow j\Delta x$, $F(x, t) \rightarrow F(j\Delta x, t) \equiv F_j(t)$ with $j = 1, \dots, N$ where N is the number of points considered in the system and $j = 1, \dots, N$. Therefore, the differential operator M becomes a matrix of rank N^2 . Furthermore, one can consider $\mu = \mu_0$ and $x_0 = L/2$ for different values of $\{\gamma, \nu\}$ in the region of existence of solitons, that is, $\gamma^2 \leq \nu^2 + \mu^2$ and $\nu < 0$.

The L parameter controls the size of the system and accounts for spatial effects. By changing N with Δx fixed, we can easily modify this parameter. In many studies, this parameter has not been considered as a relevant system parameter, being generally a small constant number. We will see that the parameter L plays a major role in the stability properties of localized dissipative states.

Therefore, we are going to consider L as a control parameter of the system and set the parameters $\{\mu, \nu, \gamma\}$. When L is small enough the spectrum is characterized by being centered on an axis parallel to the imaginary one, where each eigenvalue has a negative real part. This type of eigenvalue behavior is typical of quasi-reversible systems [45]. By increasing L , the set of eigenvalues begin to collide and give rise to the creation of a continuous set. Up to a critical value of L_c , where some of them cross the imaginary axis at a non-zero frequency, showing an Andronov-Hopf bifurcation [194, 108]. Figure 3.35 describes the spectrum before, during, and after the bifurcation, respectively. This figure illustrates the real part of the highest max auto value $\max[Re(\lambda)]$ (red points) and the eigenvalue related to the Goldstone mode (blue triangles) as a function of the size of the L system. As a consequence of the translation invariance, the eigenvalue related to the Goldstone mode is at the origin of the complex plane [172]. For $\gamma = 0.105$, $\mu = 0, 1$, and $\nu = -0, 05$, it is observed that (see Fig. 3.35 box A) below the critical

value $L_c = 304$, the largest eigenvalue corresponds to the Goldstone mode. Near the bifurcation, the eigenvalue with the greatest real part and its respective conjugate cross the real axis, giving rise to the destabilization of the uniform phase solution (see Fig. 3.35).

Analysis of the numerical stability of solitons with uniform phase reveals a strong dependence on the size of the system. This result is in agreement with the inner and outer crossover region. The inner region has a length defined by the given set of system parameters $\{\mu, \nu, \gamma\}$. If the size of the system is small enough (L less than the size of the inner region), the crossover does not occur. So the soliton with phase structure does emerge, and the soliton with uniform phase is the only stable solution. For L greater than the size of the inner region, the soliton with uniform phase is destabilized by an oscillatory bifurcation, generating the emergence of solitons with phase structure.

Since the exponential decay of stable uniform phase solitons, and therefore the length

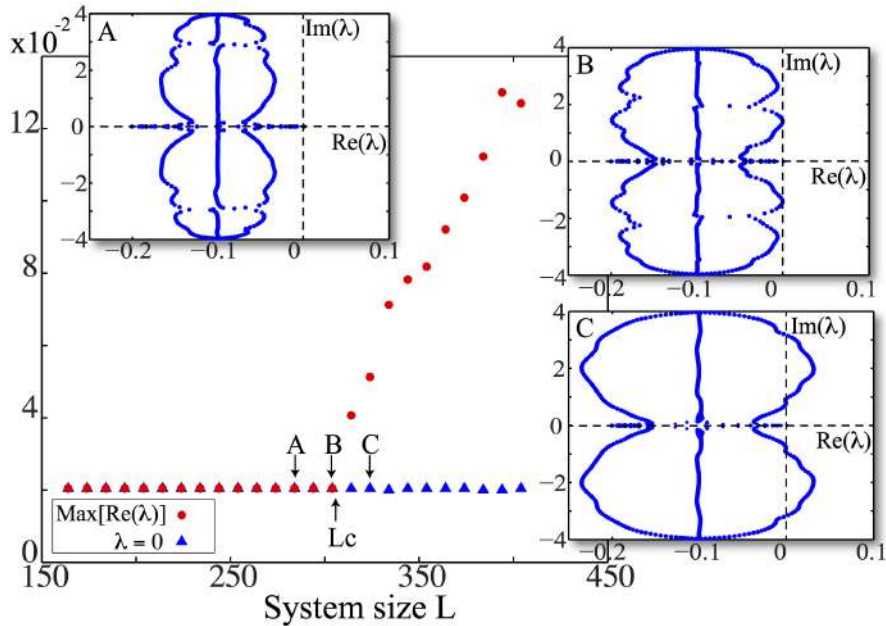


Figure 3.35: The real part of the largest eigenvalue $\text{Max}(\text{Re}(\lambda))$ (red dots) and Goldstone-related eigenvalues (blue triangles) as a function of system size. The inserted figures A, B and C are the spectrum of the soliton with homogeneous phase before ($L = 284$), during ($L = 304$), and after ($L = 324$) of the bifurcation, respectively, for $\gamma = 0.105$, $\mu = 0.1$, and $\nu = -0.05$.

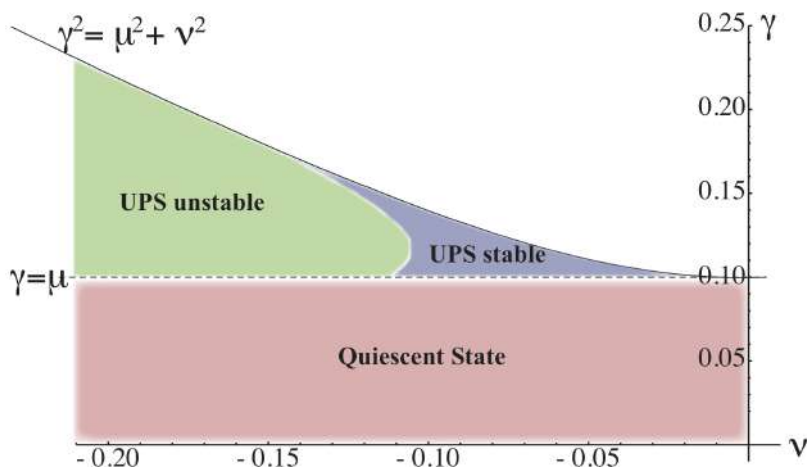


Figure 3.36: PSS bifurcation diagram in the $\gamma - \nu$ space obtained from solving 3.95 numerically for $\mu = 0.050$ and $L = 400$.

of the interior region, is a function of the parameters of the system $\{\mu, \nu, \gamma\}$, it is natural to infer that the variation of these parameters with L fixed, they can generate the destabilization of solitons with a uniform phase. Indeed, as a result of the previous strategy, we carry out an analysis of the numerical stability of these solutions varying γ for L fixed with $\mu = 0, 1$ and $\nu = -0.05$. We choose the same parameter region $\{\nu, \gamma\}$ with $L = 280$ (before the bifurcation generated by the change of the system size, see Fig. ??) to ensure that the soliton with uniform phase is stable. Figure ?? shows the eigenvalue evolution as a function of γ . As before, up to a certain critical value of γ_c , the system exhibits an Andronov-Hopf bifurcation, leading to the appearance of solitons with phase structure. The branching scenario is similar to that observed by resizing the system.

In summary, the mechanism of the above instability is a robust phenomenon. Figure 3.36 shows the stability of uniform phase solitons over a region of parameter $\{\nu, \gamma\}$ with $\mu = 0, 05$ and $L = 400$ fixed. For a system of size smaller than the critical one, it is observed that for the parameters $0 < \gamma\mu \ll 1$, the soliton with constant phase is stable. However, increasing the amplitude of the forcing γ for the detuning parameter ν , the soliton is again destabilized by an Andronov-Hopf bifurcation.

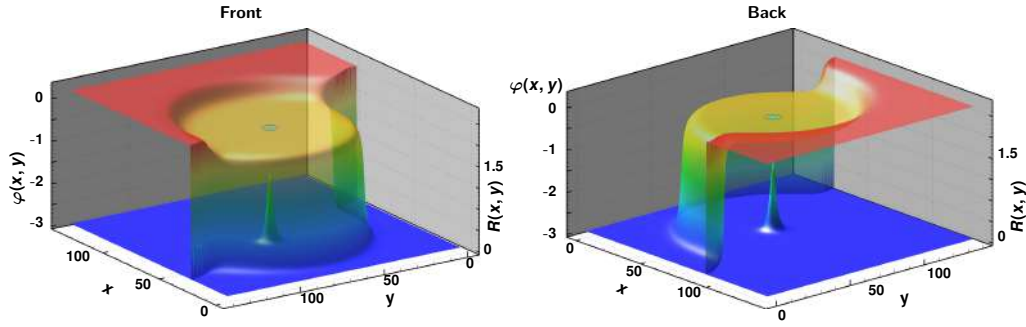


Figure 3.37: Front and back view of a stationary phase shielding soliton observed in two-dimensions for the parametrically driven nonlinear Schrödinger equation with $\gamma = 0.140$, $\nu = -0.068$ and $\mu = 0.125$. Phase and amplitude field are represented simultaneously. Colored shadow renders the phase shell-like structure ($\varphi(x, y)$) that surrounds the amplitude soliton localized at the center ($R(x, y)$).

In the case that the size of the system is large enough, the uniform phase soliton exhibits an Andronov-Hopf bifurcation leading to an armored soliton. Increasing still more the system parameters $\{\nu, \gamma\}$ a secondary bifurcation leads to a periodic behavior like those observed in [29]. In contrast, for small L s the Andronov-Hopf bifurcation leads directly to localized periodic solitons without a secondary bifurcation.

3.7.4 Phase shielding solitons in two-dimensions

To study the robustness of the phase dynamics around the soliton, we consider the two-dimensional spatial extension of Eq. (3.4), that is, ∂_{xx} operator is replaced by a two-dimensional Laplacian operator $\nabla^2 = \partial_{xx} + \partial_{yy}$ (cf. Eq. 3.35). As we have shown (see Sec. 3.3.1), this equation has soliton type solutions with constant phase [20], which are the natural extension of one-dimensional case. However an analytical expression for these solutions is unknown. Considering a similar parameter region of phase shielding solitons in one-dimension, we observe a rich phase fronts dynamics in two-dimensions. If one slightly perturbs the soliton, after some complex transient in the phase dynamics we observe the appearance of a circular phase front that spreads slowly. For later times, the front becomes asymmetric, giving rise to another front. Finally, the two fronts become stationary, creating a shield-like structure around the soliton. Figure 3.37 shows the

stationary phase structure observed numerically in a two-dimensional system. It is important to note that we only see phase shielding structure as a state of equilibrium for dissipative soliton in a large system size. The two-dimensional solution is characterized by being composed by all the solutions found in one-dimension. Indeed, if one performs different cuts containing the center (soliton position), one can recognize the observed solutions in one-dimension. A surprising property of the shell-like structure observed is that if one calculates the phase change in a closed path ($\oint_{\Gamma} \vec{\nabla} \varphi d\vec{s}$) within the region close to the position of the soliton one finds that this is zero. Nevertheless, if one takes a closed path in the exterior region of the soliton position, one finds $\oint_{\Gamma} \vec{\nabla} \varphi d\vec{s} = \pm\pi$. Therefore phase shielding solitons have a complementary property to the topological defects, which are characterized by having a phase change in the neighborhood of the defect equal to πn with n an integer number.

In brief, localized structures in parametrically forced systems have a rich and unexpected phase dynamics, creating novel types of localized states. We expect that phase shielding solitons could be observed experimentally in simple coupled forced oscillators, such as a vertically driven fluid layers in narrow cells, optical parametrical oscillators, driven magnetic media, and chain of coupled oscillators. Shell-like phase structure must play a significant role in soliton interaction, since bound states of two solitons show a complex phase structure. Experimental observations show an intricate temporal dynamics of dissipative solitons which cannot be explained from constant phase solitons.

Chapter 4

Dissipative solitons in forcing systems

Main characteristic of an oscillator is to possess an intrinsic natural frequency. Forcing at this particular frequency is the natural way to excite an oscillator in an efficient way. When forcing an oscillator close to its natural frequency, the oscillator exhibits a large oscillation amplitude, which can be understood from a balance between the injection (forcing) and the dissipation of energy (dissipation). This is a *resonance* phenomenon [131]. The resonance phenomenon has been known since the dawn of modern science by Galileo [98], who was interested in the understanding of the pendulum dynamics. Depending on the intensity and the frequency of the forcing this oscillator begins to manifest its nonlinear nature, with an asymmetric amplitude response with respect to the forcing frequency [131]. Likewise, by sufficiently large forcing intensity the oscillator can exhibit bistability between two equilibria oscillations [131]. When increasing the forcing amplitude, the system may exhibit complex chaotic type behaviors (see the textbook [16] and reference therein). The previous scenario changes drastically when one considers a spatial extension of the nonlinear oscillator. In the latter case one expects the emergence of nonlinear phenomena such as patterns, localized solutions, fronts, nonlinear waves, chaos, chimera states, phase turbulence, spatiotemporal chaos, weak turbulence, among others. Due to the complexity of the nonlinear partial differential equations, only particular models close to conservative limits have

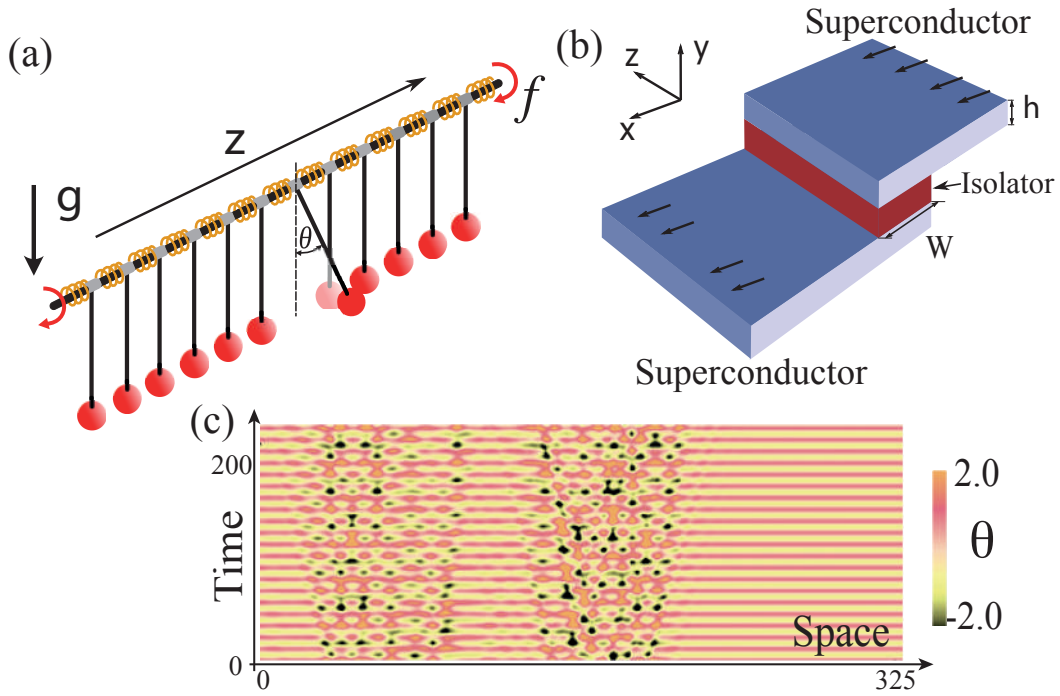


Figure 4.1: Driven damped nonlinear oscillators. (a) Schematic representation of a driven dissipative chain of pendula. θ is the angle formed by a pendulum and the vertical axis; $f = \gamma \sin(\omega t)$ accounts for an temporal modulating torque with an amplitude and frequency γ and ω , respectively. (b) Schematic representation of an extended Josephson junction, which is composed of two superconductors separated by an insulating strip. (c) Spatiotemporal evolution of a driven damped sine-Gordon Eq. (4.13), by $\omega_0 = 1$, $\mu = 0.05$, $\kappa = 1$, $\gamma = 5.9$, $\omega = 2.7$, $dt = 0.05$ and $dx = 0.65$ [91].

been studied analytically in detail (cf. Rev. [125] and references therein). A systematic study a chain of forced oscillators through *amplitude equations* [28, 152]. This type of approach is valid for small amplitude that has allowed a unified understanding of several phenomena such as pattern formation, localized structures, phase turbulence, defect turbulence, spatiotemporal chaos, weak turbulence, among others. In optics a natural nonlinear extended oscillators are cavities [146]. Therefore, by means of external electromagnetic waves with a frequency near to the cavity frequency, one expects to be able to resonate this optical cavity with the injection.

4.0.1 Josephson junctions an exceptional oscillator

The dissipative sine-Gordon equation (2.51) can be applied to another relevant physical system, namely an extended Josephson [76, 138]. Figure 4.2 displays a Josephson junction. To model these quantum elements, one can consider a quantum system consisting of two superconductors described by two wave functions ψ_1 and ψ_2 which is separated by an insulating film (see Fig. 4.2). When one applies a voltage difference, classically one does not expect to observe electrical conduction as result of the insulator, however, quantitatively one observe a current through the device, even without voltage (Josephson effect [115]). To describe this phenomenon, one can consider a two-state quantum system described by

$$i\hbar\partial_t\psi_1 = E_1\psi_1 + k\psi_2, \quad (4.1)$$

$$i\hbar\partial_t\psi_2 = E_2\psi_2 + k\psi_1, \quad (4.2)$$

where \hbar is the Planck constant, E_1 and E_2 account for the energy of the superconductor, $E_2 - E_1 = -qV$, where V is the voltage between superconductors and q the electrical charge, and k accounts for the coupling between superconductors (Evanescent coupling via wave-function tail overlap), which is determined by the properties and geometry of the insulating material. Introducing polar representation $\psi_l(t) \equiv \sqrt{\rho_l(t)}e^{i\phi_l(t)}$ ($l =$

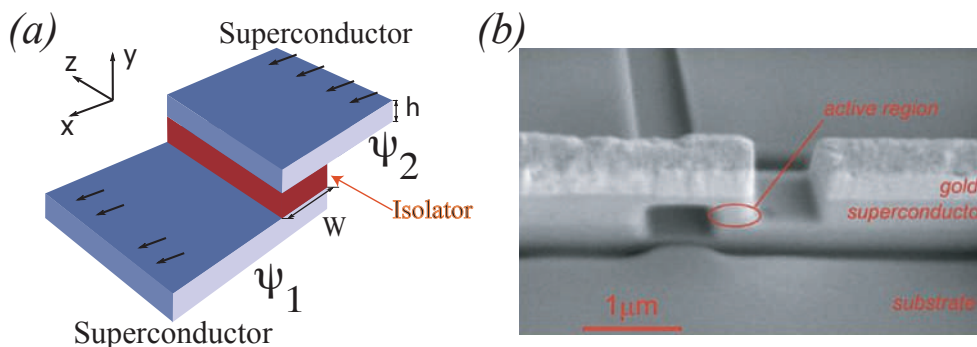


Figure 4.2: Josephson junctions. (a) Schematic representation of the Josephson junctions. ψ_1 and ψ_2 account for the amplitud probability of the superconductor state of the respective superconductor. (b) Snapshots of the Josephson junction

$\{1, 2\}$), where $\rho_l(t)$ accounts for the density of cooper pair, the set of equations read

$$\partial_t \rho_1 = \frac{k\sqrt{\rho_2\rho_1}}{\hbar} \sin(\phi_2 - \phi_1), \quad (4.3)$$

$$\partial_t \rho_2 = -\frac{k\sqrt{\rho_2\rho_1}}{\hbar} \sin(\phi_2 - \phi_1), \quad (4.4)$$

$$\partial_t \phi_1 = -\frac{E_1}{\hbar} - \frac{k}{\hbar} \sqrt{\frac{\rho_2}{\rho_1}} \cos(\phi_2 - \phi_1), \quad (4.5)$$

$$\partial_t \phi_2 = -\frac{E_2}{\hbar} - \frac{k}{\hbar} \sqrt{\frac{\rho_1}{\rho_2}} \cos(\phi_2 - \phi_1). \quad (4.6)$$

the current between superconductors is given by

$$J_s \equiv \partial_t \rho_1 = -\partial_t \rho_2 = \frac{k\sqrt{\rho_2\rho_1}}{\hbar} \sin(\phi_2 - \phi_1). \quad (4.7)$$

Hence, if there is a phase difference $\phi \equiv \phi_2 - \phi_1$ between the superconductors, there is a current. This phase difference satisfies

$$\partial_t \phi = \frac{qV}{\hbar} - \frac{k}{\hbar} \cos(\phi) \left[\sqrt{\frac{\rho_2}{\rho_1}} - \sqrt{\frac{\rho_1}{\rho_2}} \right]. \quad (4.8)$$

Considering that both states have the same density $\rho_0 \equiv \rho_1 = \rho_2$, one finds Josephson's relationships

$$J_s = \frac{k\rho_0}{\hbar} \sin(\phi), \quad (4.9)$$

$$\partial_t \phi = \frac{qV}{\hbar}. \quad (4.10)$$

Note that even without voltage ($V = 0$), but with a phase difference, one can see a quantum current (*Josephson effect* [115]). On the other hand, the current and the voltage are connected by means of Maxwell equations, particularly by

$$\left(\frac{\partial_{tt}}{c^2} - \nabla^2 \right) \vec{E} = \mu_0 \partial_t \vec{J}, \quad (4.11)$$

where \vec{E} and \vec{J} are the electric field and current between the superconductor, respectively. If the insulator is a thin film then $\vec{E} \approx -V/d \hat{y}$ with d the thickness of the insulator, and the current is composed of a normal and a superconductor current, $\vec{J} = (J_s + J_n)\hat{y}$. The normal current satisfies the Ohm law $J_n = -V/\eta d$ with η is the

resistivity. Using the Maxwell equation, Josephson relations, the previous approximation and assuming that phase difference depend of the transversal coordinate $\phi(x, t)$, one gets

$$\partial_{tt}\phi = -\frac{c^2 k \rho_0 d \mu_0}{\hbar^2 q} \sin \phi - \frac{c^2 \mu_0}{\eta} \partial_t \phi + c^2 \partial_{xx}. \quad (4.12)$$

Hence, the Josephson junctions is describe by the dissipative sine-Gordon equation, where the natural frequency depends of the density of cooper pairs, electric charge, constant of coupled between the superconductor, and the thickness of the insulator.

4.0.2 From driven damped sine-Gordon model to driven damped nonlinear Schrödinger equation (Lugiato-Lefever equation)

Let us consider a driven damped chain of pendula (cf. Fig. 4.1a), which is described, in the continuum limit, by a following forced dissipative sine-Gordon equation [18, 91, 177]

$$\ddot{\theta}(z, t) = -\omega_o^2 \sin \theta - \mu \dot{\theta} + k \partial_{zz} \theta + \gamma \sin(\omega t), \quad (4.13)$$

where $\theta(z, t)$ is the angle formed by a pendulum and the vertical axis in the z -position at time t ; ω_o is the natural frequency of the pendulum; μ , k , γ , and ω are the damping, elastic coupling, amplitude and frequency of the forcing, respectively. For the sake of simplicity, we have chosen a harmonic external forcing. The model Eq. (4.13) takes into account of the dynamics of a chain of coupled pendula to first neighbors by restitution springs [76], which are mounted on the horizontal bar that oscillates in a harmonic way with respect to its azimuthal axis (cf. Fig. 4.1a). Hence, the elastic bar induces an oscillatory torque on each pendulum.

The model Eq. (4.13) can be applied to another physical system, namely an extended Josephson junctions [76, 21]. The schematic of this system is depicted in Fig. 4.1b. In the following we provide the meaning of the variable and the parameters of the extended Josephson Junction. The variable $\theta(z, t)$ in Eq. (4.13) accounts for the phase difference between the wave function of each superconductors. The parameter ω_o^2 stands for the superconductor current in the junction and its value is determined by the particular

characteristics of the junction. The parameter μ accounts for the normal current, and the parameter k is proportional to the square of light speed. The term proportional to γ in Eq. (4.13) takes into account of the alternating current across the junction. Indeed, modifications of the sine-Gordon equation allows to describe different physical systems such as charge density waves [106], dislocations in crystal [35], magnetization of driven ferromagnetic wires [25], gravity and high-energy [76].

For zero forcing and damping, $\gamma = \mu = 0$, the above model describes a Hamiltonian system, that present time reversal invariance, which is well-know as the sine-Gordon model. Figure 4.1 illustrates a schematic representation of a driven dissipative chain of pendula. When the dissipation is included, the vertical state $\theta(z, t) = 0$ becomes the only stable equilibrium. The forcing induces oscillations of the vertical state with the forcing frequency. The amplitude of this oscillation strongly depends of the detuning between the forcing and natural frequency, $\nu \equiv \omega - \omega_0$. Figure 4.1c shows a complex spatiotemporal evolution of the driven damped sine-Gordon equation.

To figure out the dynamics observed in the driven damped sine-Gordon equation, we consider the quasi-reversal limit, that is, the time reversal limit perturbed with small injections and small dissipations of energy [45]. In this limit, model (4.13) corresponds to a perturbed sine-Gordon equation with $\nu \sim \mu \sim \varepsilon$, $\gamma \sim \varepsilon^{3/2}$, and ε is an arbitrary small scaling parameter, $\varepsilon \ll 1$. Considering the following ansatz

$$\theta = \sqrt{\frac{2\varepsilon}{3\omega_0}} A(x, \tau) e^{i\omega t} + \left(\frac{\varepsilon}{6\omega_0}\right)^{3/2} A^3 e^{i3\omega t} + c.c. + h.o.t., \quad (4.14)$$

where $A(x, \tau)$ is the slowly varying envelope of the vertical state, $\tau \equiv \varepsilon t$ and $x \equiv \sqrt{2\varepsilon\omega_0/k}z$ are slow variables, *c.c.* and *h.o.t.* denote the complex conjugate and the high order terms in amplitude A , respectively. Introducing the above ansatz in Eq. (4.13), and matching different orders in ε . After straightforward calculations, at the dominant order in ε , the envelope A obeys the driven damped nonlinear Schrödinger equation

$$\partial_\tau A = -(\tilde{\mu} + i\nu)A - i|A|^2 A - i\partial_x^2 A - \tilde{\gamma}, \quad (4.15)$$

where $\tilde{\mu} \equiv \mu/2$, and $\tilde{\gamma} \equiv \gamma/4\sqrt{2\omega/3}$. Notice that the terms of above equation are of order $\varepsilon^{3/2}$ and the higher order terms are at least of order $\varepsilon^{5/2}$.

The above amplitude equation is the paradigmatic one-dimensional Lugiato-Lefever equation [145] or the driven damped nonlinear Schrödinger equation [119, 153, 165]. The correspondence between the sine-Gordon model and the Lugiato-Lefever equation was established in Ref. [18].

Although the amplitude equation (4.15) was proposed for the first time in plasma [165] and coupled nonlinear oscillators [119, 153], its main use is in the context of nonlinear optics, where this model is known as the Lugiato-Lefever equation [145]. In their seminal paper, Lugiato and Lefever introduce for the first time the mean field approach to derive a simple model to describe the spatiotemporal evolution of the intracavity field envelope. An early report on transverse patterns, which describes numerical simulations of self-focusing and filamentation of light beams in bistable nonlinear media [135]. Later on Lugiato and Lefever, have shown that the existence of transverse patterns does not require a bistable homogeneous steady state [145]. They show that the symmetry breaking instability leading to the spontaneous formation of stationary spatial patterns can occur in the monostable regime far from any second-order critical point. More importantly, they have established the link between the well known symmetry-breaking instability in chemical reaction diffusion systems [149] and the transverse pattern in nonlinear optics [145].

The Lugiato-Lefever equation (4.15) have broad applicability than passive optical cavities and it is a well-known paradigm in the study of spatial periodic or localized patterns in optics. It has been considered for that purpose in diffractive systems such as liquid crystals, left-handed materials [129], and photonics coupled waveguides [170, 66]. It has been also derived for dispersive systems such as nonlinear fiber resonator [112] and whispering-gallery-mode microresonators leading to optical frequency comb generation [44, 109, 68]. The sign of the second derivative with respect the x coordinate is negative and the nonlinearity is of the focussing type. Depending of the context in which the Lugiato-Lefever equation is derived, the sign of nonlinearity and dispersion or diffraction can be positive or negative see classification in table 4.0.2. In optics the LLE model was derived considering the mean field limit of driven Kerr cavities with

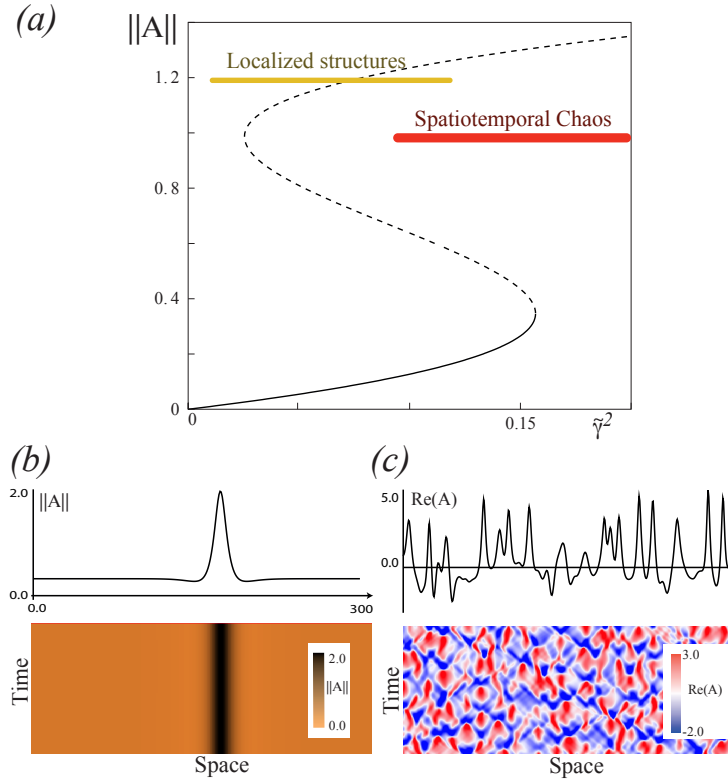


Figure 4.3: The driven damped nonlinear Schrödinger equation, Eq. (4.15). (a) Representative bifurcation diagram of the driven damped nonlinear Schrödinger equation Eq. (4.15) versus the forcing intensity for positive detuning in the bistable regime. The solid and the dashed curve account for the stable and the unstable uniform state. The colored bars account, respectively, for the parameter region where localized structures and spatiotemporal chaos are observed. (b) Instantaneous profile and spatiotemporal evolution of the amplitude $\|A\|$ for a localized structures. (c) Instantaneous profile and spatiotemporal evolution of $Re(A)$ in the spatiotemporal chaotic regime.

a high Fresnel number—assuming that the cavity is much shorter than the diffraction and the nonlinearity spatial scales.

	Diffraction	Dispersion	Nonlinearity
Passive cavity	+		\pm
LHM	\pm		\pm
Nonlinear Fiber		\pm	+
WGM		+	\pm
Chain of pendula		-	-
Josephson Junctions		-	-

Sign of diffraction, dispersion and nonlinearity. Passive cavity, diffraction is always positive while nonlinearity can be either positive or negative.

Cavity filled with Left-handed materials (LHM), diffraction and nonlinearity can be either positive or negative. Whispering-gallery-mode microresonators (WGM) leading to optical frequency comb generation. In the case of the chain of pendula both nonlinearity and dispersion are negative.

Figure 4.3 shows the typical bifurcation diagram of the Lugiato-Lefever equation with positive detuning in the bistable regime. The solid and the dashed curve account for the stable and the unstable uniform state, respectively. In addition, it is characterized the parameter region where localized structures and spatiotemporal chaos are observed numerically [139].

4.1 Localized structures

From the envelope Eq. (4.15), it is easy to characterize analytically the uniform equilibria. The uniform steady state response A of Eq. (4.15) satisfies $\gamma^2 = [\mu^2 + (\nu - |A|^2)]|A|^2$. For $\nu < \sqrt{3}\mu$, the steady, uniform state is a single valued function. For $\nu > \sqrt{3}\mu$ the system exhibits a bistable behavior with an S-shaped curve (see Fig. 4.3a). In contrast, in the driven damped sine-Gordon equation, the analytical

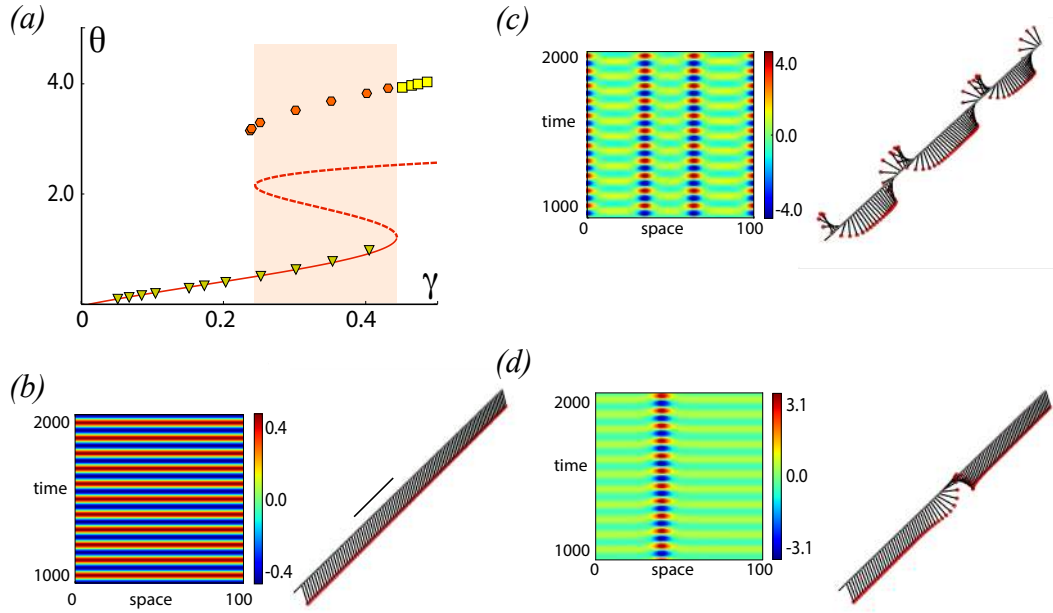


Figure 4.4: Dynamics of the driven dissipative chain of pendula model Eq. (4.13). (a) Bifurcation diagram: amplitude of the oscillation versus the forcing intensity γ . The solid and dashed curves account, respectively, for the stable and unstable uniform oscillation around the vertical state $\theta(x, t) = 0$. Triangular symbols corresponds to numerical observations of Eq. (4.13) with $\omega_0 = 1$, $\mu = 0.15$, $\kappa = 1$, $\omega = 2.7$, $dt = 0.05$ and $dx = 0.5$. Hexagonal and square symbols account for the maximum amplitude of localized structures and amplitude of the patterns, respectively. The painted area accounts for the coexistence region. Spatiotemporal evolution and schematic representation of an uniform oscillation $\gamma = 0.207$ (b), a standing wave $\gamma = 0.45$ (c), and a localized waves $\gamma = 0.3$ (d).

characterization of uniform oscillations far from the quasi-reversible limit is a complex endeavor. Numerically, we have calculated the amplitude of an uniform oscillation as function of forcing γ and have compared this oscillation amplitude with the oscillation amplitude that one obtains considering a single pendulum, avoiding spatial instabilities of the chain of pendula. Figure 4.4a summarizes the comparison between oscillation amplitude of a single pendulum (solid and dashed curve) and the numerical values of the amplitude of an uniform oscillation (triangular symbols). The uniform oscillation experience a modulation instability. This bifurcation leads to the formation of standing waves solutions (cf. Fig. 4.5).

The upper branch of this curve accounts for an uniform oscillation with large ampli-

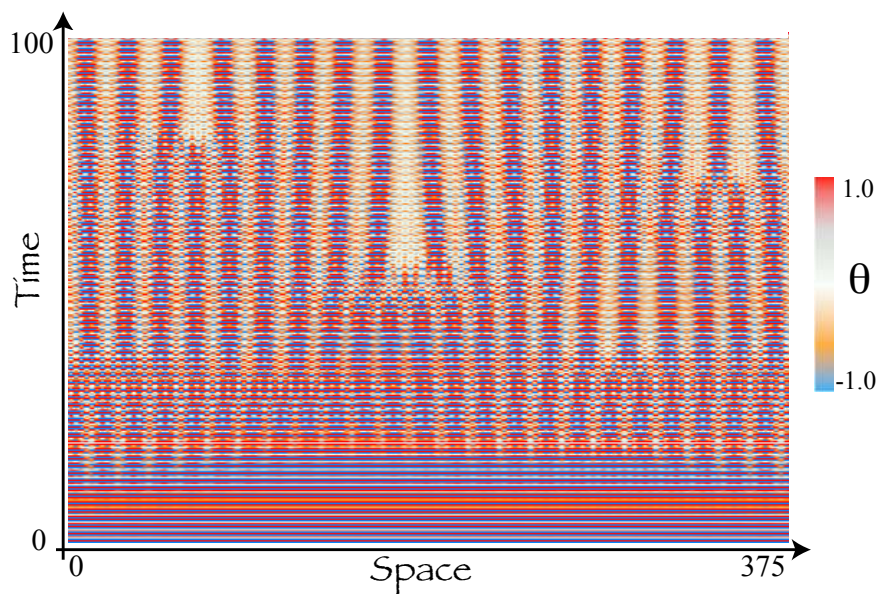


Figure 4.5: Spatiotemporal evolution of modulational instability of a driven damped sine-Gordon Eq. (4.13) with $\omega_0 = 1.0$, $\mu = 0.09$, $\kappa = 1.0$, $\gamma = 0.8$, $\omega = 2.7$, $dt = 0.076$ and $dx = 0.75$.

tude. Similar bifurcation diagram has been obtained theoretically and experimentally in a driven damped array of coupled pendula [168, 209]. Notwithstanding, this uniform oscillation is unstable as result of the Turing instability. Figure 4.4b displays the spatiotemporal evolution and a schematic representation of a uniform oscillation of the driven damped sine-Gordon model. Hence, the system exhibits a coexistence between a stable uniform oscillation and an unstable standing wave (cf. painted area of Fig. 4.4a).

In the coexistence area, one expects to observe localized structures [82, 175], which correspond to localized waves [61]. In the context of Lugiato-Lefever Eq. (4.15d), localized structures have been examined in one and in two dimensional LLE [186, 18, 19]. Figure 4.4d shows the spatiotemporal evolution and a schematic representation of a localized waves in a driven dissipative chain of pendula. Experimentally, this type of structure has been observed in a forced damped array of coupled pendula [168, 75]. From the uniform oscillation it is easy to obtain this localized state by considering a local perturbation. This particle type solutions are the dissipative counterpart of soliton solutions of the sine-Gordon equation. The localized wave is characterized by a

central peak accompanied laterally by two depressions in the amplitude (cf. Fig. 4.3b). The maximum of the amplitude of localized wave as function of the forcing intensity γ is represented by hexagonal symbols in Fig. 4.3a. For small strength of the forcing γ , these solutions appear by a saddle-node bifurcation. When increasing the forcing intensity these solutions becomes unstable by a radiation of complex spatiotemporal state [137, 139]. Indeed, the localized waves obtained with the driven damped sine-Gordon equation and the Lugiato-Lefever model are quite similar.

Outside the coexistence region and large strength of the forcing γ , one can observe stable standing waves, which correspond to the counterpart of the pattern state observed in the Lugiato-Lefever equation. Figure 4.4c depicts the spatiotemporal evolution and a schematic representation of a standing wave. These solutions come out from the unstable uniform oscillation—upper branch in Fig. 4.4a—as result of the modulational instability. Namely, from an initial homogeneous oscillation appears a small spatial modulation that increases systematically to a finite amplitude. However, this standing wave is unstable. It broke its spatial periodicity by several localized phase singularities, which allows the system to reach the adequate wavelength of the stable standing wave. Figure 4.5 illustrates the modulation instability process of an uniform oscillation. The phase singularities are recognizable by means of the dislocations observed in the spatiotemporal diagram [64]. In Fig. 4.4a the square symbols stand for the amplitude of the stable standing waves.

4.1.1 System without dissipation

Let us consider the non-dissipative driven nonlinear Schrödinger equation,

$$\partial_\tau A = -i\nu A - i|A|^2 A - i\partial_x^2 A - \gamma. \quad (4.16)$$

Note that we have neglected the dissipation ($\mu = 0$). In this limit the system corresponds to a Hamiltonian system with a forcing, that is,

$$\partial_\tau A = -i\frac{\partial\mathcal{H}}{\partial\bar{A}}, \quad (4.17)$$

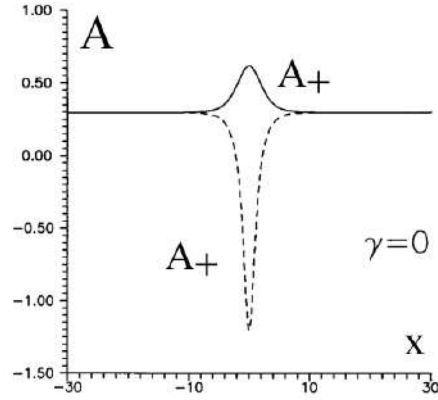


Figure 4.6: Analytical dissipative soliton using formula (4.20) for non-dissipative driven nonlinear Schrödinger equation (4.16) [18].

with

$$\mathcal{H} = \int dx \left(\nu |A|^2 + \frac{|A|^4}{2} + |\partial_x A|^2 + \gamma A + \gamma \bar{A} \right). \quad (4.18)$$

Note that the Poisson bracket has the form

$$\{f, g\} = \frac{\partial f}{\partial A} \frac{\partial g}{\partial \bar{A}} - \frac{\partial g}{\partial A} \frac{\partial f}{\partial \bar{A}}. \quad (4.19)$$

At this limit Barashenkov shows that the non dissipative driven nonlinear Schrödinger equation, has the following analytical solution [18]

$$A_{\pm} = \frac{1}{\sqrt{2(1 + 2 \cosh^2 \alpha)}} \left(1 + \frac{2 \sinh^2 \alpha}{1 \pm \cosh^2 \alpha \cosh^2(Ax)} \right). \quad (4.20)$$

Here α and A are defined by

$$\gamma = \frac{\sqrt{2} \cosh^2 \alpha}{(1 + 2 \cosh^2 \alpha)^{3/2}}, \quad (4.21)$$

$$A = \frac{\sinh \alpha}{\sqrt{1 + 2 \cosh^2 \alpha}}. \quad (4.22)$$

Figure 4.6 shows a chart of the analytical expressions (4.20).

For the dissipative driven nonlinear Schrödinger equation (4.15), $\mu \neq 0$, no exact solutions for dissipative solitons are available. The reason for the inaccessibility of analytical solutions is due to the fact that the associated spatial system $[A = A(x)]$

is not integrable. Therefore, the only accessible strategy is through numerical analysis. Figure 4.3b, a localized structure of the driven dissipative nonlinear Schrödinger equation (4.16) is shown, and oscillations around the central peak characterize this solution. From the point of view of homoclinic curves, it corresponds to homoclinic of the Shilnikov type [189, 50], which is typical of chaotic systems.

4.1.2 Quasi-reversal limit

For the sake of simplicity, we will consider the limit of the perturbative nonlinear Schrödinger equation (2.57). As we studied in section 2.3.3, this equation has a family of localized solutions, solitons, parameterized by the soliton's height, frequency, speed, and position [see formula (2.65)]. When considering dissipation, these solutions disappear; then, to stabilize this solution, one must consider energy injection through forcing. To characterize the localized solutions, let us write the perturbed equation (4.15) in polar representation

$$\begin{aligned}\partial_t R &= 2\partial_x R \partial_x \theta + R \partial_{xx} \theta + \gamma \cos(\theta) - \mu R, \\ R \partial_t \theta &= -\nu R - R^3 - \partial_{xx} R + R(\partial_x \theta)^2 - \gamma \sin(\theta).\end{aligned}\quad (4.23)$$

Let us consider the following ansatz [119, 153]

$$A = 2\eta \operatorname{sech} \left[\frac{\eta^2(x - x_0)}{2} \right] e^{i((\eta^2/2 - \nu)t + \sigma)} = \eta R_0(x) e^{i((\eta^2/2 - \nu)t + \sigma)}, \quad (4.24)$$

where $\eta(t)$ and $\sigma(t)$ is promoted a temporal function. Introducing the previous ansatz in the set of equations (4.28)

$$\begin{aligned}\dot{\eta}(R_0 + \eta^2 \partial_x R_0) &= \gamma \cos((\eta^2/2 - \nu)t + \sigma) - \mu R, \\ R_0 \dot{\sigma} &= -(\eta^2/2 - \nu)R - \gamma \sin((\eta^2/2 - \nu)t + \sigma).\end{aligned}\quad (4.25)$$

To obtain ordinary equations, we multiply both equations by R_0 and integrate them

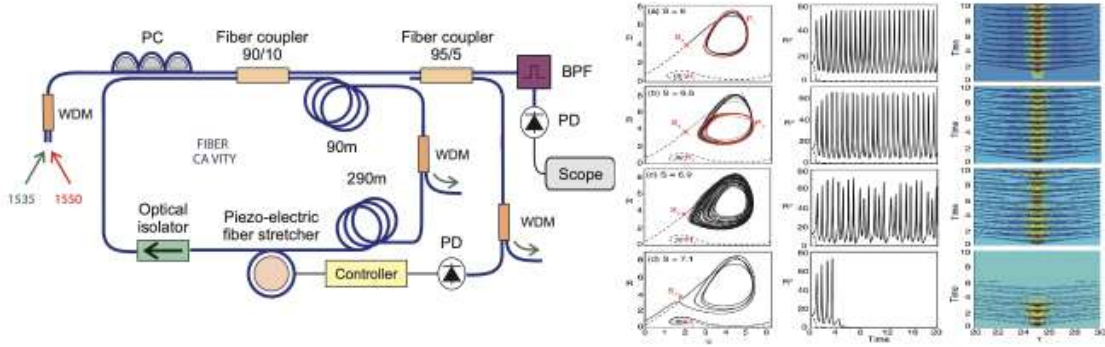


Figure 4.7: (a) Schematic representation of a fiber cavity. Experimental observation of cavity soliton.

into all space.

$$\begin{aligned} \dot{\eta} (\langle R_0^2 \rangle + \eta \langle R_0 \partial_x R_0 \rangle) &= \gamma \cos((\eta^2/2 - \nu)t + \sigma) \langle R_0 \rangle - \mu \eta \langle R_0^2 \rangle, \\ \langle R_0^2 \rangle \dot{\sigma} &= -(\eta^2/2 - \nu) \langle R_0^2 \rangle - \gamma \langle R_0 \rangle \sin((\eta^2/2 - \nu)t + \sigma). \end{aligned} \quad (4.26)$$

After straightforward calculations, one gets

$$\begin{aligned} \langle R_0 \rangle &= \frac{4\pi}{\eta^2}, \\ \langle R_0^2 \rangle &= \frac{16}{\eta^2}, \\ \langle R_0 \partial_x R_0 \rangle &= 0. \end{aligned} \quad (4.27)$$

Hence, we obtain

$$\begin{aligned} \dot{\eta} &= \frac{\gamma \pi \cos((\eta^2/2 - \nu)t + \sigma)}{4} - \mu \eta, \\ \dot{\sigma} &= -(\eta^2/2 - \nu) - \frac{\gamma \pi \sin((\eta^2/2 - \nu)t + \sigma)}{4}. \end{aligned} \quad (4.28)$$

Assuming $\sigma = (\eta^2/2 - \nu)t$. Namely, we consider that the solution is not oscillatory. Therefore, the correct ansatz should be

$$A = 2\eta \operatorname{sech} \left[\frac{\eta^2(x - x_0)}{2} \right], \quad (4.29)$$

where $\eta = \gamma\pi/4\mu$. The localized solution to the same as the parametric case is a balance between the injection and dissipation of energy.

Similar equations but that give a more adequate account of the dynamics are obtained through the use of the inverse scattering technique [119, 125, 153].

Driven Kerr cavities with a high Fresnel number—assuming that the cavity is much shorter than the diffraction and the nonlinearity spatial scales—is described in the mean field limit by the the driven damped nonlinear Schrödinger equation (4.15) [145]. This equation has been extended to model both fiber cavities [112] and optical frequency comb generation [44], in which the diffraction is replaced by dispersion. Temporal cavity solitons in one-dimensional Kerr media in was observed [136, 137]. Figure 4.7 shows a fiber cavity soliton.

Chapter 5

Structures located between homogeneous states

In the previous chapter we have found the existence of localized structure in the case of parametric and forced systems. Where the mechanism of appearance of these solutions is saddle-node and the mechanism of disappearance is the loss of the state that supports this solution. In order to establish the generic mechanisms of structures located in systems out of equilibrium, in this chapter we will establish the ingredients and mechanisms of localized structures in dissipative systems.

5.1 Bistable model

Intuitively one hopes to find localized solutions in systems that exhibit bistability or coexistence, that is, systems that exhibit coexistence of two stable states. In this section we will present various bistable physical systems with homogeneous states.

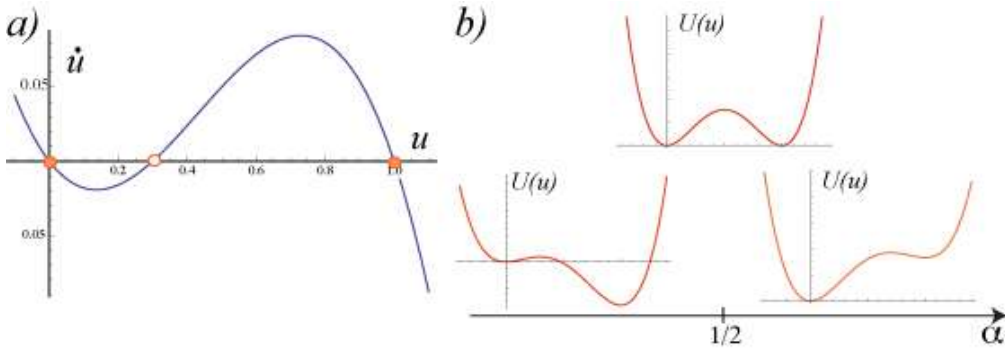


Figure 5.1: Nagumo Model a) representation of dynamics and equilibria. b) Energy as a function of the adversity parameter.

5.1.1 Population dynamics

A simple example that presents bistability is the Nagumo model [166], which has the form

$$\partial_t u = u(u-1)(\alpha-u) + \partial_{xx} u, \quad (5.1)$$

The scalar field $u(x, t)$ accounts for the density of a given population in a position x and time t . This population is characterized by the fact that the non-population state, $u = 0$, is a stable equilibrium that must overcome a nucleation barrier to generate the population equilibrium. That is, the previous model Eq. (5.1) takes as input the twin features of interaction at a distance and *the Allee effect* [5, 6, 169]. The latter means that the reaction term or nonlinearity in our system is such that the population suffers extinction if it starts out at sufficiently low levels of population density, that its growth overwhelms this tendency to extinction if the density exceeds certain levels, and that at sufficiently high levels a saturation effect sets in counteracting a Malthusian explosion (exponential growth). Note that $0 \leq \alpha \leq 1$ accounts for adversity. Namely, it controls the relative stability of the different equilibria $u = 1$ and $u = 0$, while α is closer to a state, it is then less stable. The two states are equally stable at $\alpha \equiv \alpha_M = 1/2$, which corresponds to Maxwell's point [102]. The previous model can be rewritten as follows

$$\partial_t u = -\frac{\partial U}{\partial u} + \partial_{xx} u, \quad (5.2)$$

where

$$U(u) = \frac{u^4}{4} - \frac{(1 + \alpha)u^3}{3} + \frac{\alpha u^2}{2}.$$

Figure 5.1 shows the potential as a function of the adversity parameter. It is important to note that the dynamics of model (5.1) is variational, that is,

$$\partial_t u = -\frac{\partial \mathcal{F}}{\partial u} \quad (5.3)$$

where

$$\mathcal{F} = \int \left[U(u) + \frac{(\partial_x u)^2}{2} \right] dx. \quad (5.4)$$

Then the dynamics of the Nagumo equation (5.1) is characterized by minimizing \mathcal{F} , since

$$\frac{d\mathcal{F}}{dt} = \int dx \frac{\partial \mathcal{F}}{\partial u} \frac{\partial u}{\partial t} = - \int dx \left(\frac{\partial \mathcal{F}}{\partial u} \right)^2. \quad (5.5)$$

Then the minima of \mathcal{F} account for the equilibria.

5.1.2 Nematic-isotropic transition

The nematic-isotropic transition is a classic problem of the theory of liquid crystals, in which the nematic phase is characterized by the rod like molecules are oriented locally

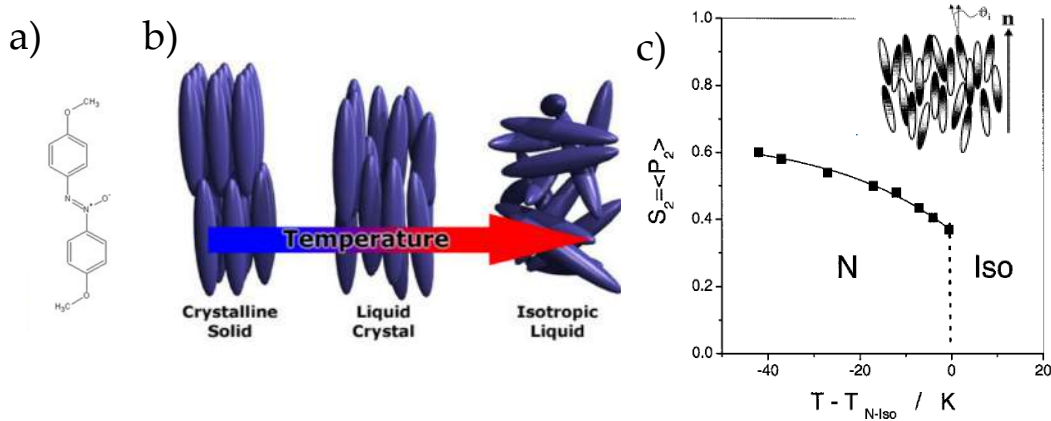


Figure 5.2: Liquid Crystals state of matter. a) Typical molecule of liquid crystal with rod like structures. b) Schematic representation of different phases of rod like molecules as function of temperature. c) Bifurcation diagram of a liquid crystal transition.

in one direction (orientational order), unlike the isotropic liquid phase which is characterized by the molecules are locally disordered [202, 43, 80]. Figure 5.2 shows a typical structure of liquid crystal molecules containing several coupled cycles benzenes. The interaction between molecules (electric and magnetic) and temperature allow the formation of different matter phases, such as: *crystalline solid*, *liquid crystal* and *isotropic liquid*. Figure 5.2b schematically illustrates these phases. Therefore, as a function of temperature T one expects to observe this transition, that is, there is a critical temperature T_c at which one observes the emergence of a phase on the other. T_c typically ranges from a few to hundreds celsius. Due to the molecules have a preferred direction but not a sense, this transition is characterized by a second rank tensor [202, 43, 80]. This tensor is a symmetric matrix with zero trace, characterized by a single scalar parameter

$$S(\vec{r}, t) = \frac{3}{2} \langle \cos^2(\theta) \rangle - \frac{1}{2}, \quad (5.6)$$

which is an order parameter¹ that accounts for the alignment of the molecules and θ is an angle with respect to a direction must be oriented the molecules (cf. Fig. 5.2). Then, when S is small (order one) accounts for the isotropic liquid (nematic) phase. The dynamic of the order parameter is characterized by the free energy (Landau-de Gennes theory) [202, 43, 79, 80]

$$\mathcal{F}[S, \nabla S] = \frac{A}{2} S^2 - \frac{B}{2} S^3 + \frac{1}{2} S^4 + \frac{(\nabla S)^2}{2}, \quad (5.7)$$

where $\{A, B\}$ are phenomenological positive parameters. It is worthy to note that due to S accounts for an orientation, the free energy \mathcal{F} does not depend linearly in S [79, 80]. Usually A parameter is proportional to difference of the temperature with the critical one ($A \propto T - T_c$) [202, 43, 80], this is the bifurcation parameter.

The temporal evolution of S is characterized by the minimization of the free energy, that is,

$$\frac{\partial S}{\partial t} = -\frac{\delta \mathcal{F}}{\delta S} = -AS + BS^2 - S^3 + \nabla^2 S. \quad (5.8)$$

¹An order parameter is the simplest variable characterizing the dynamics of a bifurcation[134].

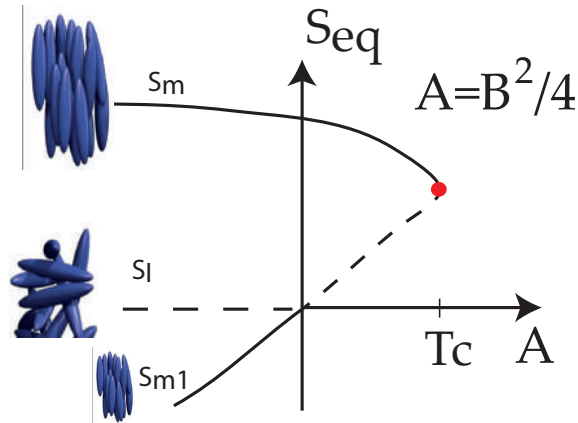


Figure 5.3: Bifurcation diagram of nematic isotropic transition described by model (5.8). The A parameter accounts for temperature. T_c is the critical temperature from which the system exhibits coexistence between the nematic (S_m and S_{m1}) and isotropic liquid phase (S_I).

From the standpoint of dynamic system, this model describes an extended transcritical bifurcation [74]. This model has the steady states $S = S_I = 0$ and $S \equiv S_M = (B \pm \sqrt{B^2 - 4A})/2$ that accounts, respectively, for the isotropic liquid and nematic phase. For large values of the bifurcation parameter ($A \gg 1$), the only supported state is the isotropic liquid phase, S_I . When the bifurcation parameter is diminished to zero ($A = 0$), the isotropic state becomes unstable by a discontinuous bifurcation (first order transition or subcritical bifurcation [114, 194]), that is, this bifurcation generates an abrupt change of equilibria. This bifurcation generates the emergence of nematic phase, S_M . This phase has a region of hysteresis (coexistence) with isotropic state between $A = 0$ to $A = B^2/4$. For negative A the stable state are nematic phases (S_m and S_{m1}). Moreover, for $A < 0$ the isotropic liquid phase is unstable. Figure 5.3 shows a bifurcation diagram of isotropic nematic transition described by model (5.8).

5.1.3 Ferromagnetic transition

Ferromagnetic materials are characterized by exhibiting a permanent magnetic (magnets). Typical materials that exhibit this property are cobalt, iron, and nickel. However,

when one increases the temperature these materials lose this magnetic property. When one decreases the temperature becomes another magnetic exactly at the same critical temperature, which is referred to as the Curie temperature, T_C [123]. From a microscopic point of view to sufficiently high temperatures the magnetic spins of the material are disordered. Figure 5.4 illustrates the ferromagnetic materials as function of temperature. For temperatures lower than the Curie temperature, the magnetic spins are arranged in one or another direction.

Following the spirit of Landau to describe this transition [196, 134], let us consider as an order parameter the magnetization $M(\vec{r}, t)$, which accounts for the density of magnetic spins or moments. When the magnetization is zero the system does not exhibit magnetism. Assuming the ferromagnetic transition is smooth and there is magnetic exchange with the first neighbors. In the Landau approach, the free energy that characterizes the ferromagnetic transition is [134]

$$F = \int \left(\epsilon \frac{M^2}{2} + \frac{M^4}{4} + \dots + \frac{[\partial_x M]^2}{2} \right) dx, \quad (5.9)$$

where ϵ is the bifurcation parameter that is proportional to $T - T_c$. The dynamics of

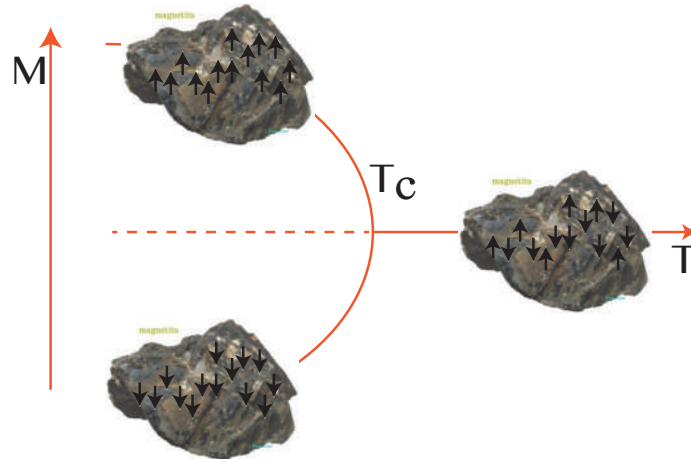


Figure 5.4: Schematic representation of ferromagnetic transition. T and M account for the temperature and magnetization, respectively.

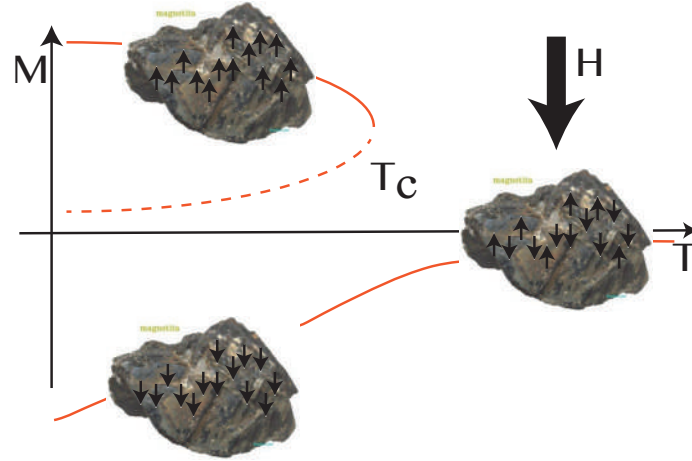


Figure 5.5: Schematic representation of ferromagnetic transition under the influence of an external magnetic field H .

magnetization is given by (dissipative ϕ^4 -model)

$$\partial_t M = -\frac{\delta F}{\delta M} = \epsilon M - M^3 + \partial_{xx} M. \quad (5.10)$$

For positive ϵ there is only one states ($M = 0$) and for ϵ negative, the system has three equilibria one unstable and two stables. Figure 5.4 shows the bifurcation diagram of this model, where the equilibria are $M = \{0, \pm\sqrt{\epsilon}\}$. In presence of external magnetic field the above scenario changes, the ferromagnetic transition becomes an imperfect transition as it is illustrated in Fig. 5.5. Indeed, the forced magnetic material is a magnet even over the curie temperature (cf. Fig. 5.5). The external magnetic field favors a magnetization on the other. Hence, the external magnetic field broke the symmetry between both magnetic equilibria. A simple term that broke this symmetry in the free energy is

$$F = \int \left(HM + \epsilon \frac{M^2}{2} + \frac{M^4}{4} + \dots + \frac{[\partial_x M]^2}{2} \right) dx, \quad (5.11)$$

likewise the dynamics of the magnetization reads

$$\partial_t M = H - \epsilon M - M^3 + \partial_{xx} M. \quad (5.12)$$

The bifurcation diagram of this model is depicted in Fig. 5.5. Due to this transition has coexistence between two stable domain, one expect to observe front propagation between this two asymmetric states.

5.2 Particle-type solutions between two-uniform states: wave called Front

All the physical models presented in the previous section are characterized by presenting coexistence between uniform solutions. Let us consider a simple one-dimensional reaction diffusion model of the form

$$\partial_t u = -\frac{\partial V}{\partial u} + \partial_{xx} u = -\frac{\delta F}{\delta u}, \quad (5.13)$$

with a bistable potential and Lyapunov function

$$F = \int \left(V(u) + \frac{[\partial_x u]^2}{2} \right) dx. \quad (5.14)$$

For the sake of simplicity, we can consider a bistable potential

$$V(u) = -\eta u - \epsilon u^2/2 + u^4/4. \quad (5.15)$$

In the upper panels of Fig. 5.6 is represented the potential for different value of η and positive ϵ . This system have two trivial equilibria represented by $\{\mathcal{A}, \mathcal{B}\}$, that is, in this region of parameters the system exhibits bistability. For small η , the equilibria has the form $\mathcal{A} = -\sqrt{\epsilon} + O(\eta)$ and $\mathcal{B} = \sqrt{\epsilon} + O(\eta)$.

Thus, the reaction diffusion equation reads

$$\partial_t u = \eta + \epsilon u - u^3 + \partial_{xx} u. \quad (5.16)$$

This model correspond to a simplified model of ferromagnetic transition. From the dynamical point of view this model correspond to an extended pitchfork bifurcation [74], where ϵ and η are the bifurcation parameter and parameter that controls the

5.2. PARTICLE-TYPE SOLUTIONS BETWEEN TWO-UNIFORM STATES: WAVE CALLED FROM

relative stability between equilibria. This bifurcation accounts for the nascent of bistability [197]. In the context of catastrophe theory the previous model corresponds to an extended cusp catastrophe [15, 101].

Numerical simulations of the above model by small η and positive ϵ show front propagation between the equilibria. Figure 5.6 shows the profile and spatiotemporal evolution of front solutions of simple bistable model (5.16). Considering a propagative solution $u(x - vt)$, we have the following Newton type equation

$$-v\partial_z u = -\frac{\partial V}{\partial u} + \partial_{zz}u, \quad (5.17)$$

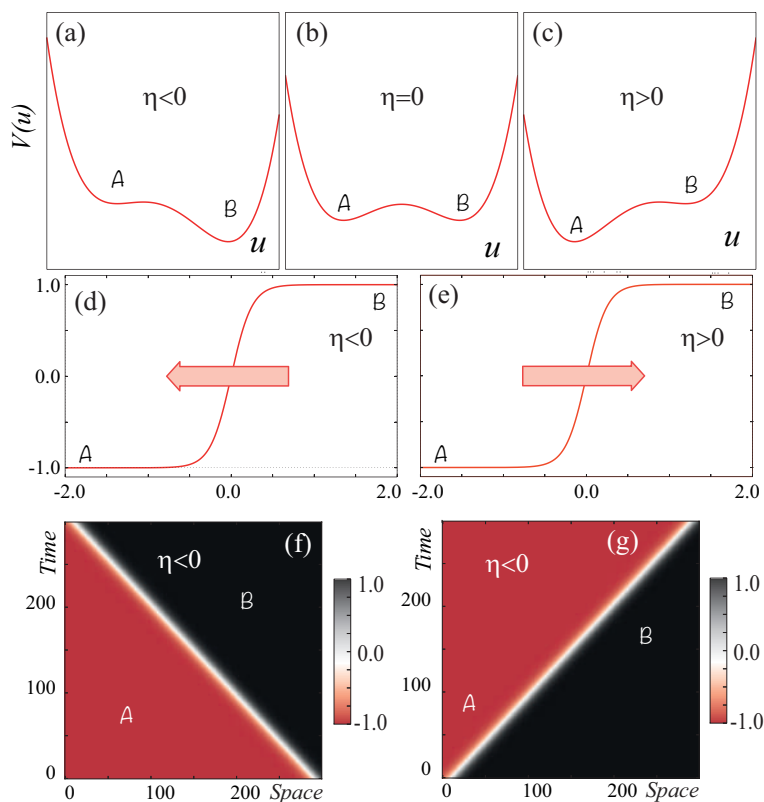


Figure 5.6: Front propagation in bistable variational model Eq. (5.16) with positive ϵ . The upper panels represent the potential, $V(u)$, for different values of η . The middle and lower panels illustrate the front profile and their respective spatiotemporal evolution [9].

where $z = x - vt$ is the co-mobile coordinate. Thus the above equation can rewrite as

$$\partial_{zz}u = \frac{\partial V}{\partial u} - v\partial_z u = -\frac{\partial W}{\partial u} - v\partial_z u. \quad (5.18)$$

This equation correspond to a Newton type equation with a potential $W(u) = -V(u)$, that is, the potential is inverted. Figure 5.7 depicts the respective potentials V and W . Hence for this Newton type equation, the front solution corresponds to a heteroclinic curve between the equilibria. Then, starting from \mathcal{B} state, there is an only one damping coefficient v_c , for which the system presented an heteroclinic. For larger speeds ($v > v_c$) the trajectory from \mathcal{B} ends at the unstable equilibrium, which corresponds to a local minimum of effective potential W . Figure 5.7 shows this equilibrium that is represented by \mathcal{C} . Contrary to lower speeds ($v < v_c$), the trajectory diverges to infinity. Therefore, normal fronts only have a single speed of propagation ($v = v_c$). Which it is a completely different features in compare to fronts propagation into unstable state.

In the case of considering a front connecting \mathcal{A} with \mathcal{B} , it is important to note that the state \mathcal{A} corresponds to a local minimum, then the speed is negative to generate this trajectory, i.e., this term is now an injection energy ($v < 0$). From Newton type equation, one can infer that when two states have the same energy, the front solution is motionless. The possibility of parameter space having a motionless front is known in the literature as Maxwell point [102]. Thus the mechanism of propagation of fronts between stable states for variational systems is the energy difference between these

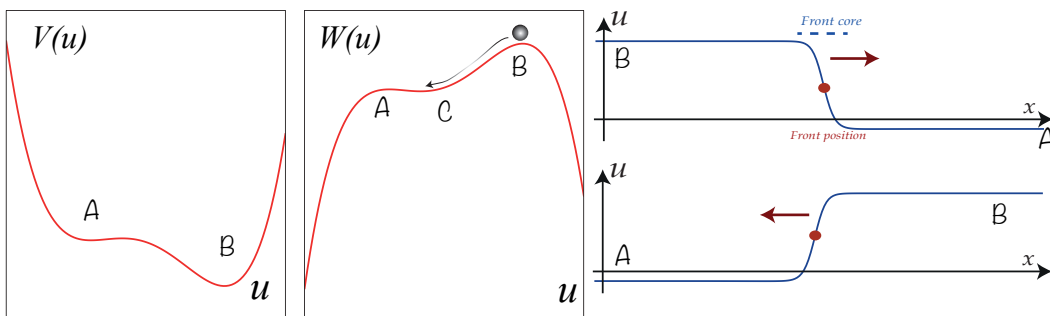


Figure 5.7: Bistable potential. Left and central panel correspond to original and effective potential in the Newton type equation. Right panels account for the normal front solutions.

5.2. PARTICLE-TYPE SOLUTIONS BETWEEN TWO-UNIFORM STATES: WAVE CALLED FROM

states. Namely, when the front spreads the free energy F decreases.

To determine analytically the front speed, one can multiply Eq. (5.17) by $\partial_z u$ and integrated in the entire domain, one gets

$$\begin{aligned}
 -v \int dz (\partial_z u)^2 &= - \int dz \frac{\partial V}{\partial u} \partial_z u + \int dz \partial_{zz} u \partial_z u, \\
 &= - \int dz \frac{\partial V}{\partial z} + \int dz \partial_z \left(\frac{[\partial_z u]^2}{2} \right), \\
 &= -\Delta V + \frac{[\partial_z u]^2}{2} \Big|_{-\infty}^{\infty},
 \end{aligned} \tag{5.19}$$

where $\Delta V = V(z = -\infty) - V(z = \infty) = V(\mathcal{A}) - V(\mathcal{B})$. Using the fact that the front in infinity converges to the steady state, thus $\partial_z u|_{\pm\infty} = 0$. Finally one obtains the following expression for the front speed [174]

$$v = \frac{\Delta V}{\int dz (\partial_z u)^2}. \tag{5.20}$$

From the above formula, one can conclude that the front speed is proportional to the energy difference. However, the above expression is not a explicit formula for the front speed, since the profile of $u(z)$ depends on v . Note that the above result is valid for any variational system of the form (5.13).

Front propagation close to Maxwell's point

Let us consider $\eta = 0$, Maxwell's point, the bistable model (5.16) has a motionless front solution of the form

$$u(x, t) = \sqrt{\epsilon} \tanh \left(\frac{\sqrt{\epsilon}(x - x_0)}{2} \right), \tag{5.21}$$

where x_0 stands for the front position. Considered the term proportional to η as a perturbative one, we can consider the following ansatz

$$u(x, t) = \sqrt{\epsilon} \tanh \left(\frac{\sqrt{\epsilon}(x - x_0(t))}{2} \right) + w(x, x_0), \tag{5.22}$$

where the front position is promoted to a temporal function and w is a small correction function. We assume that the temporal variation of front position and w are the order

of perturbation ($\dot{x}_0 \sim w \sim \eta$). Introducing the above ansatz in Eq. (5.16), linearizing in w , and after straightforward calculations we obtain the following solvability condition

$$\dot{x}_0 = \frac{\eta \int dz \partial_z u}{\int dz (\partial_z u)^2} = \frac{3\sqrt{2}}{2\epsilon} \eta. \quad (5.23)$$

Then the front speed is proportional to η .

5.3 Front propagation at the Fredericksz transition

As we have already mentioned in Chapter 5.1.2, the liquid crystals are characterized by having a locally orientational order. This soft material must be sustained in a container. The container walls interact with the liquid crystal molecules in the walls inducing certain orientations. If molecules are oriented parallel or orthogonal to the walls is referred to as planar or homeotropic anchoring [43, ?]. Figure 5.8 shows a nematic liquid crystal sample with planar anchoring. As a result of anchoring all molecules are oriented in the same direction, because anchoring molecules apply a torque over the other molecules. Through the application of an external field one can induce an extra torque [43, ?]. In particular, if the molecules have positive dielectric constant, the application of a voltage orthogonal to the walls can induce a torque such that molecules like to be parallel to electric field. Competition between the torque induced by the anchored molecules (elasticity) and the torque induced by the external field can induce an instability for the molecular orientational order. This instability is well-known as *the Fredericksz transition* [43, ?]. Indeed, there is a critical value of the intensity of the electric field, $|\vec{E}_c|$, for which the molecules start to rotate. Figure 5.8 depicts the the Fredericksz transition.

Experimental observations of Fredericksz transition to nematic liquid crystal samples show that this instability is supercritical [?]. To describe the dynamics of a nematic liquid crystal thin film must be introduced as order parameter average angle molecules $\theta(r_\perp, t)$ in the thickness direction. In the inset of Fig. 5.8 this angle is illustrated. Based on the theory of bifurcations close to the Fredericksz transition, we can introduce the

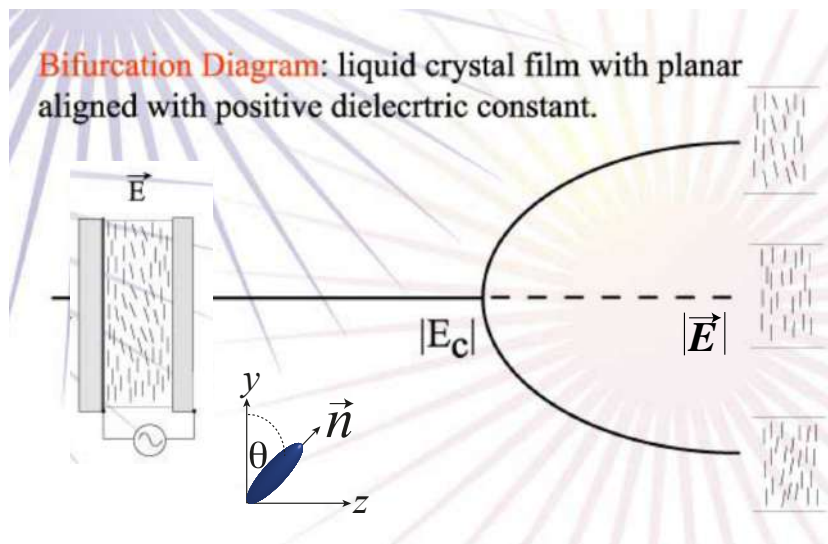


Figure 5.8: Schematic representation of the Freedericksz transition for a nematic liquid crystal with planar anchoring.

following model describing this transition

$$\dot{\theta} = \alpha(|\vec{E}|^2 - K_3)\theta - \beta\theta^3 + \kappa\nabla_{\perp}^2\theta, \quad (5.24)$$

where $\{\alpha, \beta\}$ are adequate dimensional parameters, κ accounts for diffusion length, and ∇_{\perp}^2 accounts for the Laplacian in transversal coordinates. Below the transition point ($|\vec{E}|^2 < K_3$), the only stable equilibrium corresponds to the molecules parallel to the walls, $\theta = 0$. Above the transition point ($|\vec{E}|^2 \geq K_3$), the system exhibits two homogeneous configurations as equilibrium, $\theta = \pm\sqrt{|\vec{E}|^2 - K_3}$. Energetically these two configurations are equivalent. That is, this transition corresponds to a spontaneous breaking of the reflection symmetry. For an arbitrary initial condition this system exhibits different domains separated by defects. This front solution are denominated Ising wall because connect symmetric states. Moreover, this solution due to connect energetically equivalent states are denominated *kink solutions* [157, 200]. Figure 5.9 shows the interface dynamics close to Fréedericksz transition. To understand the rich dynamics of Ising walls, in the next section we will study the interaction of walls.

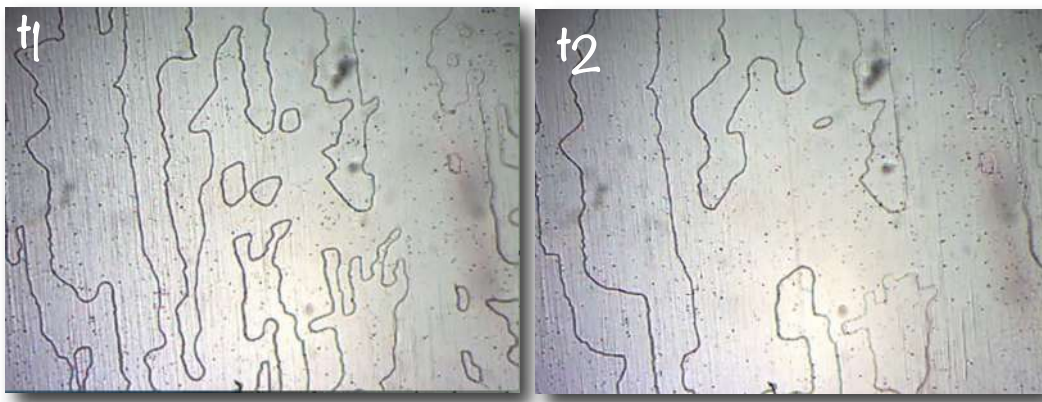


Figure 5.9: Domain walls above the Fréedericksz transition for successive instant ($t_1 > t_2$), courtesy LAFER.

5.4 Kink interaction

To figure out the rich dynamics of interface between Ising nematic wall. Let us consider the kink dynamics in one-dimension described by

$$\partial_t u = \epsilon u - u^3 + \partial_{xx} u, \quad (5.25)$$

where $u(x, t) \equiv \sqrt{\beta}\theta(x, t)$ and $x = r_\perp/\sqrt{\kappa}$ are the normalized order parameter and spatial coordinate. $\epsilon \equiv \alpha(|\vec{E}|^2 - K_3)$ is the bifurcation parameter. As we have mention this model has kink and anti-kink solutions (cf. formula 5.21). In the next session, based on the pioneering work of Kawasaki and Ohta [120], we will characterize the kinks interaction.

5.4.1 Kinematic law of a pair kinks

Let $\{u_-, u_+\}$ kink and anti-kink solutions of model Eq. (5.25), respectively. The kink solutions are characterized by a continuous parameter the kink position² and fixed parameter the front width. Note that the translation invariance generates a Lie group

²This position corresponds to the spatial location of the front that presents maximum spatial variation. In the particular case of kink solutions of Eq. (5.25), this position corresponds to the root of the kink.

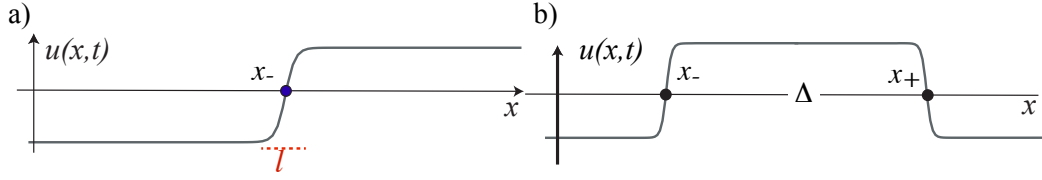


Figure 5.10: Schematic representation of kink solutions. a) Kink solution obtained from numerical solutions of Eq. (5.25). x_- and l stand for the kink position and width. b) kink and anti-kink solution, $\{x_-, x_+\}$ are the kink positions and Δ is the distance between kinks.

with respect to the translation parameter [178]. Figure 5.10a displays the front position and width. Consider a pair of kinks sufficiently separated as shown in Figure 5.10b. To describe this solution we consider the ansatz

$$u(x, t) = u_k[x - x_-(t)] + u_{Ak}[x - x_+(t)] - \sqrt{\epsilon} + w(x, x_-, x_+), \quad (5.26)$$

where $\{x_-, x_+\}$ are the kink positions that are promoted temporal function and w is a small correction function. The third term of the above expression is necessary for that the kink-antikink solution in infinite tends to $-\sqrt{\epsilon}$. Introducing the above ansatz in Eq. (5.25), and linearized in w after straightforward calculations we obtain

$$\begin{aligned} \partial_t u &= -\dot{x}_- \partial_z u_k(z \equiv x - x_-) - \dot{x}_+ \partial_z u_{Ak}(z \equiv x - x_+) \\ &= (\epsilon - (u_k + u_{Ak} - \sqrt{\epsilon})^2 + \partial_{xx}) w + \epsilon(u_k + u_{Ak} - \sqrt{\epsilon}) \\ &\quad - (u_k + u_{Ak} - \sqrt{\epsilon})^3 + \partial_{xx} u_k + \partial_{xx} u_{Ak}, \end{aligned} \quad (5.27)$$

rewriting the above expression using the fact that $\epsilon u_k - u_k^3 + \partial_{xx} u_k = 0$ and $\epsilon u_{Ak} - u_{Ak}^3 + \partial_{xx} u_{Ak} = 0$, one obtains

$$\begin{aligned} \mathcal{L}w &\equiv -(\epsilon - 3(u_k + u_{Ak} - \sqrt{\epsilon})^2 + \partial_{xx}) w = \dot{x}_- \partial_z u_k + \dot{x}_+ \partial_z u_{Ak} \\ &\quad - 3u_k^2(u_{Ak} - \sqrt{\epsilon}) - 3u_k(u_{Ak} - \sqrt{\epsilon})^2 + 3u_{Ak}\sqrt{\epsilon}(u_{Ak} - \sqrt{\epsilon}). \end{aligned} \quad (5.28)$$

To solve the above linear equation, we must to introduce the inner product

$$\langle f|g \rangle = \int_{-\infty}^{\infty} f(x)g(x)dx, \quad (5.29)$$

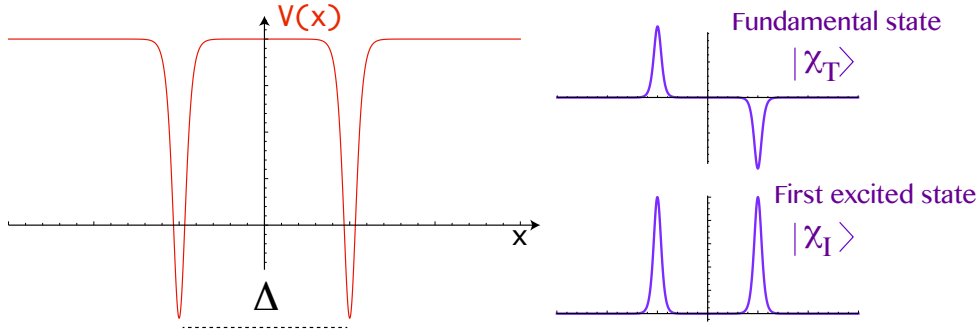


Figure 5.11: Effective bistable potential of kink interaction. Δ accounts for the distance between the minima. Insets account for the fundamental and first excited states.

then \mathcal{L} is a self adjoint operator, $\mathcal{L}^\dagger = -(\epsilon - 3(u_k + u_{Ak} - \sqrt{\epsilon})^2 + \partial_{xx})$. Notice that this operator is Hamiltonian type, i.e., $\mathcal{L}^\dagger = -\partial_{xx} + V(x)$, where the associated potential is defined by $V(x) \equiv -\epsilon + 3[u_k(x) + u_{Ak}(x) - \sqrt{\epsilon}]^2$, which corresponds a bistable potential. Figure 5.11 shows the bistable potential of the kink interaction. This potential has a fundamental mode related to translations of the kinks. In the case that the distance between the kinks is large enough ($\Delta \ll \sqrt{\epsilon}$), the fundamental mode as results of translation invariance can be approach by

$$|\chi_T\rangle = \partial_x u_k + \partial_x u_{Ak} + O(e^{-\sqrt{2\epsilon}\Delta}), \quad (5.30)$$

This mode is an element of kernel of \mathcal{L}^\dagger , i.e. $\mathcal{L}^\dagger |\chi_T\rangle = 0$. Moreover, $\mathcal{L}^\dagger [\partial_x u_k + \partial_x u_{Ak}] = O(e^{-\sqrt{2\epsilon}\Delta})$. Another important mode is the first excited state $|\chi_I\rangle$, which is this related to the mode of interaction of kinks. This mode can be write

$$|\chi_I\rangle = \partial_x u_k - \partial_x u_{Ak} + O(e^{-\sqrt{2\epsilon}\Delta}), \quad (5.31)$$

Note that

$$\mathcal{L}^\dagger |\chi_I\rangle = O(e^{-\sqrt{2\epsilon}\Delta}). \quad (5.32)$$

Therefore, for long separated kinks, $\Delta \ll \sqrt{\epsilon}$, the functions $\{\partial_x u_k + \partial_x u_{Ak}, \partial_x u_k - \partial_x u_{Ak}\}$ are pseudo eigenfunctions of \mathcal{L}^\dagger , that is, these eigenfunctions have eigenvalues with exponential small values. In a similar manner of two-body problem, we introduce a

change of variables to the central position $\delta(t)$ ³ and the distance between kinks $\Delta(t)$. Introducing the change of variable

$$\begin{aligned}\delta(t) &\equiv \frac{x_-(t) + x_+(t)}{2}, \\ \Delta(t) &\equiv x_-(t) - x_+(t).\end{aligned}\tag{5.33}$$

Analogously one obtains

$$\begin{aligned}x_-(t) &= \delta - \frac{\Delta}{2}, \\ x_+(t) &= \delta + \frac{\Delta}{2}.\end{aligned}\tag{5.34}$$

Introducing this change of variable in Eq. (5.28), this reads

$$\begin{aligned}\mathcal{L}w &= \dot{\delta}(\partial_z u_k + \partial_z u_{Ak}) - \dot{\Delta}(\partial_z u_k - \partial_z u_{Ak}) \\ &- 3u_k^2(u_{Ak} - \sqrt{\epsilon}) - 3u_k(u_{Ak} - \sqrt{\epsilon})^2 + 3u_{Ak}\sqrt{\epsilon}(u_{Ak} - \sqrt{\epsilon}).\end{aligned}\tag{5.35}$$

To solve the above linear equation we must to impose the solvability condition, that is, the right hand side of above equation is orthogonal to the pseudo eigenfunctions $\{|\chi_T\rangle, |\chi_I\rangle\}$. Imposing the solvability conditions with respect to translation mode, we obtain

$$\dot{\delta}\langle\chi_T|(\partial_z u_k + \partial_z u_{Ak})\rangle = \langle\chi_T|3u_k^2(u_{Ak} - \sqrt{\epsilon}) - 3u_k(u_{Ak} - \sqrt{\epsilon})^2 + 3u_{Ak}\sqrt{\epsilon}(u_{Ak} - \sqrt{\epsilon})\rangle.\tag{5.36}$$

The above equations can rewrite

$$\begin{aligned}\dot{\delta}|\chi_T|^2 &= \langle\partial_z u_k|3u_k^2(u_{Ak} - \sqrt{\epsilon}) - 3u_k(u_{Ak} - \sqrt{\epsilon})^2 + 3u_{Ak}\sqrt{\epsilon}(u_{Ak} - \sqrt{\epsilon})\rangle \\ &+ \langle\partial_z u_{Ak}|3u_k^2(u_{Ak} - \sqrt{\epsilon}) - 3u_k(u_{Ak} - \sqrt{\epsilon})^2 + 3u_{Ak}\sqrt{\epsilon}(u_{Ak} - \sqrt{\epsilon})\rangle.\end{aligned}\tag{5.37}$$

By symmetry arguments

$$\begin{aligned}3u_k^2(u_{Ak} - \sqrt{\epsilon}) - 3u_k(u_{Ak} - \sqrt{\epsilon})^2 + 3u_{Ak}\sqrt{\epsilon}(u_{Ak} - \sqrt{\epsilon}) &= \\ 3u_{Ak}^2(u_k - \sqrt{\epsilon}) - 3u_{Ak}(u_k - \sqrt{\epsilon})^2 + 3u_k\sqrt{\epsilon}(u_k - \sqrt{\epsilon}).\end{aligned}\tag{5.38}$$

³Which corresponds to the equivalent mass center.

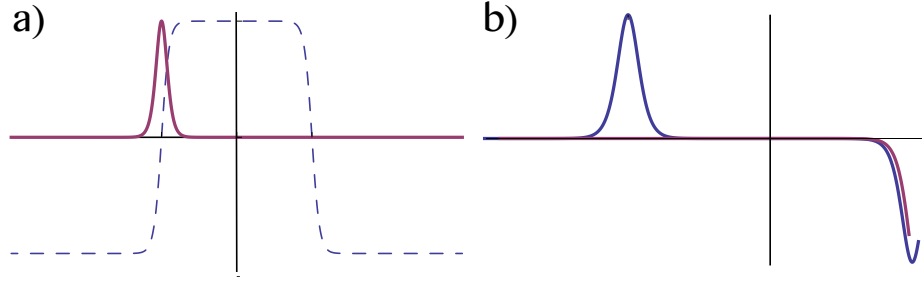


Figure 5.12: Kink solution. a) Spatial variation of the kink solution, $\partial_x u_k$. b) Asymptotic behavior of $u_{Ak} - \sqrt{\epsilon}$ around kink position.

Hence, the dynamic of central position is

$$\begin{aligned} \dot{\delta} ||\chi_T||^2 &= \langle \partial_z u_k | 3u_k^2(u_{Ak} - \sqrt{\epsilon}) - 3u_k(u_{Ak} - \sqrt{\epsilon})^2 + 3u_{Ak}\sqrt{\epsilon}(u_{Ak} - \sqrt{\epsilon}) \rangle \\ &+ \langle \partial_z u_{Ak} | 3u_{Ak}^2(u_k - \sqrt{\epsilon}) - 3u_{Ak}(u_k - \sqrt{\epsilon})^2 + 3u_k\sqrt{\epsilon}(u_k - \sqrt{\epsilon}) \rangle. \end{aligned} \quad (5.39)$$

The spatial variation of the kink solution u_k is characterized by being centered in the kink position, i.e. it is exponentially small almost everywhere except in the region close to the kink core. Figure 5.12 shows the function $\partial_x u_k$. Then the first term on the right side is an integral to be evaluated around x_- . The anti-kink solution around x_- minus $\sqrt{\epsilon}$ when both kinks are enough separated has the form

$$(u_{Ak}(x \rightarrow -\infty) - \sqrt{\epsilon}) \longrightarrow -2\sqrt{\epsilon}e^{-2\sqrt{\epsilon/2}(x-\delta-\Delta/2)}. \quad (5.40)$$

This function around the kink position decays exponentially and $u_{Ak} \approx \sqrt{\epsilon} - 2e^{-2\sqrt{\epsilon/2}(x-\delta-\Delta/2)}$.

Thus, the first term on the right side can be approximate by

$$\langle \partial_z u_k | u_k^2(u_{Ak} - \sqrt{\epsilon}) - u_k(u_{Ak} - \sqrt{\epsilon})^2 + u_{Ak}\sqrt{\epsilon}(u_{Ak} - \sqrt{\epsilon}) \rangle \approx \langle \partial_z u_k | u_{Ak}\sqrt{\epsilon}(u_{Ak} - \sqrt{\epsilon}) \rangle. \quad (5.41)$$

This last integral can be approximate

$$\langle \partial_z u_k | u_{Ak}\sqrt{\epsilon}(u_{Ak} - \sqrt{\epsilon}) \rangle \approx -2\epsilon \int_{-\infty}^{\infty} dx \partial_z u_k \left(x - \delta + \frac{\Delta}{2} \right) e^{-2\sqrt{\epsilon/2}(x-\delta-\Delta/2)} H \left(-x + \delta + \frac{\Delta}{2} \right), \quad (5.42)$$

where $H(x)$ is the Heaviside step function [23]. The introduction of the H function is to describe adequately the behavior of the function $u_{Ak}(x) - \sqrt{\epsilon}$ in infinite. Changing

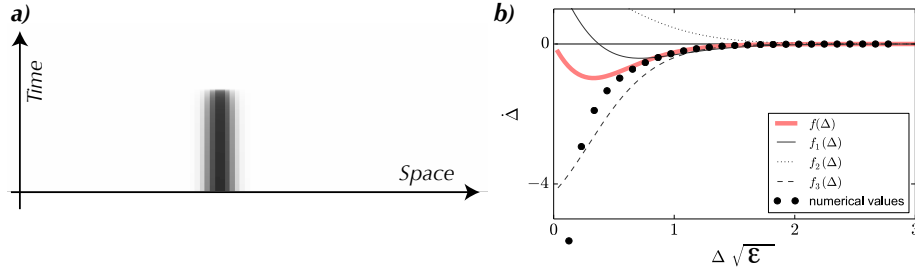


Figure 5.13: Kink interaction. a) Spatiotemporal evolution of a kinks pair. b) Numerical comparison of the kink interaction and numerical simulation. Points are obtained numerically by considering two close kink and anti-kink solution, then numerically the system evolves during a brief moment of time, and finally the temporal variation of the kink position is calculated, where curves are defined by $f(\Delta) \equiv \langle \chi_I | 3u_k^2(u_{Ak} - \sqrt{\epsilon}) + 3u_k(u_{Ak} - \sqrt{\epsilon})^2 + 3u_{Ak}\sqrt{\epsilon}(u_{Ak} - \sqrt{\epsilon}) \rangle$, $f_1(\Delta) \equiv \langle \chi_I | 3u_{Ak}\sqrt{\epsilon}(u_{Ak} - \sqrt{\epsilon}) \rangle$, $f_2(\Delta) \equiv \langle \chi_I | 3u_k^2(u_{Ak} - \sqrt{\epsilon}) \rangle$, $f_3(\Delta) \equiv \langle \chi_I | 3u_k(u_{Ak} - \sqrt{\epsilon})^2 \rangle$ [69].

the variable of integration $z = x - \delta + \Delta/2$, this integral reads

$$\langle \partial_z u_k | u_{Ak} \sqrt{\epsilon} (u_{Ak} - \sqrt{\epsilon}) \rangle \approx -\frac{a}{2} e^{-2\sqrt{\epsilon}/2\Delta}, \quad (5.43)$$

where $a \equiv 4\epsilon \int \partial_z u_k(z) e^{-\sqrt{\epsilon}z} H(-z + \Delta)$. Hence, one obtains

$$\langle \partial_z u_k | u_k^2(u_{Ak} - \sqrt{\epsilon}) - u_k(u_{Ak} - \sqrt{\epsilon})^2 + u_{Ak}\sqrt{\epsilon}(u_{Ak} - \sqrt{\epsilon}) \rangle \approx -\frac{a}{2} e^{-2\sqrt{\epsilon}/2\Delta}. \quad (5.44)$$

Analogously to previous analysis for the second term on the right side of Eq. (5.39), one can perform the same type of approach⁴ and gets

$$\langle \partial_z u_{Ak} | 3u_{Ak}^2(u_k - \sqrt{\epsilon}) - 3u_{Ak}(u_k - \sqrt{\epsilon})^2 + 3u_k\sqrt{\epsilon}(u_k - \sqrt{\epsilon}) \rangle \approx \frac{a}{2} e^{-2\sqrt{\epsilon}/2\Delta}. \quad (5.45)$$

Therefore, the dynamics of the central positions of the kinks is $\dot{\delta} = 0$. From this result we can infer that the kinks dynamics can be characterized by either attract or repel the kinks symmetrically. The above dynamic one also can be understood as a consequence of the reflection invariance of Eq. (5.25)

⁴The difference that the spatial variation of the anti-kink compared with the kink is the opposite sign $\int \partial_z u_k(z) = -\int \partial_z u_{Ak}(z)$.

Imposing the solvability conditions with respect to interaction mode $|\chi_I\rangle$, after straightforward calculation we obtain

$$\begin{aligned} \dot{\Delta} \|\chi_I\|^2 &= \langle \partial_z u_k | 3u_k^2(u_{Ak} - \sqrt{\epsilon}) - 3u_k(u_{Ak} - \sqrt{\epsilon})^2 + 3u_{Ak}\sqrt{\epsilon}(u_{Ak} - \sqrt{\epsilon}) \rangle \\ &- \langle \partial_z u_{Ak} | 3u_{Ak}^2(u_k - \sqrt{\epsilon}) - 3u_{Ak}(u_k - \sqrt{\epsilon})^2 + 3u_k\sqrt{\epsilon}(u_k - \sqrt{\epsilon}) \rangle. \end{aligned} \quad (5.46)$$

Using the results obtained in formulas (5.44,5.45), the dynamics for the distance between kinks Δ satisfies (The kinematic law of kinks) [120]

$$\dot{\Delta} \approx -be^{-\sqrt{2\epsilon}\Delta}, \quad (5.47)$$

with $b \equiv a/\|\chi_I\|^2 = 3a/2\epsilon^{3/2} > 0$. Therefore, the kink interaction is characterized by being attractive and decreased exponentially with the distance between kinks. The system then seeks to find its overall energy minimum through the kink attract and reach the homogeneous state. Figure 5.13 shows the spatiotemporal evolution of a kinks pair and also the comparison of the different terms of the interaction with numerical simulations. These results show an appropriate agreement even for distances of the order of the kink core, where the other terms of the interaction have been take into account [69].

5.4.2 Interaction of a gas of kinks: coarsegraning

Numerical simulations of model Eq. (5.25) with noise before the transition exhibit fluctuations around the zero equilibrium. Crossing transition, the system presents the emergence of diverse walls. These domains are separated by several kinks that are interacting. Figure 5.14 illustrates the previous process. To account for these wall domains, we consider the following ansatz (multiple kinks solutions)

$$u(x, t) \approx \sum_n (-1)^n u_k(x - x_n(t)) - \sqrt{\epsilon}, \quad (5.48)$$

where x_n stands for the position n -kink. Using the pair interaction law, Eq. (5.47), between the kinks, we obtains (n -kink interaction law) [120]

$$\dot{x}_n = b \sum_{i < n} (-1)^i e^{-2\sqrt{\epsilon/2}|x_n - x_i|} - b \sum_{i > n} (-1)^i e^{-2\sqrt{\epsilon/2}|x_i - x_n|}. \quad (5.49)$$

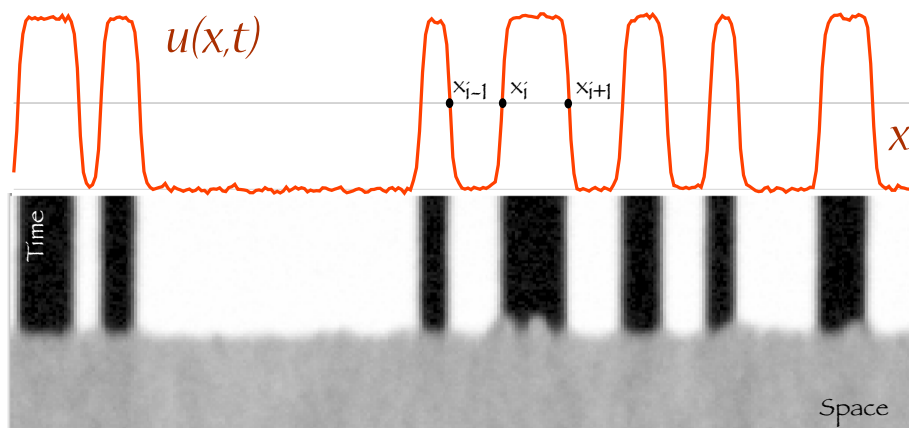


Figure 5.14: Spatiotemporal evolution of emergence of domains walls. Numerical simulation of model Eq. (5.25) with noise before and after transition. x_i accounts for the kink position.

Due to the n -kink interaction decays exponentially, we can approximate it by the interaction of first neighbors, that is,

$$\dot{x}_n \approx -be^{-2\sqrt{\epsilon/2}(x_{n+1}-x_n)} + be^{-2\sqrt{\epsilon/2}(x_n-x_{n-1})}. \quad (5.50)$$

Then the closest kinks attract the central kink with the aim of annihilating it. It is important to note that this type of force between kinks is weak and short-range, which makes it difficult to verify this type of interaction numerically.

An unexpected property of the interaction of a gas of kinks is that it is self-similar, that is, the interaction is simultaneously invariant to temporal and coordinate transformations [184, 30]. As a result of this type of symmetry one expects to find laws for the dynamics. A classic example of self-similarity is the Newton interaction that cause the Kepler's third law [184, 30]. Considering the transformation

$$\begin{aligned} (x_{n+1} - x_n) &\rightarrow (x_{n+1} - x_n + \lambda), \\ t &\rightarrow te^{\sqrt{2\epsilon}\lambda}, \end{aligned} \quad (5.51)$$

that corresponds to a temporal and spatial dilatation, the kink interaction Eq. (5.50) is invariant. This means that if one separates the distance between kinks in a λ distance is equivalent to delay time by a fact $e^{2\sqrt{\epsilon/2}\lambda}$.

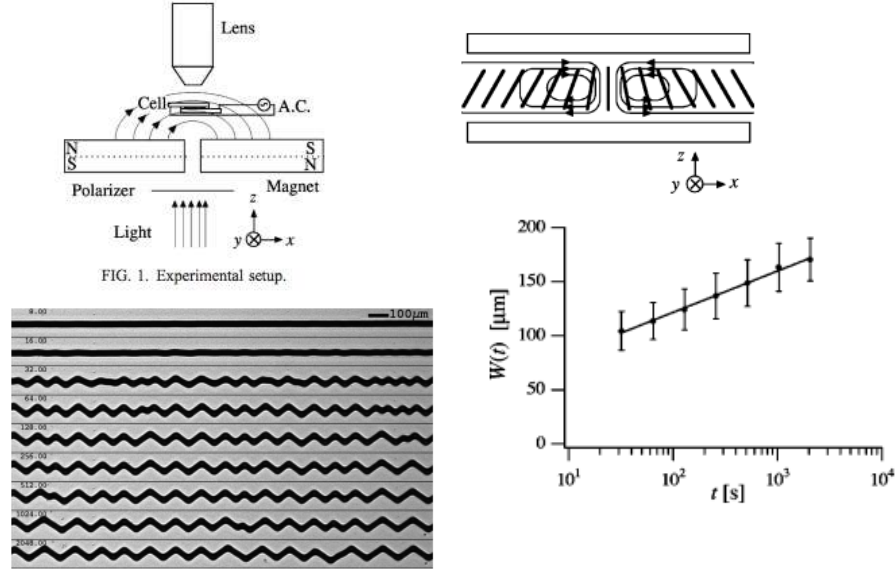


Figure 5.15: Kink dynamics in inhomogeneous electro-convection experiment. In top left panel is schematic represented the setup, in top right panel is depicted the interface between two convection rolls, in bottom left panel is illustrated a sequence of temporal snapshot of the interface and in bottom right panel the temporal evolution of average length between kinks [147].

A macroscopic parameter characterizing the dynamics of kinks is the average distance between kinks $\langle l \rangle$, defined by

$$\langle l(t) \rangle \equiv \sum_i \frac{x_{i+1}(t) - x_i(t)}{N(t)} = \frac{L}{N(t)}, \quad (5.52)$$

where $N(t)$ the number of kinks at time t . Indeed, this quantitative characterizes the number of kink inside the system. Since the kink interaction controls the dynamics of these defects, the above expression also must be controlled by this interaction. Thus, this also should be self-similar, i.e.

$$\begin{aligned} \langle l + \lambda \rangle &= \langle l(te^{\sqrt{2\epsilon}\lambda}) \rangle, \\ \langle l + \lambda \rangle &= \langle l(t) \rangle + \lambda \end{aligned} \quad (5.53)$$

then

$$\langle l(te^{\sqrt{2\epsilon}\lambda}) \rangle = \langle l(t) \rangle + \lambda. \quad (5.54)$$

The only function that satisfies the above property is

$$\langle l(t) \rangle = \frac{1}{\sqrt{2\epsilon}} \ln(t). \quad (5.55)$$

Therefore, one can infer that the number of kink decrease logarithmic in time, $N(t) = \sqrt{2\epsilon}/\ln(t)$. That is, from interaction laws of defects one can deduce macroscopic laws. This type of behavior is usually denominated as coarsening dynamics [176]. Figure 5.15 shows a set up of inhomogeneous electro-convection, which has interface between two convection rolls [147, 148]. This interface due to the anisotropic elastic constant is unstable generating a complex dynamic of kinks as illustrated in Fig. 5.15. A kink separates two regions with opposite slope. Experimentally it was studied the average distance of kinks as a function of time and found that satisfies a logarithmic law [147]. This confirms the results presented above.

5.4.3 Effect of discretization kink interaction

Numerical simulations of model Eq. (5.25) from an initial uniform solution $u = 0$ with noise and positive ϵ is characterized by the appearance of several domains (cf. Fig. 5.14). The interaction between nearest walls is characterized by annihilating, kinks interaction; however for sufficiently large time, the system is frozen. That is, domains are no longer changed in the course of time. This phenomenon can be understood by the combination of two factors: firstly the kink interaction which is very weak and on the other hand the discreteness of the system under simulation. A discrete system can be described by an effective continuous equation of the [59]

$$\partial_t u = \epsilon u - u^3 + \partial_{xx} u + \Gamma_{dx}(x) \partial_{xx} u + \Gamma'_{dx}(x) \partial_x u, \quad (5.56)$$

where $\Gamma_{dx}(x)$ is a small spatial periodic function with dx period, $\Gamma_{dx}(x + dx) = \Gamma_{dx}(x)$, and Γ'_{dx} accounts for derivative of Γ_{dx} . This function accounts for the discreteness of the system. The presence of periodic forcing modified the front dynamics by a periodic force (Peierls- Nabarro force). Similarly, the kinematic law of kink Eq. (5.47), is modified by

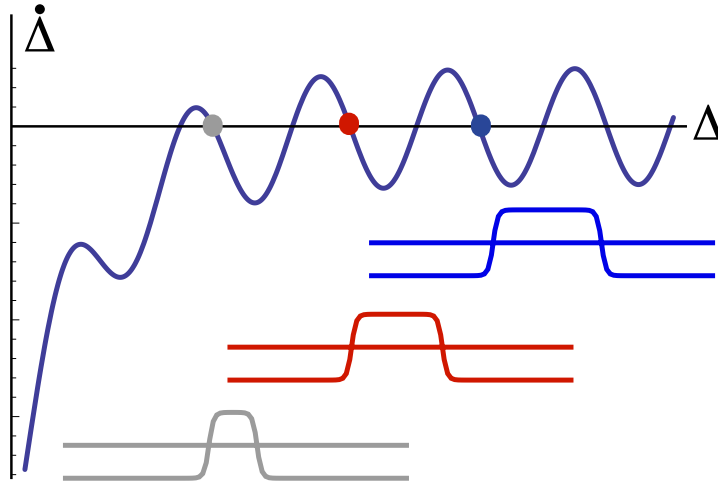


Figure 5.16: Kink interaction formula (5.57). the inset account for different localized states.

the presence of a periodic force, then this reads

$$\dot{\Delta} \approx -be^{-\sqrt{2\epsilon}\Delta} + \gamma_{dx}(\Delta), \quad (5.57)$$

where $\gamma_{dx}(\Delta)$ is a periodic function, $\gamma_{dx}(\Delta + dx) = \gamma_{dx}(\Delta)$. Figure 5.16 depicts the typical kink force. For large enough distance between kinks ($\Delta \gg \sqrt{\epsilon}$), the system has several equilibrium positions as a result of discreteness, i.e., the interaction is completely neglected. These positions correspond to the kink takes a symmetrical distribution of the points that form it. Decreasing the distance between the kinks, the interaction between kinks becomes more relevant. The system exhibits a family of localized states with different widths. The localized structures width is of order of multiple of dx . It is important to note that these localized solutions are not solutions of Eq. (5.25), but are solutions of corresponding discrete model of Eq. (5.25)⁵ or effective Eq. (5.56). Therefore from the discreteness, we have visualized the possibility of localized states.

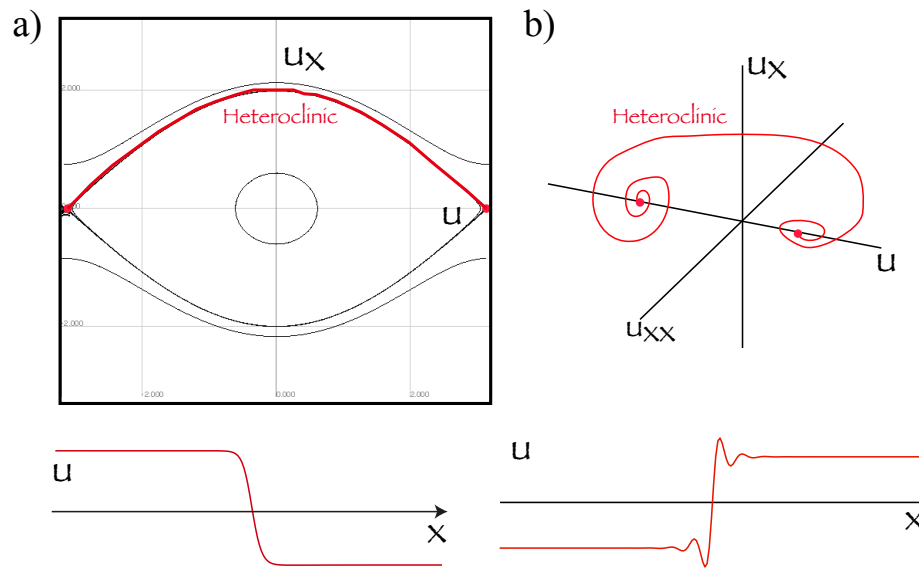


Figure 5.17: Schematic representation of heteroclinic curves for a spatial dynamical system of different dimensions. Top panels show the heteroclinic curves in their respective phase portrait. Bottom panels display the respective profile of their respective heteroclinic curves.

5.5 Localized states as result of kink interaction

During the last years, emerging macroscopic particle-type solutions or localized states or localized structure in macroscopic extended dissipative systems have been observed in different fields, such as: domains in magnetic materials, chiral bubbles in liquid crystals, current filaments in gas discharge, spots in chemical reactions, localized states in fluid surface waves, oscillons in granular media, isolated states in thermal convection, solitary waves in nonlinear optics, among others [82, 175, 2]. Hence, one can infer the universality of the localized states dynamics. Although these states are spatially extended, they exhibit properties typically associated with particles. Consequently one can characterize them with a family of continuous parameters such as position, amplitude and width. This is exactly the type of description used in more fundamental physical theories like Quantum Mechanics and Particle Physics. However, localized

⁵which is using for the numerical analysis.

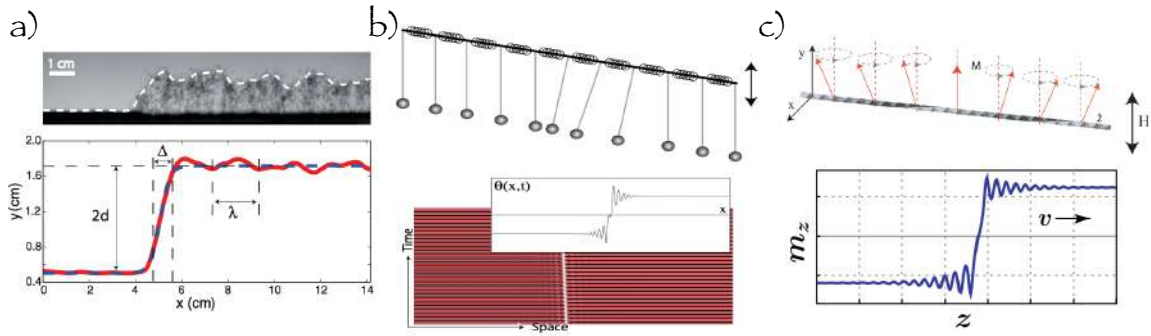


Figure 5.18: Kink solutions with damping spatial oscillations. a) fluidized granular media [154, 155], b) vertically driven chain of pendula [48, 56], and c) forcing magnetic wire with easy plane [52].

states emerging in extended dissipative systems are characterized by being made of a large number of atoms or molecules (of the order of Avogadro's number) that behave coherently.

In this section, we want to respond to the possibility of localized structure as a result of the kinks interaction. As we have seen in previous sections of kink interaction is determined by their asymptotic behavior. From the point of view of geometry in phase space, Kinks correspond to heteroclinic solutions. The heteroclinic curves are trajectories in phase portrait that connect hyperbolic points. In spatial dynamical systems of two-dimension, the homoclinic curves do not exhibit spatial oscillations (cf. Fig. 5.17a). This property is a consequence of that two-dimensional dynamic system stable manifolds are one-dimensional. The above scenario changes when the associated spatial dynamical systems have high dimensions. The hyperbolic points are characterized to have complex eigenvalues, then the associated manifolds (attractive/repulsive) are characterized to exhibit oscillatory trajectories around the hyperbolic point range. Indeed, the heteroclinic curves shows spatial damping oscillations as it tends to equilibrium. Figure 5.17 shows the typical heteroclinic curves. Kinks with spatial damping oscillation have been observed in several contexts such as driven granular media [154, 155], population dynamics [48, 56], vertically driven chain of pendula [52], forcing magnetic wire [52], to mention a few. Figure 5.18 shows kinks solution with damping oscillation

in several contexts.

5.5.1 Simple model: Turing-Swift-Hohenberg equation

In the previous sections, we have considered a simple model, Eq. (5.25), that displays spatially monotonic kinks. A natural generation of this equation, based on pioneering spirit of the work of Alan Turing [78], is considered higher gradients, that is (Turing-Swift-Hohenberg model)

$$\partial_t u = \epsilon u - u^3 + \nu \partial_{xx} u - \partial_{xxxx} u, \quad (5.58)$$

where $u = u(x, y, t)$ is a real scalar field, x and y are spatial coordinates and t is time. Depending on the context in which this equation has been derived, the physical meaning of the field variable $u(x, y, t)$ could be the electric field, deviation of molecular orientations, phytomass density, amplitude of velocity or temperature modes, or chemical concentration. The control or the bifurcation parameter ϵ measures the input field amplitude, the aridity parameter, temperature difference or chemical concentration. The parameter ν stands for the diffusion coefficient, when this parameter is negative ($\nu > 0$), it induces an anti diffusion process. Thus the first two terms on the right hand side of Eq. (5.72) account for homogeneous or local nonlinear dynamics, the third and fourth term stand for the transport mechanisms or spatial coupling via diffusion and hyperdiffusion, respectively.

Equation (5.72) is a prototype model which exhibits both localized and extended patterns. This is an isotropic nonlinear model deduced originally to describe the pattern formation of Benard convection [192]. Usually this model is denominated as Swift-Hohenberg. An important property of Eq. (5.72) is that it possess a gradient form, i.e.

$$\frac{\partial u}{\partial t} = - \frac{\delta F[u, \partial_x u, \partial_{xx} u]}{\delta u}, \quad (5.59)$$

with the functional

$$F \equiv \int \left(-\epsilon \frac{u^2}{2} + \frac{u^4}{4} + \nu \frac{(\partial_x u)^2}{2} + \frac{(\partial_{xx} u)^2}{2} \right) dx. \quad (5.60)$$

Note that using the solutions of Eq. (5.72), this functional satisfies

$$\frac{dF}{dt} = - \int dx (\partial_t u)^2 \leq 0. \quad (5.61)$$

Hence, F is a Lyapunov functional that can only decrease in the course of time. This functional guarantees that time evolution proceeds toward the state for which the functional has the smallest possible value which is compatible with the systems boundary conditions. Any initial distribution $u(x, t)$ evolves towards a homogeneous or inhomogeneous (periodic or localized) stationary state corresponding to a local or global minimum of F . The analysis of the functional F is provided in Ref. [201]. In the bistability region ($\epsilon > 0$), as result of hyperdiffusion the kink solutions exhibit spatial damping oscillations (cf. Fig. 5.17b).

Kink interaction with damping oscillations

Analogously to section 5.4.1, to study the kink interaction we can consider the following solutions

$$u(x, t) = u_k[x - x_-(t)] + u_{Ak}[x - x_+(t)] - \sqrt{\epsilon} + w(x, x_-, x_+), \quad (5.62)$$

where $\{x_-, x_+\}$ are the kink positions that are promoted temporal function and w is a small correction function. The third term of the above expression is necessary for that the kink-antikink solution in infinite tends to $-\sqrt{\epsilon}$. The above solution is represented in Fig. 5.19. The analytical expression of the kink solution is unknown, nevertheless, its asymptotic behavior is simple to characterize by linear analysis around the equilibria. Thus,

$$u_k(x \rightarrow \pm\infty) \rightarrow \pm\sqrt{\epsilon} (1 - 2\gamma e^{\mp\alpha x} \cos(\beta x + \delta_0)), \quad (5.63)$$

where $\{\alpha, \beta\}$ correspond to the real and imaginary part of eigenvalue that characterize the manifold around the equilibria $\pm\sqrt{\epsilon}$.

Introducing the above ansatz in Eq. (5.72), and linearized in w after straightforward calculations we obtain

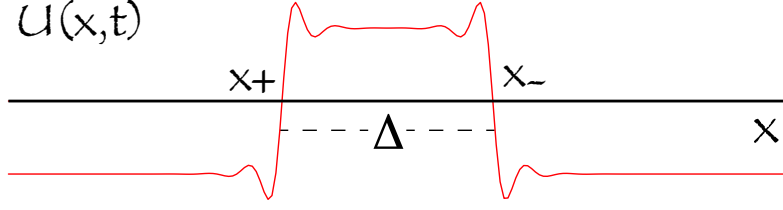


Figure 5.19: Schematic representation of a pair of kink solutions of model Eq. (??). Δ is the distance between kinks.

$$\begin{aligned} \mathcal{L}w &\equiv -(\epsilon - 3(u_k + u_{Ak} - \sqrt{\epsilon})^2 + \nu\partial_{xx} - \partial_{xxxx})w = \dot{x}_- \partial_z u_k + \dot{x}_+ \partial_z u_{Ak} \\ &- 3u_k^2(u_{Ak} - \sqrt{\epsilon}) - 3u_k(u_{Ak} - \sqrt{\epsilon})^2 + 3u_{Ak}\sqrt{\epsilon}(u_{Ak} - \sqrt{\epsilon}). \end{aligned} \quad (5.64)$$

Considering the canonical inner product

$$\langle f|g \rangle = \int_{-\infty}^{\infty} f(x)g(x)dx, \quad (5.65)$$

then \mathcal{L} is a self adjoint operator. Similarly, to what shown in Sec. 5.4.1, the linear operator \mathcal{L} has two pseudo-eigenfunctions related to translation ($|\chi_T\rangle$) and interaction ($|\chi_I\rangle$) mode, which have the form

$$\begin{aligned} |\chi_T\rangle &= \partial_x u_k + \partial_x u_{Ak} + O(e^{-\sqrt{\alpha}\Delta}), \\ |\chi_I\rangle &= \partial_x u_k - \partial_x u_{Ak} + O(e^{-\sqrt{\alpha}\Delta}). \end{aligned} \quad (5.66)$$

Introducing the central position $\delta(t) = (x_-(t) + x_+(t))/2$ and the distance between kinks $\Delta(t) = x_-(t) - x_+(t)$, the linear Eq. (5.64) reads

$$\begin{aligned} \mathcal{L}w &= \dot{\delta}(\partial_z u_k + \partial_z u_{Ak}) - \dot{\Delta}(\partial_z u_k - \partial_z u_{Ak}) \\ &- 3u_k^2(u_{Ak} - \sqrt{\epsilon}) - 3u_k(u_{Ak} - \sqrt{\epsilon})^2 + 3u_{Ak}\sqrt{\epsilon}(u_{Ak} - \sqrt{\epsilon}). \end{aligned} \quad (5.67)$$

Imposing the solvability condition, one gets

$$\begin{aligned} \dot{\delta}||\chi_T||^2 &= \langle \partial_z u_k | 3u_k^2(u_{Ak} - \sqrt{\epsilon}) - 3u_k(u_{Ak} - \sqrt{\epsilon})^2 + 3u_{Ak}\sqrt{\epsilon}(u_{Ak} - \sqrt{\epsilon}) \rangle \\ &+ \langle \partial_z u_{Ak} | 3u_{Ak}^2(u_k - \sqrt{\epsilon}) - 3u_{Ak}(u_k - \sqrt{\epsilon})^2 + 3u_k\sqrt{\epsilon}(u_k - \sqrt{\epsilon}) \rangle, \\ \dot{\Delta}||\chi_I||^2 &= \langle \partial_z u_k | 3u_k^2(u_{Ak} - \sqrt{\epsilon}) - 3u_k(u_{Ak} - \sqrt{\epsilon})^2 + 3u_{Ak}\sqrt{\epsilon}(u_{Ak} - \sqrt{\epsilon}) \rangle \\ &- \langle \partial_z u_{Ak} | 3u_{Ak}^2(u_k - \sqrt{\epsilon}) - 3u_{Ak}(u_k - \sqrt{\epsilon})^2 + 3u_k\sqrt{\epsilon}(u_k - \sqrt{\epsilon}) \rangle. \end{aligned} \quad (5.68)$$

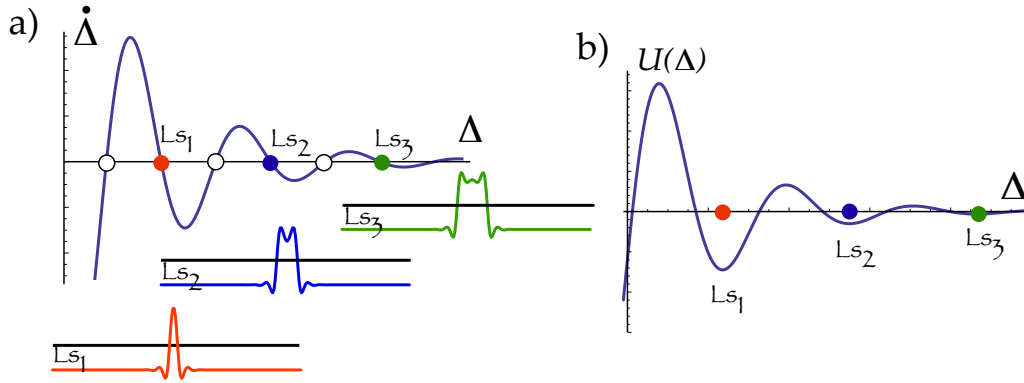


Figure 5.20: Schematic representation of the kink interaction. a) Interaction law, Δ accounts for the localized structure width. Ls_i stands for the i -localized structure. The insets account for the different localized structures. b) Potential of the interaction.

Using the asymptotic behaviors of kink and anti-kink solutions, symmetry arguments, and similar arguments using in Sec. 5.4.1, after straightforward calculations we obtain

$$\begin{aligned}\dot{\delta} &= 0, \\ \dot{\Delta} &= -b_1 e^{-\alpha\Delta} \cos(\beta\Delta + \delta_1),\end{aligned}\tag{5.69}$$

where $\{b_1, \delta_1\}$ are parameters determined numerically. The first equation tells us that the center position is not changed by the displacement of the kinks. The second equation tells us that the kink interaction alternates between being attractive and positive, and its intensity decays exponentially with the kink distance. Hence, the system exhibits a family of localized states with different widths, which are of the order of a multiple of the wavelength of the kink spatial oscillation [70, 73]. Figure 5.20 shows the profile of the kink interaction and depicts the smallest localized structures. Notice that the kink interaction is a variational dynamics, i.e.

$$\dot{\Delta} = -\frac{\partial U}{\partial \Delta},\tag{5.70}$$

where the potential

$$U(\Delta) = -b_1 \frac{e^{-\alpha\Delta}}{\beta^2 + \alpha^2} (\alpha \cos(\beta\Delta + \delta_1) - \beta \sin(\beta\Delta + \delta_1)).\tag{5.71}$$

From this potential, we can conclude that the smaller is the localized structure are more stable. Likewise, the respective basins of attraction are bigger for smaller localized structures. Hence, in present of noise the smaller states are more stable.

5.5.2 Localized structures as result front interaction

A natural generalization of of Turing-Swift-Hohenberg Eq. (5.72) is consider a constant term in the dynamics, that is

$$\partial_t u = \eta + \epsilon u - u^3 + \nu \partial_{xx} u - \partial_{xxxx} u, \quad (5.72)$$

where η parameter breaks the reflection symmetry $u \rightarrow -u$, thus it accounts for the asymmetry between homogeneous states. This parameter becomes the pitchfork bifurcation in an imperfect one. This model was initially proposed to describe the dynamics of the envelope electric field inside a nonlinear cavity, which is forced with an external electric field at its resonant frequency [197, 142]. As we have shown in Sec. 5.2, this extra parameter is responsible of front propagation between the asymmetric states. That is, this term is responsible for a drift dynamic of fronts. In order to analyze how this term affects the kink dynamics, we consider that this term as perturbative one. It is a fact of matter that we can perform an analogous analysis to the previous section incorporated the effect η (cf. Sec. 5.2) the front dynamics reads

$$\begin{aligned} \dot{\delta} &= 0, \\ \dot{\Delta} &= -b_1 e^{-\alpha \Delta} \cos(\beta \Delta + \delta_1) + \frac{3\sqrt{2}}{\epsilon} \eta. \end{aligned} \quad (5.73)$$

Then the last term of the equation of interaction can be interpreted as a constant force on the dynamics of fronts. The presence of this extra force modified the size of localized structures.

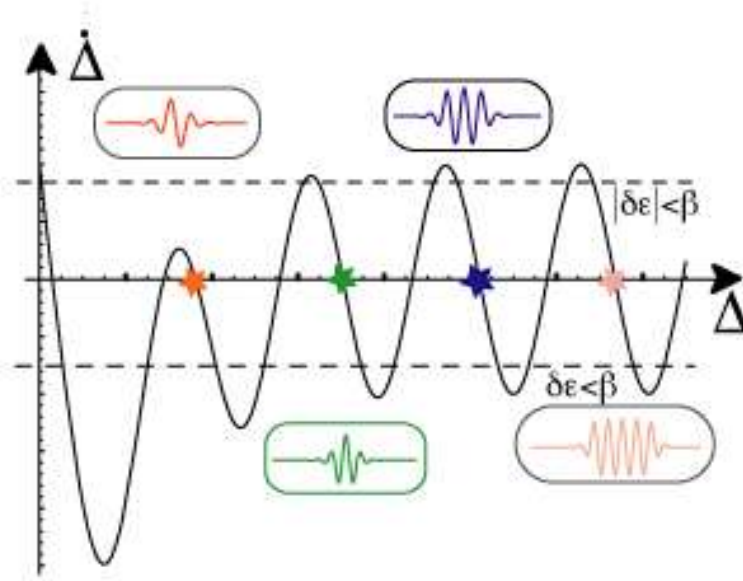


Figure 5.21: Schematic representation of the front interaction. Δ accounts for the localized structure width. Ls_i stands for the i -localized structure. The insets account for the different localized structures.

5.5.3 Amplitude approach to localized patterns and hole state

Let us consider a prototype model that exhibits localized patterns and hole solutions in one-dimensional extended system, the subcritical Swift-Hohenberg equation [182]:

$$\partial_t u = \varepsilon u + \nu u^3 - u^5 - (\partial_{xx} + q^2)^2 u, \quad (5.74)$$

where $u(x, t)$ is an order parameter, $\varepsilon - q^4$ is the bifurcation parameter, q is the wave-number of periodic spatial solutions, and ν is the control parameter of the type of bifurcation, supercritical ($\nu < 0$) or subcritical ($\nu > 0$). This model describes the confluence of a stationary and an spatial subcritical bifurcation, when the parameters scale as $u \sim \varepsilon^{1/4}$, $\nu \sim \varepsilon^{1/2}$, $q \sim \varepsilon^{1/4}$, $\partial_t \sim \varepsilon$ and $\partial_x \sim \varepsilon^{1/4}$ ($\varepsilon \ll 1$). Figure 5.22 shows typical localized patterns, hole solutions, and motionless front solutions obtained from this model. For small and negative ν , and $9\nu^2/40 < \varepsilon < 0$, the system exhibits coexistence between a stable homogenous state $u(x) = 0$ and a periodic spatial one

$$u(x) = \sqrt{\nu} \left(\sqrt{2(1 + \sqrt{1 + 40\varepsilon/9\nu^2})} \cos(qx) \right) + o(\nu^{5/2}). \quad (5.75)$$

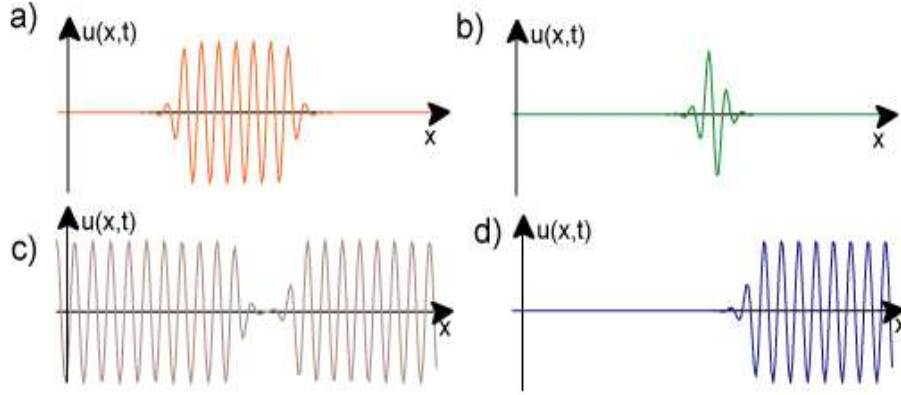


Figure 5.22: Particle type solutions appear in the subcritical Swift-Hohenberg equation (5.74). The parameters have been chosen as $\epsilon = -0.16$, $\nu = 1.00$, and $q = 0.70$. (a) Localized pattern, (b) shortest localized pattern, (c) hole solution, and (d) front solution.

In this parameter region, one finds a front between these two stable states (cf. Fig. 5.22). In order to describe the front, localized patterns and hole solutions, we introduce the ansatz

$$u = \sqrt{\frac{2\nu}{10}}\epsilon^{1/4} \left\{ A \left(y = \frac{3\sqrt{|\epsilon|}}{2\sqrt{10}q}x, \tau = \frac{9\nu^2|\epsilon|}{10}t \right) + w_1(x, y, \tau) \right\} e^{iqx} + c.c., \quad (5.76)$$

where $A(y, \tau)$ is the envelope of the front solution, $w_1(x, y, \tau)$ is a small correction function of order ϵ , and $\{y, \tau\}$ are slow variables. Note that in this ansatz we consider that q is order one, or larger than the other parameters. Introducing the above ansatz in Eq. (5.74) and linearizing in w_1 , we find the following solvability condition

$$\partial_\tau A = \epsilon A + |A|^2 A - |A|^4 A + \partial_{yy} A + \left(\frac{A^3}{9\nu} - \frac{A^3 |A|^2}{2} \right) e^{\frac{2iqy}{a\sqrt{|\epsilon|}}} - \frac{A^5}{10} e^{\frac{4iqy}{a\sqrt{|\epsilon|}}}, \quad (5.77)$$

where $\epsilon \equiv 10\epsilon/9\nu^2$, and $a \equiv 3\nu/2\sqrt{10}q$. The terms proportional to the exponential are non-resonant, that is, one can eliminate these terms by an asymptotic change of variables. Furthermore, they have rapidly varying oscillations in the limit $\epsilon \rightarrow 0$. Hence, one usually neglects these terms (non-resonant terms). Non-resonant terms have been fundamental to explain the existence of localized patterns [47], pinning phenomena of

fronts [46, 22], and localized states in bistable pattern forming systems [31]. Note that, the above envelope equation is a universal model, close to a spatial bifurcation, of a system that exhibits coexistence between an homogeneous state and spatially periodic one. In general, one can use an ansatz similar to (5.76) and noticing that the envelope satisfies independently the symmetries $\{x \rightarrow -x, A \rightarrow \bar{A}\}$, and $\{x \rightarrow x + x_o, A \rightarrow Ae^{iqx_o}\}$ one derives equation (5.77).

When one considers only the resonant terms, that is, when all spatial forcing terms are neglected. It is straightforward to show that the system has a front solution between two homogeneous states, 0 and $\sqrt{(1 + \sqrt{1 + 4\epsilon})}/2$, when $-1/4 < \epsilon < 0$. This front propagates from the global stable (global minimum) to the metastable one (local minimum). At the Maxwell point, where the equilibrium states have the same energy, the front is motionless. This point is reached at $\epsilon_M = -3/16$, where the front solution has the form

$$a_{\pm}(y) = \sqrt{\frac{3/4}{1 + e^{\pm\sqrt{3/4}(y-y_o)}}} e^{i\theta},$$

where y_o is the front's core position, and θ is an arbitrary phase.

To describe a localized pattern exhibited by (5.74) as the interaction of two fronts, we must then consider the non-resonant terms in the envelope equation (5.77). We consider all these terms as perturbations because they have rapidly varying oscillations. Close to the Maxwell point, we use the ansatz

$$A_{LP}(y, \tau) = \left[a_-(y - y_1(\tau)) + a_+(y - y_2(\tau)) - \sqrt{\frac{3}{4}} + \rho(y_1, y_2, y, \tau) \right] e^{i\theta(y_1, y_2, y, \tau)},$$

where $\{\rho, \theta\}$ are small correction functions, which are of order $\delta\epsilon \equiv (\epsilon - \epsilon_M)$ and $y_2 > y_1$. Introducing the above ansatz in equation (5.77), linearizing in $\{\rho, \theta\}$ and after straightforward calculations, we obtain the following solvability condition for the distance between the fronts

$$\frac{d\Delta}{d\tau} = f(\Delta) \equiv -\alpha\Delta \exp\left(-\sqrt{\frac{3}{4}}\Delta\right) + \beta \cos(2q\Delta/\sqrt{\epsilon}) + 2\delta\epsilon, \quad (5.78)$$

where $\Delta \equiv y_2 - y_1$, $\alpha = 27\sqrt{3}/64$ and $\beta = 64\sqrt{3}q^2 \exp(-q4\pi/\sqrt{\epsilon})/3\epsilon$. Figure 5.21 displays the interaction between two fronts. It is important to notice that in one-

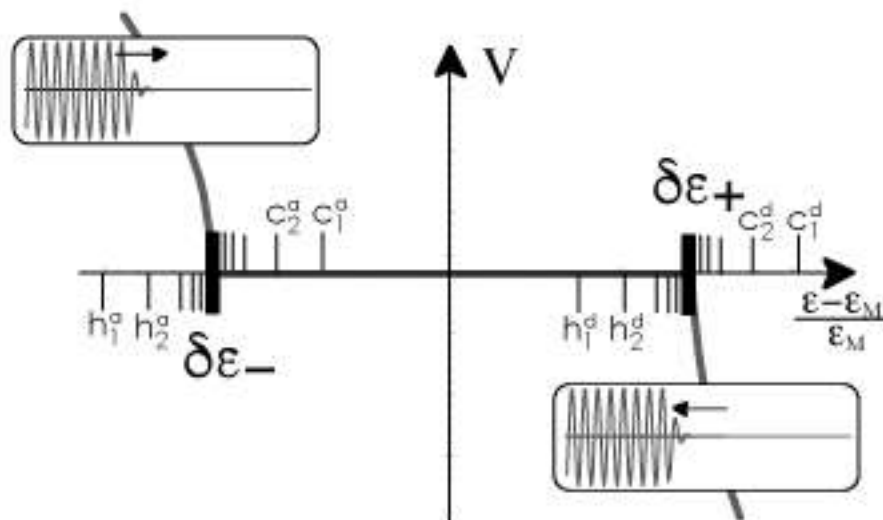


Figure 5.23: Speed of the front and bifurcation diagram of the localized patterns and hole solutions as a function of the bifurcation parameter. The thick solid line is the front velocity. c_i^a and c_i^d (h_i^a and h_i^d) represent the bifurcation points where the localized patterns with (hole solutions without) i -bumps appears and disappear, respectively.

dimensional extended systems with bistable uniform states, the dependence of the front interaction on the front distance (Δ) is purely exponential. In the present case, the linear and periodic dependence on Δ is a consequence of the interaction (contained in the non-resonant terms) of the large scale with the small scale of the underlying spatially periodic solution. The system has several equilibria, $f(\Delta^*) = 0$, that are stable if $f'(\Delta^*) < 0$. Thus, the existence and stability of localized patterns is given by the oscillatory nature of the front interaction. As it is illustrated in Fig. 5.21, each region of attractive and repulsive interaction is separated by localized patterns. It is important to notice also that the larger equilibrium (Δ^*) represent localized patterns with a larger number of bumps.

To understand the bifurcation diagram of localized patterns, we consider the effect of changing the bifurcation parameter ϵ . Modifying ϵ is equivalent to move the abscissa on the graph of front interaction (cf. Fig. 5.21). First, we consider the case $|\delta\epsilon| > \beta$ and $\delta\epsilon < 0$; the interaction is always attractive, that is, there is no equilibrium. Hence,

if one takes into account a front that connects the homogenous state with the spatially periodic state, then the spatially periodic state invades the homogenous one. Increasing ϵ , one finds the first equilibrium point $\Delta = \infty$ for $\delta\epsilon = \delta\epsilon_- \equiv \beta$ and $\delta\epsilon < 0$. Here, the system has a motionless front between the spatially periodic state and the homogenous one. This front remains stationary until $|\delta\epsilon| \leq \beta$, therefore this front is motionless in a parameter range. This phenomenon is well-known as *Locking phenomenon* and the interval $|\delta\epsilon| \leq \beta$ is denominated pinning range [174]. For $\delta\epsilon > \beta$, the front propagates from the spatially periodic state to the homogenous one. In Figure 5.23, the thick solid line is the velocity of front propagation as a function of the bifurcation parameter. Increasing $\delta\epsilon$ from $\delta\epsilon_-$, we observe that the equilibria, that is, localized patterns, appear by successive saddle-node bifurcations each time with a length smaller than the previous one, i.e., the localized patterns appear by pairs, one stable and another unstable, and each time with a smaller number of bumps. This sequence of bifurcations is illustrated in Fig. 5.23 by the points c_i^a . For $\delta\epsilon$ small, and close to the Maxwell point, the system has an infinite number of localized patterns with all the possible number of bumps. The length of the localized patterns are roughly multiple of that of the shortest localized state (one bumps). Contrarily, for $|\delta\epsilon| > \beta$, the localized patterns disappear by saddle node bifurcations and increasing $\delta\epsilon$ the larger localized patterns disappear one after the other. Hence, the shortest localized state is the last to disappear. Figure. 5.23 depicts the sequence of these bifurcation are represented by the points c_i^d . The bifurcation diagram presented above was established by Couillet et al. [72] based on arguments from the properties of invariant manifolds and chaos theory (cf. left panels of Fig. 5.24). In parallel, studying the localized structures close to a 1: 1 resonance, Champneys and Wood [208] established the bifurcation diagram of the localized patterns called *the homoclinic snaking bifurcation diagram*. Figure 5.24 illustrates the diagram that characterizes these solutions.

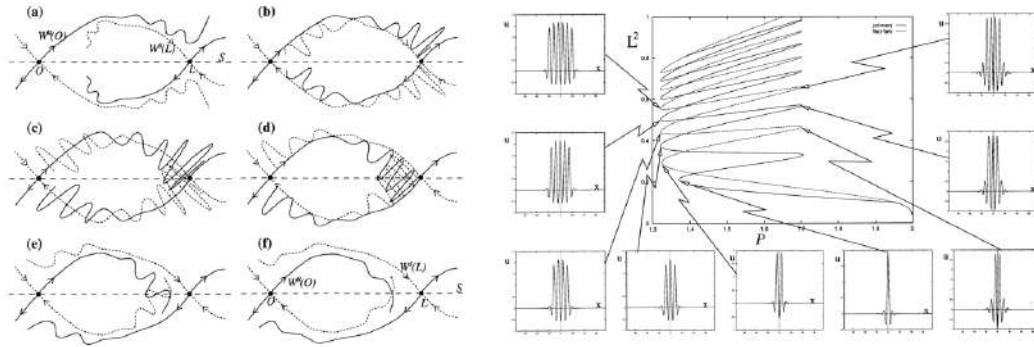


Figure 5.24: Homoclinic Snaking bifurcation diagram. The left panels account for invariant manifolds' geometry near a homoclinic bifurcation?the right-hand panels of the bifurcation diagram exhibited by the different localized solutions in the Swift-Hohenberg model [208].

5.5.4 Snaking bifurcation diagrams

5.6 Liftshitz normal form: non variational generalization of Turing-Swift-Hohenberg Equation

In the previous section, we considered a generalization of the Swift-Hohenberg equation (5.72) that considers a term that breaks the reflection symmetry of the order parameter. However, the relevant question that one must establish is the general model that describes the formation of the pattern in one-dimensional systems. As result of the spatial and temporal scales separation of the microscopic variables, the dynamics of macroscopic systems is described by a small number of variables (coarse-graining process), which generally satisfy non-variational or non-gradient equations [149, ?, 74, ?]. Indeed, the evolution of these dynamic systems is not characterized by the minimization of a free energy [?, ?]. Then, in this type of system, one expects to observe permanent behavior such as oscillations, chaos, temporal space chaos, and turbulence among others.

In this framework, walls connecting two equivalent vectorial fields through spontaneous symmetry breaking can spread according to a given chirality of the vector field [?]. This mechanism, the non-variational Ising–Bloch transition, is well known [?]. The deeper

understanding of the front propagation in macroscopic systems out of equilibrium will open the possibilities for applications in non-equilibrium crystal growth, operation of non-equilibrium magnetic and optical memories, control of non-equilibrium chemical reactions, to mention a few.

The aim of this rapid communication is to show that front solutions in scalar field models generically propagate based on two mechanism: i) the energy difference between states, and ii) non-variational effects. Considering a simple non-variational bistable model, we show analytically and numerically that the front propagation is led by non-variational dynamics. A quasi one-dimensional liquid-crystal light valve (LCLV) experiment with optical feedback allow us to evidence non-variational front propagation between different molecular orientations. Free diffraction length allows us to control the variational or non-variational nature of this optical system. A phenomenological model for small free diffraction length is derived. Numerical simulations of this model have quite good agreement with experimental observations.

Simple bistable model.- Let us consider a bistable model

$$\begin{aligned}\partial_t u &= \eta + \mu u - u^3 + \partial_{xx} u + \epsilon [c(\partial_x u)^2 + bu\partial_{xx} u], \\ &= -\frac{\delta F}{\delta u} + \epsilon F_{NV},\end{aligned}\tag{5.79}$$

where the scalar field $u(x, t)$ is an order parameter that accounts for an imperfect pitchfork bifurcation [?], μ is a bifurcation parameter, η stands for the asymmetry between the equilibria, ϵ is a small parameter, $\epsilon \ll 1$, that controls non-variational force $F_{NM} \equiv c(\partial_x u)^2 + bu\partial_{xx} u$, $\{c, b\}$ account for, respectively, nonlinear convective and diffusive terms, and the functional

$$F \equiv \int dx \left[V(u) + \frac{(\partial_x u)^2}{2} \right],\tag{5.80}$$

Figure 5.25: (color online) Front propagation in the bistable variational model Eq. (5.79) with $\epsilon = 0$. The upper panels represent the potential, $V(u)$, for different values of η , (a) $\eta = 0.2$, (b) $\eta = 0$, and (c) $\eta = -0.2$ with $\mu = 1.0$. The middle and lower panels illustrate the front profile and their respective spatiotemporal evolution for $\mu = 1.0$, $\eta = 0.3$ (d, f), and $\eta = -0.3$ (e, g).

5.6. LIFTSHITZ NORMAL FORM: NON VARIATIONAL GENERALIZATION OF TURING-SWIFT-

Figure 5.26: (color online) Non-variational front propagation model, Eq. (5.79), at Maxwell's point ($\eta = 0$, $\epsilon = 1$, and $\mu = 1$). (a) potential $V(u)$. Front profiles at given instant for positive $c = 3$ (b), negative $c = -3$ (c) and $b = 0$. Middle panels represents spatiotemporal evolution of front solution with positive and negative parameter c and $b = 0$. (f) Front speed as function of parameter c . Points account for the numerical front speed obtained from Eq. (??) with $b = 0$, $\eta = 0$ and $\epsilon = 1$, solid straight line is obtained from analytical formula $v_{NV} \approx (2c - b)\epsilon\mu\sqrt{2}/5$, and soft line is obtained using formula (??) with a numerical front profile u_F .

where $V(u) \equiv -\eta u - \mu u^2/2 + u^4/4$ is a potential. Notice the above model is invariant under spatial reflection symmetry ($x \rightarrow -x$). Moreover, model (5.79) is variational when $b = 2c$.

For $\epsilon = 0$, the above model (5.79) becomes a variational one. This model has two stable equilibria for η small and positive μ , $u = \pm\sqrt{\mu} + O(\eta)$, represented by $\{\mathcal{A}, \mathcal{B}\}$. Figure 5.25 depicts the potential $V(u)$ for different values of η . A nontrivial solution of this variational model is front waves, $u_F(x - vt) \approx \pm\sqrt{\mu} \tanh(\sqrt{\mu/2}(x - vt)) + O(\eta)$, that connects these two equilibria [174]. The middle and lower panels of Fig. 5.25 show the profile of the front solutions and their respective spatiotemporal evolution. Notice that fronts propagate at a constant speed. The location and the region of the space where the front has greater variation is known as front position and core, respectively. In the pioneering work of Pomeau [174], it is shown that front speed v is ($\eta \ll 1$)

$$v = v_V \equiv \frac{V(\mathcal{A}) - V(\mathcal{B})}{\int_{-\infty}^{\infty} (\partial_x u_F)^2 dx} \approx \frac{3\sqrt{2}}{2\mu} \eta. \quad (5.81)$$

Hence, the front speed is proportional to the energy difference between equilibria and the front core shape (denominator). Indeed, the most energetically favorable state

Figure 5.27: (color online) Front propagation model Eq. (5.79) with $\eta = 0.3$ and $\mu = 1$. (a) the potential $V(u)$. (b) Front profiles for zero (dashed line) and positive (solid line) c and $b = 0$. Right panels (c,d) represent spatiotemporal evolution of front solution with zero and positive parameter c . (f) Front speed as function of parameter c . Points account for the numerical front speed and continuous curve $v = v_V + v_{NV}$.

invades the least favorable one (cf. Fig. 5.79). Likewise, when both states have the same energy, $\eta = 0$, the front is motionless, which corresponds to Maxwell's point. Therefore, for variational systems the mechanism of front propagation is the energy difference between the connected equilibria.

5.7 Alee effect in population dynamics: Nagumo Model

Explicar soluciones localizadas solitarias, modelo biologico local y no local.
modelo Swift-Hohenberg, snaking bifurcation, non-variational dynamcis, aplicacion de
monolayer, Interaction law of 2D localized precession states
estructuras localizadas en sistemas forzados
inetraccion no reciprocas
soluciones topologicas y kinks
estructuras localizadas en sistmas conservativos, Bubbles en CH
Vortex localized state
solitones propagandose en estructura periodica, solitones en sistemas forzados

Bibliography

- [1] M.J. Ablowitz, D.J. Kaup, A.C. Newell, and H. Segur, *Phys. Rev. Lett.* **30**, 1262 (1973).
- [2] Thorsten Ackemann, WilliamJ Firth, and Gian-Luca Oppo. *Fundamentals and applications of spatial dissipative solitons in photonic devices*, *Advances in atomic, molecular, and optical physics*, **57**, 323, (2009).
- [3] G.P. Agrawal, *Nonlinear fiber optics*, (Springer, Berlin, Heidelberg, 2000).
- [4] D. Anderson, M. Bonnedal, and M. Lisak, *Self-trapped cylindrical laser beams*, *Phys. Fluids*, **22**, 1838 (1979).
- [5] W. C. Allee, *Animal Aggregations: A Study in General Sociology* (University Chicago Press, Chicago, IL, 1931).
- [6] W. C. Allee, *The Social Life of Animals* (Beacon Press, Boston, 1938).
- [7] A.A. Andronov, A.A. F. Vitt, and S.E. Khaikin. *Theory of Oscillators* (Pergamon Press, Oxford, 1966).
- [8] N. I. Akhiezer, *Elements of the Theory of Elliptic Functions* (Moscow, 1970)
- [9] AJ Alvarez-Socorro, MG Clerc, and M Tlidi. *Spontaneous motion of localized structures induced by parity symmetry breaking transition*, *Chaos* **28**, 053119 (2018).
- [10] G. Arfken, H. Weber, *Mathematical Methods for Physicists* (Elsevier Academic Press, Burlington, 2001).

- [11] M. Argentina and P. Coulet, *Physica A* **257**, 45 (1998).
- [12] M. Argentina, M.G. Clerc, R. Soto, *Phys. Rev. Lett.* **89** (2002) 044301.
- [13] V. I. Arnold, *Geometrical Methods in the Theory of Ordinary Differential Equations* (Springer, NY, 1983).
- [14] V.I. Arnold, *Mathematical Methods of Classical Mechanics* (Springer, 1989).
- [15] Vladimir I Arnol'd. *Catastrophe theory* (Springer Science & Business Media, 2003).
- [16] G. L. Baker and J.A., Blackburn, *The Pendulum: A Case Study in Physics*, (Oxford University Press, 2005).
- [17] I. V. Barashenkov, M.M. Bogdan, and V.I. Korobov, *Europhys. Lett.* **15**, 113 (1991).
- [18] I.V. Barashenkov, Y.S. Smirnov, *Existence and stability chart for the ac-driven, damped nonlinear Schrödinger solitons*, *Phys. Rev. E* **54**, 5707 (1996).
- [19] I. Barashenkov, E. Zemlyanaya, *Existence threshold for the ac-driven damped nonlinear Schrödinger solitons*, *Physica D* **132**, 363 (1999).
- [20] I. V. Barashenkov, N.V. Alexeeva, and E. V. Zemlyanaya, *Two-and three-dimensional oscillons in nonlinear Faraday resonance*, *Phys. Rev. Lett.*, **89**, 104101 (2002).
- [21] D. Bennett, A. Bishop, S. Trullinger, *Coherence and chaos in the driven, damped sine-Gordon chain*, *Zeitschrift für Physik B Condensed Matter* **47**, 265 (1982).
- [22] D. Bensimon, B.I. Shraiman, and V. Croquette, *Nonadiabatic effects in convection*, *Phys. Rev. A* **38**, 5461 (1988).
- [23] Ernst Julius Berg. *Heaviside's Operational Calculus as applied to Engineering and Physics* (McGraw-Hill book company, inc., 1936).

- [24] L. Bergé, Phys. Rep., **303**, 259 (1998).
- [25] E. Berrios-Caro, M.G. Clerc, M.A. Ferre, and A.O. Leon, *Oscillating decorated interfaces in parametrically driven systems*, Phys. Rev. E **97**, 012207 (2018).
- [26] J.A. Blackburn, H.J.T. Smith and N. Gronbech-Jensen, *Stability and Hopf bifurcations in an inverted pendulum* Am. J. Phys., *60* 903 (1992).
- [27] N. Bloembergen, *Nonlinear Optics* (W.A. Benjamin inc., New York 1965).
- [28] N.N. Bogoliubov, and Y. A. Mitropolski, *Asymptotic Methods in The Theory of Non-Linear Oscillations*, (Gordon and Breach, New York, 1961).
- [29] M. Bondila, I. V. Barashenkov, and M. M. Bogdan, Physica D *87*, 314 (1995).
- [30] Grigory Isaakovich Barenblatt. *Scaling, self-similarity, and intermediate asymptotics: dimensional analysis and intermediate asymptotics*, (Cambridge University Press, 1996).
- [31] U. Bortolozzo, M.G. Clerc, C. Falcon, S. Residori, and R. Rojas *Localized states in bistable pattern forming systems*, Phys. Rev. Letts. **96**, 214501 (2006).
- [32] E. Bour, *Théorie de la déformation des surfaces*, Journal de l'École Impériale Polytechnique **19** 1 (1862).
- [33] J. Boussinesq, *Essai sur la theorie des eaux courantes, Memoires presentes par divers savants* Acad. des Sci. Inst. Nat. France, XXIII, 1-670 (1877).
- [34] R. Boyd, *Nonlinear Optics* (3rd ed. Academic Press, 2008).
- [35] O.M. Braun and Y. Kivshar, *The Frenkel-Kontorova Model: Concepts, Methods, and Applications* (Springer-Verlag, Berlin, Heidelberg, 2004).
- [36] J. J. Brey, M. J. Ruiz-Montero, F. Moreno, and R. García-Rojo, Phys. Rev. E **65** (2002) 061302.

- [37] E. I. Butikov, J. Phys. A **35**, 6209 (2002); Am. J. Phys. **69**, 755 (2001).
- [38] C. Cartes, M.G. Clerc and R. Soto, Phys. Rev. E **70** (2004) 031302.
- [39] T. Cazenave, *An introduction to nonlinear Schrödinger equations* (Universidade Federal do Rio de Janeiro, Centro de Ciencias Matematicas e da Natureza, Instituto de Matematica, 1989).
- [40] E.A. Cerda and E.L. Tirapegui, *Faraday's instability for viscous fluids*, Phys. Rev. Lett., **78**, 859 (1997).
- [41] H. Chate, Nonlinearity, **7**, 185 (1994).
- [42] J. Clarke, A.I. Braginski, *The SQUID Handbook: Applications of SQUIDS and SQUID Systems*, (Wiley, Hoboken, 2006)
- [43] S. Chandrasekhar. *Liquid crystal* (Cambridge University Press, New York, 1992).
- [44] Y.K. Chembo, C.R. Menyuk, *Spatiotemporal Lugiato-Lefever formalism for Kerr-comb generation in whispering-gallery-mode resonators*, Phys. Rev. A **87**, 053852 (2013)
- [45] M. Clerc, P. Coulet, and E. Tirapegui, Phys. Rev. Lett. **83**, 3820 (1999); Opt. Commun. **167**, 159 (1999); Prog. Theor. Phys. Suppl. **139**, 337 (2000); Int. J. Bifurcation and Chaos **11**, 591 (2001).
- [46] M.G. Clerc, C. Falcon, and E. Tirapegui, *Additive noise induces front propagation*, Phys. Rev. Letters, **94**, 148302 (2005); Phys. Rev. E **74**, 011303 (2006)
- [47] M. G. Clerc, and C. Falcon, C. *Localized patterns and hole solutions in one-dimensional extended systems* Physica A **356**, 48 (2005).
- [48] M.G. Clerc, D. Escaff, and V.M. Kenkre. *Patterns and localized structures in population dynamics*, Phys. Rev. E, **72**, 056217 (2005).

- [49] M.G. Clerc, and D. Escaff, *Physica A: Statistical Mechanics and its Applications*, **371**, 33 (2006).
- [50] M.G. Clerc, P. Encina, and E. Tirapegui *Shilnikov bifurcation: Stationary quasi-reversal bifurcation* *Int. J. Bifurcation Chaos* **18**, 1905 (2008).
- [51] M.G. Clerc, P. Cordero, J. Dunstan, K. Huff, N. Mujica, D. Risso, and G. Varas, *Nature Physics*, **4**, 249 (2008).
- [52] M.G. Clerc, S. Coulibaly and D. Laroze, *Nonvariational ising?bloch transition in parametrically driven systems* *Int. J. Bifurcation Chaos* **19**, 3525-3532 (2009).
- [53] M.G. Clerc, U Bortolozzo and S Residori, *New J. Phys.* **11**, 093037 (2009).
- [54] M.G. Clerc, S. Coulibaly, N. Mujica, R. Navarro, and T. Sauma, *Soliton pair interaction law in parametrically driven Newtonian fluid*, *Phil. Trans. R. Soc. A* **367**, 3213 (2009).
- [55] M. G. Clerc, S. Coulibaly, and D. Laroze, *Phys. Rev. E.* **77**, 056209 (2008); *Physica D* **239**, 72 (2010).
- [56] M.G. Clerc, D. Escaff, and V.M. Kenkre. *Analytical studies of fronts, colonies, and patterns: combination of the allee effect and nonlocal competition interactions* *Phys. Rev. E*, **82**, 036210 (2010).
- [57] M.G. Clerc, S. Coulibaly, L. Gordillo, N. Mujica, and R. Navarro, *Coalescence cascade of dissipative solitons in parametrically driven systems*, *Phys. Rev. E* **84**, 036205 (2011).
- [58] M.G. Clerc, S. Coulibaly, M.A. Garcia-Nustes, and Y. Zarate, *Phys. Rev. Lett.* **107**, 254102 (2011).
- [59] M.G. Clerc, R.G. Elías, and R. G Rojas *Continuous description of lattice discreteness effects in front propagation*, *Phil. Trans. R. Soc. A* **369**, 412 (2011)

- [60] M.G. Clerc, C. Falcon, C. Fernandez-Oto and E. Tirapegui, *Effective-parametric resonance in a non-oscillating system*, EPL, 98, 30006 (2012).
- [61] M.G. Clerc, S. Coulibaly, D. Laroze, *Localized waves in a parametrically driven magnetic nanowire*, EPL **97**, 30006 (2012)
- [62] M. G. Clerc and N. Verschueren, Phys. Rev. E. **88**, 052916 (2013).
- [63] M.G. Clerc, M. A. Garcia-Nustes, Y. Zarate, and S. Coulibaly Phys. Rev. E. 87, 052915 (2013).
- [64] M.G. Clerc, C. Falcón, M.A. Garcia-Nustes, V. Odent, I. Ortega, *Emergence of spatiotemporal dislocation chains in drifting patterns*, Chaos **24**, 023133 (2014).
- [65] M.G. Clerc, S. Coulibaly, M.A. Ferré, M. A., Garcia-Nustes, M. A., and R.G. Rojas, *Chimera-type states induced by local coupling*, Phys. Rev. E **93**, 052204 (2016).
- [66] M. G. Clerc, M. A. Ferré, S. Coulibaly, R.G. Rojas, and M. Tlidi, *Chimera-like states in an array of coupled-waveguide resonators*, Opt. Lett., **42**, 2906 (2017).
- [67] M.G. Clerc, S. Coulibaly, M.A. Ferré, and R.G. Rojas, *Chimera states in a Duffing oscillators chain coupled to nearest neighbors*, Chaos, **28**, 083126 (2018).
- [68] A. Coillet, J. Dudley, G. Genty, L. Larger, Y.K. Chembo, *Optical rogue waves in whispering-gallery-mode resonators*, Phys. Rev. A **89**, 013835 (2014).
- [69] Diego AC Contreras and Marcel G Clerc. *Internal noise and system size effects induce nondiffusive kink dynamics*, Phys. Rev. E, **9**, 032922 (2015).
- [70] P. Couillet, C. Elphick, and D. Repaux. *Nature of spatial chaos* Phys. Rev. Lett. **58**, 431 (1987).
- [71] P. Couillet, L. Gil, and J. Lega, Phys. Rev. Lett. **62**, 1619 (1989).

- [72] P. Coulet, C. Riera, and C. Tresser, *Stable static localized structures in one dimension*, Phys. Rev. Lett. **84** 3069 (2000).
- [73] P. Coulet, *Localized patterns and fronts in nonequilibrium systems*, Int. J. Bifurcation Chaos, **12**, 2445 (2002).
- [74] M. C. Cross and P. C. Hohenberg. *Pattern formation outside of equilibrium* Rev. Mod. Phys., **65**, (1993).
- [75] J. Cuevas, L.Q. English, P.G. Kevrekidis, M. Anderson, *Discrete breathers in a forced-damped array of coupled pendula: modeling, computation, and experiment*, Phys. Rev. Lett. **102**, 224101 (2009)
- [76] J. Cuevas-Maraver, P.G. Kevrekidis, and F. Williams, *The sine-Gordon model and its applications. Nonlinear Systems and Complexity* (Springer, 2014).
- [77] Jean le Rond d'Alembert, *Recherches sur la courbe que forme une corde tendue mise en vibration*, Histoire de l'académie royale des sciences et des belles lettres, **3**, 214 (1749).
- [78] Jonathan HP Dawes. *After 1952: The later development of Alan Turing's ideas on the mathematics of pattern formation*, Historia Mathematica, **43**, 49, (2016).
- [79] P. G. de Gennes, *Short Range Order Effects in the Isotropic Phase of Nematics and Cholesterics*, Mol. Crystals & Liquid Crystals **12**, 193 (1971).
- [80] P. G. de Gennes and J. Prost. *The Physics of Liquid Crystals* (Clarendon Press, 1995).
- [81] O. Descalzi, A. Argentina, E. Tirapegui, Phys. Rev. E, **67**, 015601 (2003).
- [82] O. Descalzi, M.G. Clerc, S. Residori, G. Assanto, *Localized states in physics: solitons and patterns* (Springer-Verlag Berlin Heidelberg, 2011).

- [83] Robert Gilmore. *Catastrophe theory for scientists and engineers* (Courier Corporation, 1993).
- [84] P. A. M. Dirac, Proc R. Soc. Lond. A **117**, 610 (1928)
- [85] S. Dyachenko, V.E. Zakharov, A.N. Pushkarev, V.F. Shvets, and V.V. Yankov, Sov. Phys. JETP **69**, 1144 (1989).
- [86] B. Denardo, B. Galvin, A. GreenPeld, A. Larraza, S., Putterman, and W. Wright, Phys. Rev. Lett. **68**, 1730 (1992).
- [87] T. Dauxois, *Fermi, Pasta, Ulam, and a mysterious lady*, Physics Today **6**, 55 (2008).
- [88] J.C. Eilbeck, R.K.Dodd, J.D Gibbon and H.C.Morris, *Solitons and Nonlinear Wave Equations* (Academic Press, London 1982).
- [89] C. Elphick, G. Iooss, and E. Tirapegui, *Normal form reduction for time-periodically driven differential equations*, Phys. Lett. A **120**, 459 (1987).
- [90] L. D. Faddeev, L. A. Takhtajan, *Hamiltonian Methods in the Theory of Solitons* (Addison-Wesley, 1987).
- [91] M.A. Ferré, M. G., Clerc, S. Coulibally, R.G. Rojas, and M. Tlidi, *Localized structures and spatiotemporal chaos: comparison between the driven damped sine-Gordon and the Lugiato-Lefever model*, Eur. Phys. J. D **71**, 172 (2017).
- [92] E. Fermi, J. Pasta, S. Ulam, *Studies of Nonlinear Problems*. Document LA-1940 (1955).
- [93] R. P. Feynman, The Feynman Lectures on Physics Vol 3. (Narosa, 1965).
- [94] G. Fibich, *The nonlinear Schrödinger equation* (Springer, Berlin, 2015).
- [95] E. I. Fredholm, *Sur une classe d'équations fonctionnelles*, Acta Math. **27**, 365 (1903).

- [96] M.H. Friedman, J.E. Campana, and A.L. Yergey, *The inverted pendulum: A mechanical analog of the quadrupole mass filter*, Am. J. Phys., **50**, 924 (1982).
- [97] G. Floquet, *Sur les équations différentielles linéaires à coefficients périodiques* Annales de l'École Normale Supérieure, **12**, 47 (1883).
- [98] A. Frova and M. Marenzana, *Thus Spoke Galileo: The Great Scientist's Ideas and their Relevance to the Present Day* (Oxford University Press, 2006).
- [99] L. Gammaitoni, P. Hanggi, P. Jung, and F. Marchesoni, *Stochastic resonance*, Rev. Mod. Phys., **70**, 223 (1998) .
- [100] J. Garay, I. Ortega, M. G. Clerc, and C. Falcon Phys. Rev. E **85**, 035201(R) (2012).
- [101] R. Gilmore *Catastrophe theory for scientists and engineers* (Courier Corporation, 1993).
- [102] R. E. Goldstein, G. H. Gunaratne, L. Gil, and P. Couillet, *Hydrodynamic and interfacial patterns with broken space-time symmetry*, Phys. Rev. A **43**, 6700 (1991).
- [103] L. Gordillo, T. Sauma, Y. Zarate, I. Espinoza, M.G. Clerc and N. Mujica), *Can non-propagating hydrodynamic solitons be forced to move?* Eur. Phys. J. D **62**, 39-49 (2011).
- [104] L. Gordillo, Tesis de Doctorado, "Non-propagating hydrodynamic solitons in a quasi-one dimensional free surface subject to vertical vibrations", <http://www.thesis.uchile.cl/handle/2250/112129>.
- [105] W. Gordon, Zeitschrift für Physik. **40**, 117 (1926).
- [106] L. P. Gor'kov, and G. Grüner, G. (Eds.). *Charge density waves in solids*. (Elsevier, 2012) .
- [107] K. A. Gorshkov and L. A. Ostrovsky, Physica D, **3**, 428 (1981).

- [108] J. Hale and H. Kocak, *Dynamics and Bifurcations* (Texts in Applied Mathematics. Springer-Verlag, New York, 1991).
- [109] T. Hansson, D. Modotto, S. Wabnitz, *Dynamics of the modulational instability in microresonator frequency combs*, Phys. Rev. A **88**, 023819 (2013).
- [110] A. Hasegawa and F. Tappert. *Transmission of stationary nonlinear optical pulses in dispersive dielectric fibers. Anomalous dispersion*, Appl. Phys. Lett. **2**, 142 (1973).
- [111] A. Hasegawa, *Optical Solitons in Fibers* (Springer, 1989).
- [112] M. Haelterman, S. Trillo, S. Wabnitz, *Dissipative modulation instability in a nonlinear dispersive ring cavity*, Optics communications **91**, 401 (1992)
- [113] P. Holmes, J. L. Lumley, and G. Berkooz, *Turbulence, Coherent Structures, Dynamical Systems and Symmetry* (Cambridge University Press, Cambridge, 1998).
- [114] A. Jackson A., *Perspectives of Nonlinear Dynamics*, Vol. 2 (Cambridge University Press, 1985).
- [115] B. D. Josephson, *Possible new effect in superconducting tunneling*, Phys. Lett. **1**, 251 (1962).
- [116] H.P. Kalmus, *The inverted pendulum*, Am. J. Phys., **38**, 874 (1970).
- [117] K. Kaneko and I. Tsuda, *Chaos and Beyond: A Constructive Approach with Applications in Life Sciences* (Springer, Berlin 1996).
- [118] P. L. Kapitza, *Dynamic stability of the pendulum with vibrating suspension point* Sov. Phys. JETP, **21**, 588 (1951); in *Collected Papers of P. L. Kapitza*, edited by Ter Haar D. (Pergamon Press) 1965.
- [119] D.J. Kaup, A.C. Newell, *Theory of nonlinear oscillating dipolar excitations in one-dimensional condensates* Phys. Rev. B **18**, 5162 (1978).

- [120] Kyozi Kawasaki and Takao Ohta. *Kink dynamics in one-dimensional nonlinear systems*, Physica A **116**, 573, (1982).
- [121] J. Kerr, Philosophical Magazine. 4 **50**, 337 (1875).
- [122] J.K. Kevorkian and J.D.Cole, *Multiple scale and singular perturbation methods* (Springer Science & Business Media, 2012).
- [123] Charles Kittel. *Introduction to solid state physics* (Wiley, 2005).
- [124] Y.S. Kivshar, and B. Luther-Davies, Phys. Rep. **298**, 81 (1998).
- [125] Y.S. Kivshar, B.A. Malomed, *Dynamics of solitons in nearly integrable systems*, Rev. Mod. Phys. **61**, 763 (1989)
- [126] O. Klein, Zeitschrift für Physik. **37**, 895 (1926).
- [127] T. A. Kontorova and Y. I. Frenkel, Zh. Eksp. Teor. Fiz., **8**, 1340 (1938).
- [128] D.J Korteweg, G. de Vries, Philosophical Magazine 39, 422 (1895).
- [129] P. Kockaert, P. Kockaert, G. Van der Sande, I. Veretennicoff, M. Tlidi, *Negative diffraction pattern dynamics in nonlinear cavities with left-handed materials*, Phys. Rev. A **74**, 033822 (2006)
- [130] Y. Kuramoto, *Chemical Oscillations, Waves, and Turbulence* (Springer-Verlag, Berlin, Heidelberg, 1984).
- [131] L.D. Landau and E.M. Lifshitz, *Course of Theoretical Physics, Mechanics, Volume 1* (Pergamon Press, 1976).
- [132] L.D. Landau, M.E. Lifshitz, *Course of Theoretical Physics: Fluid Mechanics, Volume 6*.
- [133] L. D. Landau and E. M. Lifshitz, *Course of Theoretical Physics, Electrodynamics of Continuous Media* (Oxford University Press, Oxford, UK, 1960), Vol. 8.

- [134] L.D. Landau, M.E. Lifshitz. *Course of theoretical Physics. Volume 9: Statistical Physics; Part 1.* (Oxford, Singapore, 1980).
- [135] D.W. Mc. Laughlin, J.V. Moloney, A.C. Newell, *Solitary waves as fixed points of infinite-dimensional maps in an optical bistable ring cavity*, Phys. Rev. Lett. 51, 75 (1983); *New class of instabilities in passive optical cavities*, Phys. Rev. Lett. 54, 681 (1985).
- [136] F. Leo, S. Coen, P. Kockaert, S.P. Gorza, P. Emplit, and M. Haelterman, *Temporal cavity solitons in one-dimensional Kerr media as bits in an all-optical buffer*. Nature Photonics, **4**, 471 (2010).
- [137] F. Leo, L. Gelens, P. Emplit, M. Haelterman, S. Coen, *Dynamics of one-dimensional Kerr cavity solitons*, Opt. Express *21*, 9180 (2013).
- [138] K.K. Likharev, *Dynamics of Josephson Junctions and Circuits*, (Gordon and Breach science publishers, New York, 1985).
- [139] Z. Liu, M. Ouali, S. Coulibaly, M.G. Clerc, M. Taki, M. Tlidi, *Characterization of spatiotemporal chaos in a Kerr optical frequency comb and in all fiber cavities*, Opt. Lett. **42**, 1063 (2017).
- [140] O. Lioubashevski, H. Arbell, and J. Fineberg, Phys. Rev. Lett. **76**, 3959 (1996).
- [141] O. Lioubashevski, Y. Hamiel, A. Agnon, Z. Reches, and J. Fineberg, Phys. Rev. Lett. **83**, 3190 (1999).
- [142] Paul Mandel. *Theoretical problems in cavity nonlinear optics*, (Cambridge University Press, 2005).
- [143] E. Livne, B. Meerson, and P.V. Sasorov, Phys. Rev. E **65** (2002) 021302.
- [144] S Longhi, Phys. Rev. E **53**, 5520 (1996).

- [145] L.A. Lugiato, R. Lefever, *Spatial dissipative structures in passive optical systems* Phys. Rev. Lett. **58**, 2209 (1987)
- [146] L. Lugiato, F. Prati, and M. Brambilla, *Nonlinear optical systems* (Cambridge University Press, Cambridge 2015).
- [147] Tomoyuki Nagaya and Jean-Marc Gilli. *Experimental study of coarsening dynamics of the zigzag wall in a nematic liquid crystal with negative dielectric anisotropy* Phys. Rev. E, **65**, 051708 (2002).
- [148] Tomoyuki Nagaya and Jean-Marc Gilli. *Experimental study of spinodal decomposition in a 1d conserved order parameter system*, Phys. Rev. Lett., **92**, 145504 (2004).
- [149] G. Nicolis and I. Prigogine, *Self-Organization in Non Equilibrium Systems* (J. Wiley & Sons, New York, 1977).
- [150] A. C. Newell, *Solitons in Mathematics and Physics* (Society for Industrial and Applied Mathematics, Philadelphia 1985).
- [151] A.C. Newell, D.A. Rand, and D. Russell, Physica D **33**, 281 (1988).
- [152] A.C. Newell, T. Passot, and J. Lega, *Order parameter equations for patterns*, Annu. Rev. fluid Mech. **25**, 399 (1993).
- [153] K. Nozaki, N. Bekki, *Solitons as attractors of a forced dissipative nonlinear Schrödinger equation*, Phys. Lett. A **102**, 383 (1984)
- [154] JE Macías, MG Clerc, C Falcón, and MA Garcia-Nustes. *Spatially modulated kinks in shallow granular layers*, Phys. Rev. E, **88**, 020201 (2013).
- [155] JE Macias, J. E.as and C Falcon. *Dynamics of spatially modulated kinks in shallow granular layers* New Journal of Physics, **16**, 043032 (2014).

- [156] B. A. Malomed, *Soliton management in periodic systems* (Springer Science & Business Media, 2006).
- [157] Nicholas Manton and Paul Sutcliffe. *Topological solitons* (Cambridge University Press, 2004).
- [158] E. Mathieu, *Mémoire sur le mouvement vibratoire d'une membrane de forme elliptique*, Journal de mathématiques pures et appliquées, **13**, 137 (1868).
- [159] N. W. McLachlan, *Theory and application of Mathieu functions* (Publisher to the University Geoffrey Cumberlege, Oxford University Press, 1951).
- [160] M. M. Michaelis, *Stroboscopic study of the inverted pendulum* Am. J. Phys., **53**, 1079 (1985).
- [161] J. Miles, J. Fluid Mech **83**, 153 (1977).
- [162] J.W. Miles, J. Fluid Mech. **148**, 451 (1984).
- [163] L.F. Mollenauer, R.H. Stolen, and J.P. Gordon, Phys. Rev. Lett. **45**, 1095 (1980).
- [164] J. Monoley, and A. Newell, *Nonlinear optics*, (CRC Press, Boca raton, 2018).
- [165] G.J. Morales, Y.C. Lee, *Ponderomotive-force effects in a nonuniform plasma* Phys. Rev. Lett. **33**, 1016 (1974).
- [166] J. D. Murray, *Mathematical Biology* (Springer-Verlag, Berlin, 1989).
- [167] E. Ott, *Chaos in Dynamical Systems*, (Cambridge University Press, 2002).
- [168] F. Palmero, J. Han, L.Q. English, T. Alexander, P. Kevrekidis, *Multifrequency and edge breathers in the discrete sine-Gordon system via subharmonic driving: Theory, computation and experiment* Phys. Lett. A **380**, 402 (2016).
- [169] B. Perthame, *Transport Equations in Biology, Frontiers in Mathematics* (Springer-Verlag, New York, 2008).

- [170] U. Peschel, O. Egorov, F. Lederer, *Discrete cavity solitons* Opt. Lett. **29**, 1909 (2004)
- [171] A. Pikovsky, M. Rosenblum, and J. Kurths, *Synchronization: A Universal Concept in Nonlinear Sciences* (Cambridge University Press, Cambridge, 2001).
- [172] L. M. Pismen, *Patterns and interfaces in dissipative dynamics* (Springer Science & Business Media, 2006).
- [173] L. Pitaevskii, and S. Stringari, *Bose-Einstein Condensation*, (Clarendon, Oxford, U.K., 2003).
- [174] Y. Pomeau, *Front motion, metastability and subcritical bifurcations in hydrodynamics*, Physica D **23**, 3 (1986).
- [175] H.G. Purwins, H. Bdeker, S. Amiranashvili, *Dissipative solitons* Adv. Phys. **59**, 485 (2010).
- [176] Lorenz Ratke and Peter W Voorhees. *Growth and coarsening: Ostwald ripening in material processing* (Springer Science & Business Media, 2013).
- [177] M. Remoissenet, *Waves called solitons: concepts and experiments*. (Springer Science & Business Media, 2013).
- [178] Wulf Rossmann. *Lie groups: an introduction through linear groups*, (Oxford University Press on Demand, 2002).
- [179] B. Rumpf, and A.C. Newell, Physica D **184**, 162-191 (2003).
- [180] B.I. Shraiman, A. Pumir, W. van Saarloos, P.C. Hohenberg, H. Chate, and M. Holen, Physica D **57**, 241 (1992).
- [181] Tania Sauma, Tesis de Magister, *INTERACCION Y CARACTERIZACION DE ESTRUCTURAS LOCALIZADAS EN SISTEMAS NO LINEALES*, <http://www.dfi.uchile.cl/marcel/DatosPersonales.html>

- [182] H. Sakaguchi, and H.R. Brand, *Stable localized solutions of arbitrary length for the quintic Swift-Hohenberg equation*, Physica D, **97**, 274 (1996).
- [183] F. W. Sears and M. W. Zemansky, *University Physics* (Addison-Wesley, 1964).
- [184] Leonid Ivanovich Sedov. *Similarity and dimensional methods in mechanics* (CRC press, 1993).
- [185] A. Seeger, H. Donth, and A. Kochendörfer, Zeitschrift für Physik, **134**, 173 (1953).
- [186] A.J. Scroggie, W.J. Firth, G.S. McDonald, M. Tlidi, R. Lefever, L.A. Lugiato, *Pattern formation in a passive Kerr cavity*, Chaos Solitons Fract. **4**, 1323 (1994).
- [187] J. Scott Russell. Report on waves, *Fourteenth meeting of the British Association for the Advancement of Science*, (1844).
- [188] H.J.T. Smith and J.A. Blackburn, *Experimental study of an inverted pendulum*, Am. J. Phys., **60** 909 (1992).
- [189] L. P. Shilnikov, *A case of the existence of a count- able number of periodic motion*, Sov. Math. Dokl. **6**, 163 (1965).
- [190] V. V. Steblina, Y. S. Kivshar and A. V. Buryak, Opt. Lett., **23**, 156 (1998).
- [191] A. Stephenson, *On induced stability*, Philos. Mag., **15** 233 (1908); Mem. Proc. Manch. Lit. Phil. Soc., **52**, 1 1908).
- [192] Ju Swift and Pierre C Hohenberg. *Hydrodynamic fluctuations at the convective instability* Phys. Rev. A, **15**, 319 (1977).
- [193] A. S. Stodolna, A. Rouzee, F. Lepine, S. Cohen, F. Robicieux, A. Gijsbertsen, J. H. Jungmann, C. Bordas, and M. J. J. Vrakking, Phys. Rev. Lett. **110**, 213001 (2013).
- [194] S. H. Strogatz, *Nonlinear Dynamics and Chaos: With Applications to Physics, Biology, Chemistry and Engineering* (Addison Wesley, Reading, Mass, USA, 1994).

- [195] C. Sulem, and P. L. Sulem, *The nonlinear Schrödinger equation: self-focusing and wave collapse* (Springer Science & Business Media, 2007).
- [196] Dirk Ter Haar. *Collected papers of L.D. Landau* (Elsevier, 2013).
- [197] Mustapha Tlidi, Paul Mandel, and René Lefever. *Localized structures and localized patterns in optical bistability* Phys. Rev. Lett. **73**, 640, (1994).
- [198] P. B. Umbanhowar, F. Melo, and H. L. Swinney, Nature, **382**, 793 (1996).
- [199] H. C. Yuen, and B.M. Lake, Phys. Fluids, **18**, 956 (1975).
- [200] Tanmay Vachaspati. *Kinks and domain walls: An introduction to classical and quantum solitons* (Cambridge University Press, 2006).
- [201] AG Vladimirov, René Lefever, and Mustapha Tlidi. *Relative stability of multipeak localized patterns of cavity solitons*, Phys. Rev. A, **84**, 043848 (2011).
- [202] Ger Vertogen and Wim H Jeu. *Thermotropic liquid crystals, fundamentals*. (Springer, Berlin Heidelberg, 1988).
- [203] X. Wang, and R. Wei, *Dynamics of multisoliton interactions in parametrically resonant systems*, Phys. Rev. Lett. **78**, 2744 (1997).
- [204] X. Wang, and R. Wei. *Interactions and motions of double-solitons with opposite polarity in a parametrically driven system*, Phys. Lett. A **227**, 55-60 (1997).
- [205] X. Wang and R. Wei, Phys. Rev. E **57**, 2405 (1998).
- [206] A. M. Weiner, *Dark optical solitons*, in *Optical Solitons: Theory and Experiments*, ed. by Taylor, J. R. (Cambridge University Press, 1992).
- [207] J. Wu, R. Keolian, and I. Rudnick, Phys. Rev. Lett. **52**, 1421 (1984).
- [208] P. D., Woods, and A. R. Champneys, *Heteroclinic tangles and homoclinic snaking in the unfolding of a degenerate reversible Hamiltonian?Hopf bifurcation*, Physica D, **129**, 147 (1999)

- [209] Y. Xu, T.J. Alexander, H. Sidhu, P.G. Kevrekidis, *Instability dynamics and breather formation in a horizontally shaken pendulum chain*, Phys. Rev. E **90**, 042921 (2014)
- [210] N. J. Zabusky and M. D Kruskal, "Interactions of solitons in a collisionless plasma and the recurrence of initial states". Phys. Rev. Lett. **15** 240Ð243 (1965).
- [211] V. E. Zakharov, J. Appl. Mech . Tech. Phys . **9**, 86 (1968).
- [212] V. E. Zakharov and A. B. Shabat, Sov . Phys. JETP **34**, 62 (1972).
- [213] Zakharov, V. E. (Ed.). *What is integrability?* (Springer-Verlag, Berlin 1991).
- [214] W. Zhang, and J. Viñal, *Secondary instabilities and spatiotemporal chaos in parametric surface waves*, Phys. Rev. Lett. **74**, 690 (1995).